

DEVELOPMENT OF INSTRUMENTATION AND TECHNIQUES FOR
PRECLINICAL IMAGE GUIDED MICROIRRADIATION

A Thesis presented to the Faculty of the Nuclear Science and
Engineering Institute in the Graduate School University of Missouri

In Partial Fulfillment of the Requirements
for the Degree of Doctor of Philosophy

by

SAMANTHA G. PRICE

Dr. Sudarshan Loyalka, Academic Advisor

Dr. Enrique Izaguirre, Research Advisor

DECEMBER 2012

© Copyright by Samantha G. Price 2012

All Rights Reserved

The undersigned, appointed by the Dean of the Graduate School, have examined the thesis entitled

DEVELOPMENT OF INSTRUMENTATION AND TECHNIQUES
FOR PRECLINICAL IMAGE GUIDED MICROIRRADIATION

Presented by Samantha G. Price

A candidate for the degree of Doctor of Philosophy

Professor Sudarshan Loyalka

Professor Enrique Izaguirre

Professor Tushar Ghosh

Professor Mark Prelas

Professor Lixin Ma

Professor Robert Tompson

ACKNOWLEDGEMENTS

I would foremost like to thank my advisors, Dr. Enrique Izaguirre and Dr. Sudarshan Loyalka, for their incredible support of my research. Dr. Izaguirre gave me an opportunity to learn things I never thought I'd know, such as how to use a lathe or perform brain surgery on a mouse. Thank you for letting me a part of your incredible research.

I would also like to thank my committee, Dr. Enrique Izaguirre, Dr. Sudarshan Loyalka, Dr. Tushar Ghosh, Dr. Mark Prelas, and Dr. Lixin Ma, for their dedication to my academic success through their time and insightful consideration of my work.

I would like to thank my collaborators, Dr. Dharanipathy Rangaraj and Dr. Sridhar Yaddanapudi, for their work on the translational research. Dr. Joshua Rubin has been instrumental in our work with *in vivo* testing of the microIGRT and μ EPID.

Finally, I would like to thank my friends and family who consistently kept me focused and calm, even in the most stressful of times. All of these years in graduate school would not be possible without the support of my family. Thank you very much and I love you all.

TABLE OF CONTENTS

ACKNOWLEDGEMENTS	II
LIST OF FIGURES.....	VI
LIST OF TABLES	X
ABSTRACT	XI
INTRODUCTION.....	1
1. BACKGROUND	1
2. PHYSICAL CONCEPTS.....	5
3. IMAGE GUIDED MICROIRRADIATION: THE MICROIGRT INSTRUMENT.....	7
4. TRANSLATIONAL TECHNIQUES	9
5. ORTHOVOLTAGE DOSE MEASUREMENTS	10
6. LITERATURE REVIEW	12
7. REFERENCES.....	13
RESEARCH.....	15
1. IMPLEMENTATION OF A MICRO RESOLUTION DUAL GANTRY PRECLINICAL IMAGE GUIDED MICROIRRADIATOR: THE MICROIGRT.....	15
<i>A. Introduction.....</i>	<i>15</i>
<i>B. The microIGRT mechanical implementation.....</i>	<i>18</i>
i. MicroCT implementation	19
ii. MicroRT subsystem implementation.....	21
iii. Instrument controlling and data processing hardware.....	22
iv. The animal bed and physiological interface.....	23
v. Instrument software	24
<i>C. Methods.....</i>	<i>25</i>
i. Testing the microCT subsystem imaging capabilities.....	25
ii. Test of the microirradiator beam quality and fluence distribution	26
iii. Tests of the beam positioning accuracy for multibeam and fractionated treatments.....	27
iv. Treatment planning and treatment delivery evaluation.....	28
<i>D. Results.....</i>	<i>29</i>
i. MicroCT imaging tests	29
ii. Microirradiator beam characterization.....	31
iii. Irradiation positioning delivery accuracy	34

iv.	Multiple beam isocenter technique irradiation precision	35
v.	Validation of the treatment planning and treatment delivery	36
<i>E.</i>	<i>Discussion and conclusions</i>	38
<i>F.</i>	<i>Acknowledgements</i>	39
<i>G.</i>	<i>References</i>	39
2.	A MICRO ELECTRONIC PORTAL IMAGING DEVICE FOR IMAGE GUIDED CONFORMAL MICROIRRADIATION OF MURINE CANCER MODELS	41
<i>A.</i>	<i>Introduction</i>	41
<i>B.</i>	<i>Methods</i>	45
i.	General construction details.....	45
ii.	Imaging requirements and implementation.....	46
iii.	Instrument interface	48
iv.	Image adjustments and calibration.....	49
v.	Testing of imaging quality and resolution with phantoms	49
vi.	Dosimetric calibration	50
<i>C.</i>	<i>Results</i>	51
i.	μ EPID imaging characterization.....	51
ii.	Coregistration resolution	56
iii.	Determination of dosimetric calibration and sensitivity	56
<i>D.</i>	<i>In vivo portal imaging evaluation</i>	57
i.	Evaluation with model of normal lung tissue response to irradiation	57
ii.	Evaluation with a model of glioblastoma brain tumor treatment	58
iii.	Evaluation with xenograft tumor models.....	59
<i>E.</i>	<i>Discussion and conclusions</i>	59
<i>F.</i>	<i>References</i>	62
3.	BUILDING A BRIDGE BETWEEN PRECLINICAL AND CLINICAL RADIOTHERAPY	65
<i>A.</i>	<i>Introduction</i>	65
<i>B.</i>	<i>Preclinical and clinical radiation oncology</i>	66
<i>C.</i>	<i>Comparative analysis of preclinical and clinical treatment technology and protocols</i>	67
<i>D.</i>	<i>Matching preclinical and clinical external beam delivery dose distributions</i>	71
<i>E.</i>	<i>Metrics to formulate a translational path</i>	74

i.	Maximum, minimum, and mean dose in the target.....	76
ii.	Target dose homogeneity index and penumbra.....	77
iii.	Conformity index.....	78
iv.	Ratio of mean dose in the organ at risk to mean dose in target.....	79
v.	Dose non-uniformity ratio	80
vi.	Dose volume histograms.....	80
F.	<i>Experimental methods</i>	80
G.	<i>Cases of study</i>	82
i.	Partial and whole lung irradiation.....	82
ii.	Glioma irradiation as a case of brain cancer malignancy.....	87
iii.	Liver tumor treatment.....	91
iv.	Partial spinal irradiation.....	93
H.	<i>Conclusions and future work</i>	96
I.	<i>Acknowledgements</i>	98
J.	<i>References</i>	98
4.	INSTRUMENTATION AND TECHNIQUES FOR ORTHOVOLTAGE MICRODOSIMETRY USING SCINTILLATING FIBERS	102
A.	<i>Introduction</i>	102
B.	<i>Methods</i>	106
i.	Detector components	106
ii.	Experimental set up	110
iii.	Beam profile testing.....	111
C.	<i>Results</i>	114
D.	<i>Conclusions</i>	118
E.	<i>References</i>	119
	CONCLUSIONS.....	121
	VITA	125

LIST OF FIGURES

Figure		Page
1.	Image of the microIGRT during instrument construction. The image was taken during the instrument assembly before the microRT subsystem was shielded. The inset shows the animal bed translational x-y subsystem.	19
2.	Images of the microCT subsystem. At the left, a front view of the microCT subsystem from the side of the microRT subsystem during microRT final construction. The micro focus x-ray source, slides, flat panel detector are indicated. At the right, a side view of the microCT, showing the instrument mouse bed x-y fine motion control slides, coarse long slide to transfer the animal from the microCT to the microRT, and instrument main axis (red dot-dashed line).	20
3.	The microirradiator chamber and delivery system. At the left, a view of the jaws and BDMA to collimate and intensity modulate (step and shoot) the microRT treatment beam. At the right, a view of the microRT treatment chamber showing the location of the jaws, BDMA, mouse bed, and μ EPID at the moment of an animal irradiation. Yellow arrow indicates the beam path.	22
4.	Block diagram of the instrument interconnection for instrument control and data handling. The diagram shows the hardware components. The lead lined room and microRT subsystem shielding are indicated to show instrument shielding barriers. Not shown in detail, the microRT beam delivery system and μ EPID for drawing clarity (see figure 3 for these components).	23
5.	Diagram of the instrument software developed to handle the instrument functions. The interface consists of an object oriented software module for each subsystem, the microCT (left), the microRT (center), the μ EPID (right), and the animal bed (not shown). These modules are combined in a single main program where the visual interface is organized in dedicated data visualization and instrument control windows for each subsystem.	25
6.	In-house developed microCT phantoms to test the microCT resolution and contrast in the microCT imaging volume (50 mm diameter and 100 mm length). Left: Five tungsten wire phantom. Center: Acrylic resolution phantom. Right: Five material contrast and HU calibration phantom.	30
7.	Examples of microCT image capabilities to determine animal anatomy. On the top row, we show a microCT scan of a rodent thorax anatomy. At the bottom left, a sagittal image of the head anatomy, and at the bottom right, a translucent rendering of the animal body.	31
8.	HVL for 300 kVp, filtered and unfiltered. 50% intensity dashed line. Filter composition: 0.8 mm Sn, 0.5 mm Cu, and 1.5 mm Al.	32
9.	The x and y direction beam profiles for 0.5x0.5 cm ² and 1.5x1.5 cm ² square beams.	32
10.	Output factor for 225kVp (left) and 300 kVp (right) beams. Beams are filtered with the standard treatment filter, 0.8 mm Sn, 0.5 mm Cu, and 1.5 mm Al.	33

11. Phantom to determine PDD and results for filtered and unfiltered 120 kVp, 225 kVp and 300 kVp beams. a) PDD phantom with 10 points of measurement with radiochromic film. b) 120 kVp, 1 mA. c) 225 kVp, 7 mA. d) 300 kVp, 5.7 mA.....	34
12. Irradiation conducted over 20 fractions. Each point represents the distance from the bony landmark of reference and expected planned value. 500 μ m tolerance (dotted line) is scaled from clinical human irradiations (30 cm diameter) to mouse irradiations (2.5 cm diameter). Each point represents distance from bony landmark to edge of beam in x and y directions. Left: Brain irradiation, scale has been magnified for clarity. Right: Lung irradiation.	35
13. Test of the multiple beam irradiation of phantoms to determine the precision in localizing the treatment using isocentric irradiation. a) Four field box with isocontour inset. b) Three beams with line profile inset. c) Five beams with line profile inset.	36
14. Formulation of a treatment using masks generated from rodent lung microCT images. Top row: Contoured masks using microCT projection data .Masks are formulated to avoid irradiation of the heart and esophagus. Bottom row: Treatment planning computed dose profiles of the beam in beams eye view projections. The figure shows the AP/PA beam in the right column and a right posterior oblique 45 degree beam in the left column.....	36
15. Top row: Verification of the microirradiation of a glioma tumor implanted in the right brain hemisphere. The irradiation was performed using a generic circular mask installed in the mask exchange system, and final positioning was performed using the μ EPID. Positioning resolution is 300 μ m and dose at tumor is 2 Gy per fraction. At the far top right, an optical image of the tumor to assess treatment response. Bottom row: Verification of delivered dose distributions using calibrated radiochromic films in a right lung irradiation example. At the bottom right, the AP/PA field mask and a beam portal image coregistered with the animal anatomy.....	37
16. Left: Image of the developed portal μ EPID installed on a small animal microirradiator beam stopper. Right: 3D rendering of the developed portal μ EPID showing the main mechanical and imaging components. The arrow indicates the path of the light emitted by the scintillator.	45
17. (a) Multi-wire phantom constructed with tungsten wires of different thicknesses to determine imaging resolution in a small animal equivalent volume. (b) MTF graph obtained from the LSF data shown in the inset. LSF was fitted using a Lorentzian function.	52
18. Tissue contrast in relative pixel intensity values with respect to air as a function of the phantom thickness and the imaging beam operating potential and current. Operating potential is reported in the figure for the practical values of x-ray energies.....	53
19. Contrast gradient as a function of phantom depth for the useful range of microirradiation source practical imaging potential and currents, which include 60 kVp, 80 kVp, and 120 kVp with current values of 0.5 mA, 0.75 mA, and 1 mA.	54
20. Constant contrast curves for contrast values of 500 and 400 as a function of small animal absorbed dose for microirradiation source practical imaging potential and currents.	55
21. Left: DQE for filtered treatment orthovoltage beams of 225 kVp and 300 kVp, with 2.9 mm of Cu and 3.9 mm of Cu, respectively. Right: DQE for anatomical imaging beam of 120 kVp, filtered with 2.8 mm of Al and operating currents of 0.5, 1, 1.5, and 2 mA.	55
22. Intensity vs. dose rate for two treatment energies. 250 kVp (solid line) for 1–7 mA and 300 kVp (dashed line) for 1-5.7 mA.	57

23. Anatomical portal images coregistered with orthovoltage treatment beams. (a) Portal image of a mouse thoracic cavity overlay with a split beam to irradiate both lungs. (b) Portal image of a mouse head showing the bony anatomy with the circular treatment beam placed at the right hemisphere. (c) Portal image of a mouse torso with a xenograft tumor in the mammary fat pad and an overlay of the treatment field.....	58
24. Determination of the dose profile delivered to the glioma implanted in the brain hemisphere as shown in figure 23b. The dose contours, labeled in cGy, are based on the dosimetric calibration of the μ EPID dose curve reported in figure 22 for the 300 kVp orthovoltage treatment beam.....	60
25. Dose rate versus normalized depth for parallel opposed beams. A clinical 6 MV beam, dotted line, delivered for a 31 cm depth, plotted on the lower x-axis. A preclinical 300 kV beam (189 keV average energy), solid line, delivered for a 25 mm depth and plotted on the upper x-axis.....	72
26. Demonstration of the stochastic noise inherent in high resolution film analysis. Each pixel is approximately 1 μ m. The graph has been zoomed in to show a 100 μ m distance of the central portion of the beam. Each line represents a line profile of the same film, spaced 2 pixels apart. Inset: Three complete line profiles.	78
27. Three beam lung tumor irradiation. Top: DVH illustrating the doses to the target, heart, and healthy lung. Bottom: Isodose contours overlayed with microCT imaging.....	85
28. Three beam irradiation of the entire right lung of a mouse. Left: DVH with the targeted right lung, contralateral lung, and heart contoured. Center: Intensity map overlay of the 45 degree angle beam. Right: Intensity map overlay of the AP/PA whole lung irradiation.....	87
29. Three beam brain tumor irradiation of a mouse. Top: DVH with target, healthy brain tissue, and visual system contoured and a prescribed dose of 60 Gy. Bottom: Coronal overlay. Bottom right: Transverse overlay.....	90
30. A three beam liver irradiation with a circular aperture. Top: DVH for the target in the liver, the healthy liver tissue, and the lungs. Bottom: Isodose contours overlayed with microCT images.....	93
31. Partial spine irradiation of a mouse using three and five beams. Top: DVH for both three beams (solid lines) and five beams (dashed lines). Center: Isodose overlay of a three beam treatment using a square aperture with microCT sagittal and transverse images. Bottom: Isodose overlay of a five beam treatment using a square aperture with microCT sagittal and transverse images.....	94
32. Left: Dosimeter electronics. Optical fiber has been epoxied to the MPPC diode and coated with black paint. Right: Two scintillating fibers, BCF-12 and BCF-60, coupled to clear fibers with optical clear epoxy, painted black.....	107
33. Efficiency curves for BCF-12 (dotted red line), BCF-60 (dashed green line), and the MPPC (solid blue line).....	108
34. Schematic view of the experimental set up. The bold black line indicates the exterior wall of the lead lined room. An angled hole, a maze, through the wall allows for the passage of cables without the risk of radiation exposure.....	111
35. Left: Portal images of dosimeter overlayed with field size images. The fibers and ion chambers are attached to an acrylic half cylinder phantom and placed in the mouse bed,	

extending past the end to avoid backscatter error. The beam is centered on the dosimeters. A shadow feature has been added to enhance viewing on the BCF-12 500 μm fiber..... 113

36. Diode response curves for the 500 μm BCF-12 fiber and the 1500 μm BCF-60 fiber. 114

37. Dose as a function of depth as measured by GafChromic film (solid blue line), the BCF-60 fiber (dashed green line), BCF-12 fiber (dotted red line), a CC04 ion chamber (pink squares), and a CC01 ion chamber (black stars). Both the film and the fiber responses were relative and normalized to the ion chamber responses..... 115

38. Beam profiles measured with GafChromic film (solid blue), CC04 ion chamber (dot-dash purple), CC01 ion chamber (short dashed orange), BCF-12 (dotted red) and BCF-60 (long dashed green). a) 1x1 mm^2 beam. b) 2x2 mm^2 beam. c) 5x5 mm^2 beam. d) 10x10 mm^2 beam.... 117

39. Left: Dose rate response of the BCF-12 (red dotted line) and BCF-60 (solid blue line) scintillating fibers for a 120 kVp beam and currents between 0.5 and 5 mA. Right: Dose rate response of the BCF-12 (red dotted line) and BCF-60 (solid blue line) scintillating fibers for a 300 kVp beam and currents between 1 and 5.7 mA. 118

LIST OF TABLES

Tables	Page
1. HVL for most commonly used source potentials. 120 kVp filter – 0.75 mm of Al. 225 kVp and 300 kVp filter - 0.8 mm Sn, 0.5 mm Cu, 1.5 mm Al.....	31
2. Beam homogeneity, symmetry, and penumbra for four field sizes.....	32
3. Organ volume comparison between mice and humans	75
4. Metric comparison for single open field beam.....	77
5. Metric comparison between clinical and preclinical for a 3 beam lung treatment.	78
6. Comparison of preclinical and clinical metrics for a lung tumor treatment.....	85
7. Comparison of preclinical and clinical metrics for a brain tumor treatment.....	90
8. Comparison of preclinical and clinical metrics for a liver tumor treatment.....	92
9. Comparison of preclinical and clinical metrics for a spinal tumor treatment.....	95
10. Comparison of commonly used dosimeters for small fields	106
11. Comparison of fiber parameters.....	108
12. Comparison of FWHM and penumbra for a 1x1 mm ² beam detected with GafChromic film and the microdosimeter with a BCF-12 and BCF-60 fiber.	116
13. Comparison of FWHM and penumbra for a 2x2 mm ² beam detected with GafChromic film, a CC01 ion chamber, and the microdosimeter with a BCF-12 and BCF-60 fiber.	116
14. Comparison of FWHM and penumbra for a 5x5 mm ² beam detected with GafChromic film, a CC01 ion chamber, a CC04 ion chamber, and the microdosimeter with a BCF-60 fiber.	116
15. Comparison of FWHM and penumbra for a 10x10 mm ² beam detected with GafChromic film and a CC04 ion chamber.	116
16. Comparison of the FWHM deviation from GafChromic film measurements for four field sizes and four dosimeters. Values are shown in percent.	117
17. Comparison of the penumbra deviation from GafChromic film measurements for four field sizes and four dosimeters. Values are shown in percents.....	117

Abstract

Radiation therapy accounts for more than half of cancer treatments in the US, and in order to provide the most effective treatment to patients, new developments are implemented each year. Before a novel radiation therapy device or technique can be used to treat patients in the clinic, it must first undergo testing. One of the most effective testing methods is preclinical small animal testing, because the testing environment provides a large sample population on which treatment variations can be tested for efficacy and possible side effects. To improve the effectiveness of preclinical testing, the devices and methods used on small animals should closely resemble those used in the clinic. These include irradiators, fractionation schedules, repeatability methods, and results characterization. Results characterization will provide a translational pathway between the preclinical and clinical environments of a small animal irradiation and human treatments to account for variation in treatment beams and subject size between preclinical and clinical irradiations.

The Biomedical Physics Laboratory at Washington University in St. Louis, with whom I was working, developed a preclinical small animal image guided microirradiator, the microIGRT, and we characterized the device using clinical methods, such as those used for machine acceptance and quality assurance. In order to provide treatment verification and subject positioning repeatability, we designed, developed, and characterized a micro electronic portal imaging device (μ EPID), similar to the portal devices used on clinical linear accelerators. Using the microIGRT and the μ EPID, we developed treatments for small animal brain, lung, liver, and spinal tumors using clinical treatment planning methodologies translated to preclinical small animal models. We characterized the treatment results with several metrics and compared these to clinical treatments. The metrics were compared, side by side, and conclusions were drawn for the efficacy of the small animal treatment to establish the first steps for a pathway to translate preclinical results to clinical trials. Considering the difficulties of dosimetry for small fields commonly used in small animal irradiations, we also designed and developed a fiber scintillating microdosimeter. This dosimeter allowed for more accurate orthovoltage beam characterization, thus improving treatment planning and translational treatments.

Introduction

1. BACKGROUND

There are currently over 11 million people suffering from cancer (Howlader, et al., 2012). While there are many treatment options, radiation therapy accounts for over 50% of the cancer cases. In order to better treat patients, new instrumentation and techniques for radiation therapy are continuously designed and developed. After their conception, these novel devices must be tested before they can be used to treat patients in the clinic. The first tests can be conducted using computer models. While these can be fairly accurate in terms of modeling patient anatomy and physiological effects, a computer model is based on the average human, rather than considering the vast number of differences in individuals. Therefore, a computer model will not be able to accurately predict how a novel technique or instrument will affect a varied sample group. For some treatment options, such as for radioenhancers and radioprotectors, *in vitro* testing is available.

Radioenhancers, or radiosensitizers, are drugs which can be administered to the patient to target tumor cells and provide enhanced tumor response to radiation treatment. A radioprotector is a drug administered to target healthy tissue and provide reduced response to radiation (Coleman and Mitchell, 1999). For the most effective use of these drugs, it is important to test the targeting ability and sensitivity of the drug to specific tissues, which can be conducted on cells in culture. These cells can be administered the drugs for targeting efficacy testing and irradiated in culture for evidence of enhanced or reduced radiosensitivity. Cell cultures, however, typically feature only one tissue, so it will not be evident if the drugs will target other tissues in the body or produce side effects in combination with radiation treatment, so *in vivo* testing will follow.

One *in vivo* option is proceeding directly to clinical trials and human testing. This method utilizes patients who are considered terminal or non-responsive to current treatment methods, and these patients can volunteer to participate in the study for alternative treatments. Some advantages of this option include the ability to begin immediately treating patients and possibly improving their quality of life. However, there are some disadvantages. While the earlier computer model testing could tailor a radiation therapy to safely

treat the average person, there could be treatment effects that are seen in only a portion of the population, and these effects could lead to patient harm. Once an adverse effect is discovered, the technique must be sent back to the design and development stage. Another disadvantage is the amount of time required to obtain a statistically significant amount of data from a clinical trial. Because there may possibly be a limited number of patients, it could take years to acquire a large data set. To possibly avoid an extended use of time and money, and prevent patient harm, an *in vivo* option for novel radiation therapy techniques and instrumentation is testing in the preclinical environment.

Preclinical testing involves the use of small animals to provide a large sample group that will illustrate long term effects in a shorter time than that of a human. With a very large sample group, many treatment options can be tested more quickly and efficiently, thus eliminating ineffective treatments. Mouse models also offer consistent phenotypes, thereby allowing the investigator to test the radiation therapy method or instrument on many available physical characteristics, such as healthy mice, suppressed immune systems, and knock out genes. The radiation therapy device or protocol can also be tested on multiple stages of cancer, rather than the typically advanced stages seen in the clinical trials discussed previously. After a preclinical trial has been conducted and deemed successful, the device or protocol can be considered safe for human testing. In order to fully utilize small animal testing, the preclinical testing environments should offer many, if not all, of the instrumentation and techniques already available in radiation therapy clinics. The more closely a preclinical experiment emulates a clinical treatment, the more accurately the results can be evaluated and applied to the clinic. As the clinic modernizes so must the preclinical environment. Outdated or lagging technology used for small animal imaging and treatment will not accurately simulate a clinical setting and will therefore skew experimental data from preclinical testing.

The two main aspects of radiation oncology are imaging and therapy. Diagnostic imaging includes functional and anatomical imaging. Functional imaging includes PET, SPECT, gamma camera, fluoroscopy, ultrasound, and some MRI methods. Anatomical imaging includes MRI, ultrasound, and CT. Typically, functional imaging will provide an excellent view of the path of a drug or blood flow through a tissue, but it will not always provide accurate localization in the body. Anatomical imaging can provide high resolution “snap shots” of the anatomy but cannot provide information about motion or function. To best utilize these varied techniques, imaging fusion options exist to combine an overlay of a functional

image with an anatomical image (Townsend & Cherry, 2001). Imaging is vital for diagnosis and delineation of a tumor in cancer treatment. The more precisely a tumor can be located and quantified, the more accurately it can be treated.

Following patient imaging, a treatment plan is generated to guide therapy. A treatment modality will be chosen and the target and organs at risk (OAR) will be delineated on the patient image. In forward, or conventional, treatment planning, the beams are shaped by the user, and the treatment planning software will present the results of the treatment based on the specified beams, in terms of dose to the target and OARs. The results of the treatment can be verified using the known data for beam energy and shape and dose distribution in a phantom. This system was used in the past for simpler plans such as basic conformal treatments, i.e. without intensity modulation.

With the onset of IMRT, plans became much more complicated and inverse treatment planning was developed (Barth, et al., 1990). This method specifies constraints that the software uses, along with an optimization method to determine the shape and intensity of a beam/beams to deliver the specified treatment. This method is computationally intensive and can be time consuming, but advancements in technology have drastically decreased computation time. The advantage of advanced treatment planning software which utilizes 3D imaging is the use of volumetric data. A treatment plan can evaluate the dose to each contour with respect to contour volume. In inverse planning, a dosimetrist will choose the treatment beam energy, number of beams, and beam angle to develop the treatment. According to published data, such as QUANTEC [Bentzen, et al., 2010], there are limits for each OAR which define the maximum or mean dose which can safely be delivered to each organ to reduce the risk of side effects. These constraints have been developed from years of clinical research outlining the dose limits to each organ based on the possible dose effects. A dosimetrist will input these limits into the treatment planning software and use inverse planning to evaluate the modulation of the beam at each angle required to deliver the defined treatment. After the software has produced a plan, the dosimetrist can evaluate the plan and then decide to either alter parameters and run the plan again, or accept the plan as a successful treatment. After a successful treatment plan has been developed, it will then be sent to the appropriate treatment modality station.

Radiation therapy includes the use of brachytherapy, linear accelerators (linac) for IMRT, Tomotherapy, conventional 3D radiation therapy with a radioactive source or a linac, and stereotactic radiotherapy. Each treatment option offers a range of treatment options for which it is best suited. For example, a brain tumor is more likely to be treated with stereotactic radiotherapy due to the limited tissue motion in the brain, as opposed to a classic 3D conformal treatment option which uses larger field sizes. Stereotactic radiotherapy is a treatment option which utilizes a coordinate system relative to the patient, rather than relative to the treatment machine. In the case of brain treatment, a frame is attached to the patient's head, which provides the coordinate system relative to the patient and guides the treatment. This can allow for more precise treatment localization and hypofractionated (fewer fractions) treatments. Another example is cervical cancer, which is more likely to be treated with brachytherapy than conventional 3D radiation therapy due to availability of a body cavity for a brachytherapy device. Brachytherapy is an internal treatment and can use either a radioactive source or a small electronic x-ray device, as opposed to IMRT, which is an external beam treatment.

All of these modalities for imaging and therapy offer patients a moderately individualized cancer treatment plan to best suit their needs. With a wide range of options in the clinic, it's necessary to develop preclinical instrumentation and techniques to match. Small animal microirradiator exist in some universities, offering researchers a platform to perform imaging and radiation therapy on small animals in a setting similar to a human treatment. These microirradiator can offer high resolution imaging and fractionated treatments, similar to tools used in the clinic, and perform conformal treatment for improved cancer therapy. An aspect of clinical irradiations that is only beginning to be explored in microirradiator is the use of image guided therapy. Image guided therapy uses portal imagers or other on-board imaging to provide either daily CT images of the patient or real time *in vivo* imaging during treatment to improve therapy. Daily CT images, like those provided by Tomotherapy (The TomoProcess), provide therapists an updated view of patient anatomy each day of treatment, rather than relying on pre-treatment CT images that could possibly be weeks old. This updated image can improve therapy through daily tumor and healthy tissue location verification and tumor size. Daily treatment can be altered to accommodate these changes. Real time *in vivo* imaging, provided by electronic portal imaging devices (EPID), can provide therapists a view of the patient positioning and beam profile during treatment. This can verify proper beam energy and collimator

placement, such as wedges, blocks, or multileaf collimators (MLC). Daily CT imaging and EPIDs can be excellent resources to improve radiation therapy in the clinic. Through the use of pre-treatment imaging and on-board imagers, radiation therapy is progressing towards more adaptive treatments with image guidance capabilities. These options are also being utilized in preclinical irradiations to improve the correlation between preclinical and clinical treatments.

As preclinical instrumentation and techniques improve to simulate clinical treatments, the results of preclinical experiments will begin to have a stronger correlation with clinical results. One reason that many clinical developments proceed directly to clinical trials is because there is not a well understood or agreed upon correlation between preclinical and clinical irradiation results. Based on the properties of a clinical experiment, such as subject size and treatment beam energy, preclinical irradiations will differ from clinical irradiations, regardless of the steps taken to design preclinical devices with clinical similarity. It is therefore important to understand how the two treatment environments are similar and how they differ. Steps which can be taken to build a bridge between the preclinical and clinical testing environments include the similitude of treatment characterization. This can range from how the imaging and treatment machines are commissioned and characterized, to how the treatment results are summarized. Preclinical characterization can take its direction from clinical treatments, based on the extensive treatment experience the clinic has seen. This back translation to preclinical testing will strengthen the bridge between the two testing environments and provide the foundation for preclinical testing to be used for every novel clinical development.

2. PHYSICAL CONCEPTS

One of the primary differences between clinical and preclinical radiation therapy is the beam energy. Human treatments use a megavoltage beam, 1-25 MeV, while small animal treatments use an orthovoltage beam, 40-320 keV. Orthovoltage sources are typically smaller, less expensive, and more versatile than megavoltage beams, making them ideal for small animal irradiation. Orthovoltage beams also have less tissue penetration than megavoltage beams, perfect for the considerably smaller body diameter of a mouse compared to a human. A 6 MV photon beam has a maximum dose deposition at 1.5 cm, whereas a 300 kVp x-ray beam deposits most of its dose in the mm range (Sheikh-Bagheri & Rogers, 2001). Another crucial

difference between orthovoltage and megavoltage is the method of interaction between the photons and matter. At higher energies, the predominant interaction is Compton scattering. In Compton scattering, an inelastic collision takes place between a photon and an orbital electron, considered to be at rest. The electron recoils with a certain amount of energy and the photon is deflected with a reduced energy and altered wavelength. Compton scattering is dependent upon the electron density of matter rather than the atomic number (Z) so, at megavoltage energies, photons interact similarly with bone and tissue. Bone has a higher atomic number, around 14, than tissue, which has an atomic number of around 8. At orthovoltage energies, photon interactions include not only Compton scattering, but also the photoelectric effect, which is predominant at lower energies. In the photoelectric effect, the photon is completely absorbed and an electron is emitted from an atom. The probability of the photoelectric effect is dependent upon Z^3 , so a photon will preferentially interact with a higher Z material, such as bone, rather than tissue (Khan, 2003). This phenomenon is an important aspect of orthovoltage irradiation to consider, because bone could receive a significantly higher dose than tissue, leading to bone marrow depletion. This bone marrow depletion could lead to reduced red blood cell counts which could ultimately starve the animal of blood. Tumor growth relies on extensive vascularity and if the animal is starved for blood, the tumor will begin to shrink. At this point, it would be unclear if the tumor shrinkage was due to reduced vascularity or a successful treatment. A photon beam is not a monoenergetic stream of photons; rather it is a spectrum of energies, with the peak energy reported, such as 6 MV or 300 kVp. Because the beam is a spectrum, it will contain not only the higher energies preferred for treatment, but also the lower energies interacting through the photoelectric effect which provide superfluous dose. Lower Z materials like tin and copper filter out orthovoltage energies below 120 kV but retain the higher treatment energies. A commonly used treatment filter in microirradiator is Thoreau's filter. It is comprised of tin, copper, and aluminum, in that order, placed in the beam path. The reason for this specific order is due to the reduced density from beam to patient. The new x-rays formed in the tin are absorbed by the copper, the new x-rays formed in the copper are absorbed by the aluminum, and the new x-rays formed in the aluminum are absorbed in the air. If orthovoltage irradiators did not filter their beams, the preclinical results could be very different from clinical results, eliminating the usefulness of the preclinical experiment.

3. IMAGE GUIDED MICROIRRADIATION: THE MICROIGRT INSTRUMENT

There are several methods for small animal irradiation. Some researchers have developed irradiators using shielded brachytherapy sources with an aperture for irradiation (Stojadinovic, et al., 2007). This method is simple and straightforward, but it does have some drawbacks. For instance, the source is constantly decaying and it will have to be replaced periodically. The source must also be shielded because it is emitting radiation in all directions, even when an animal is not being treated. Another option, one utilized in our instrument, is an x-ray tube. X-ray tubes offer orthovoltage energy beams that can be turned on and off, so there is no need for constant shielding. The x-rays do not decay, so there is an extended life time of use. There are commercially available microirradiators that feature peak energies from 225-320 kVp. These instruments come with the source intact and shielding in place. The downside to these commercial instruments is the lack of options for varying dose rate, source-to-surface distance, and beam angle. In order to address this lack of variability, my group designed our own microirradiator, termed the microIGRT. Other institutions have developed their own irradiators, equipped with an image guidance system. These systems use the same x-ray source to provide both imaging and treatment (Wong, et al., 2008). While this is convenient because only one source is required, it limits the capabilities of the irradiator. Lower energies, such as those between 60-120 kVp, are ideal for imaging but are not ideal for treatment. With these systems, there must be a compromise between image and treatment quality. The microIGRT we have developed overcomes these obstacles via independent imaging and treatment subsystems, the microCT and the microRT, both of which have independent x-ray sources.

While other microirradiators exist with imaging capabilities, our microIGRT is the only microirradiator with a dual gantry that features on-board CT. The CT subsystem includes a source with a $75 \times 75 \mu\text{m}^2$ focal spot, 80 kVp maximum operating voltage, and 0.5 mA maximum current. The CT source is mounted on a slide to allow for the adjustment of source-to-object distances. On the opposite slide, a flat panel detector is mounted and aligned, with a pixel array of 1024×1024 pixels. Based on the large number of pixels available, imaging options vary from a low resolution 64 image reconstruction which is performed very quickly with a very low dose, to a high resolution 512 image reconstruction which can be used for precise tumor localization and delineation. The on-board CT offers not only high resolution diagnostic CT imaging but also daily CT imaging of each small animal to provide image guided treatments. These daily images

improve therapy through accurate subject positioning before treatment to precisely locate the tumor and surrounding healthy tissues. In the clinic, a patient treated with radiation therapy is conscious during treatment and can be told to remain still or be restrained in an alpha cradle. Alpha cradles ensure repeatable positioning and precision, for daily treatment. This will improve the conformity of treatment because the patient was imaged in a CT in the same position in which they are treated. Theoretically, the tumor and healthy tissues will not have moved too drastically between imaging and treatment. Small animals cannot be told to remain still and restraint is not always practical, so anesthetization is utilized to ensure the animal moves as little as possible. While under anesthesia, there will still be breathing and cardiac motion, but the animal is not actively moving around during treatment. Microirradiators rely on millimeter precision for conformal treatment and it's highly unlikely a researcher will position a mouse in exactly the same position for every treatment, so on-board CT imaging can guide the researcher in their treatment planning by displaying daily anatomical images to locate the area to be irradiated.

Our microIGRT features a dual gantry system, with CT and RT, and a single shared mouse bed that travels between the two. For each fraction, a mouse can be placed in the mouse bed under anesthesia, undergo CT imaging and then pass immediately to the RT gantry where treatment can be performed without perturbing the anatomical positioning. The positioning of the mouse bed can be verified with the use of a portal imager. We also developed a micro electronic portal imaging device to be used for subject and beam positioning verification. The design of the portal imager was based on clinical devices and is used in much the same manner. A scintillating screen, positioned in line with the beam and the mouse bed, produces light when photons interact. The light is viewed by a CCD camera positioned out of the beam line, to prevent radiation damage to the electronics from radiation. The image is then viewed on screen with our in-house developed software and can be used to reposition the mouse bed, if necessary, as well as verify proper beam aperture and filter placement during treatment.

The microIGRT treatment was designed with clinical similarity in mind, to provide highly conformal orthovoltage treatment through the use of beam delimiting apertures, designed with our treatment planning system, and developed with our tungsten epoxy method. There are six beam apertures available for each treatment, providing multibeam therapy to help spare healthy tissue, similar to treatments performed on humans in the clinic. Finally, the beam is modified through specially designed filters to eliminate low

energy photons (e.g. those below 150 keV), thus raising the average energy of the beam and reducing unnecessary dose to the skin and bone marrow.

The entire microIGRT system is unified through a coaxial architecture and software developed in-house, which provides quick and seamless treatment with clinical relevance. The system can accommodate large cohort numbers that can be treated with conformal multibeam treatments in a reasonable time period.

4. TRANSLATIONAL TECHNIQUES

The entire purpose of preclinical small animal irradiation is to design, develop, and test novel radiotherapy techniques and devices which will eventually be put into clinical practice. It is therefore crucial that a preclinical experiment provide data which is clinically relevant. Based on the differing treatment beam physics, as explained above, it's clear an orthovoltage beam will deliver a different treatment than a megavoltage beam, due on the photon interactions. Additionally, because the subject scale is vastly different between humans and small animals, with mice only 10% of that of a human for most organs, it's important to adjust a preclinical treatment accordingly. The difficulty in designing a preclinical treatment is how to adjust for treatment beam energy, subject scale, and treatment modality to deliver a treatment which will provide clinically relevant results. The first step is to characterize a clinical treatment that was deemed successful. This should include determining metric values for the treatment which characterizes the results. These metrics will become the standard for a clinical treatment to which a preclinical treatment can be compared. The metrics chosen should characterize the shape of the beam and the dose distribution in both the target and the surrounding tissues. This will demonstrate the conformity of the beam, the sparing of healthy tissues, and effectiveness of treating the target to the prescribed dose. The clinical environment has advanced treatment planning software at its disposal, which can be used to determine metric values and then be used to formulate treatment and resultant metrics.

Preclinical treatment planning varies between institutions, but forward planning is typically used for small animal treatments. The beams are shaped according to organ contours and multibeam treatments are delivered using 3D imaging, such as microCT. In the same way as the clinic, this volumetric data can be used to determine preclinical metric values. The purpose of using the metrics is to determine what the values should be for a preclinical treatment to obtain similar results to the clinic, not necessarily identical

metric values. For instance, the penumbra in a clinical beam should be considerably larger than that of a preclinical beam, based on the size of the treatment area, but the treatment efficacy should be the same. The challenge in this process is attempting to standardize preclinical treatment, based on different mouse breeds, treatment sites, and orthovoltage treatment delivery modalities. In this project, we used four treatment sites to plan a preclinical small animal irradiation based on clinical protocols but delivered with our microirradiator. The results of the small animal treatments were compared to that of clinical treatments to determine how preclinical trials should be conducted for specific treatment sites such that they provide clinically relevant results.

5. ORTHOVOLTAGE DOSE MEASUREMENTS

Orthovoltage dosimetry is conveniently mapped out in AAPM TG-61 (Ma, et al., 2001). There are many methods to measure dose, depending on the type of radiation and dose data required. One of the most common dose measuring tools utilized in the clinic is an ion chamber. Ion chambers are versatile, available in many volumes and shapes, and can be used for a wide range of energies. Ion chambers are typically calibrated with a Co-60 source, which delivers a uniform treatment beam energy of 1.25 MeV, as opposed to the spectrum of energies seen in an electronic x-ray source. According to TG-51, used for megavoltage dosimetry, an ion chamber can be used to measure absolute dose for various beam energies according to calibration factors as provided by an accredited dosimetry calibration laboratory (Almond, et al., 1999). An advantage of ion chambers is the uniform response to a wide range of treatment energies based on correction factors. If the correction factors are known, ion chambers are useful for preclinical imaging and treatment, typically up to 300 kVp. These correction factors, as explained in TG-61, can be found using the half value layer thickness, which denotes beam quality, and additional ion chamber and electrometer specific factors. The half value layer is found by inserting increasing thicknesses of aluminum or copper into the beam path and measuring the relative beam intensity. The half value layer is the thickness of material in the beam path required to reduce the beam intensity by half. This value can then be used to find the average energy of the beam and determine the beam quality to be used for dose measurements. An additional correction factor accounts for the temperature and pressure of the testing environment when compared to the standard temperature and pressure used during calibration at an accredited laboratory. The

remaining correction factors account for the ionization chamber polarity effect, the stem effect, and the electrometer effect, as provided by the accreditation laboratory. The dosimetry method typically used for orthovoltage treatments is called “in-air”, which means the absorbed dose to water at the surface of a water phantom is measured. According to TG-61, there are two energy levels in an orthovoltage irradiation; low energy, less than 100 kV, and medium energy, from 100-300 kV. The upper energy range may use the “in-phantom” method, which determines dose to water at a 2 cm depth in water. The wide variety of shapes and sizes for ion chambers provide a varied level of spatial resolution, with active lengths as small as 3 mm. This can be very useful in a clinical IMRT irradiation, with field sizes in the centimeter range. However, for a small animal irradiation, field sizes can be as small as 0.5 mm in diameter, so ion chambers are not necessarily ideal in all aspects of orthovoltage dose measurement.

Another dose measurement method is radiochromic and radiographic film. Film provides very high spatial resolution, limited only by the size of the grains in radiographic film, the composition of the proprietary active layer of radiochromic film, and the resolution of the scanner used to digitize the film. Radiographic film is composed of silver halide and can become overexposed at orthovoltage energies due to the high Z number of silver in response to the photoelectric effect. Therefore, radiochromic film, with the highest Z number of 6, is a better option at lower energies, with similar response at energies ranging from 6 MV to 120 kVp. According to GafChromic, there is a 25% lower response to kV beams than to MV irradiation. (GafChromic, 2010) Because of this nearly independent response to energy in the orthovoltage range, film is an excellent option for relative dosimetry in orthovoltage treatments. Radiochromic film is not sensitive to ambient light and does not require development, so it is therefore much more convenient than radiographic film for measurements. However, darkening of the film can vary slightly between film batches and it is recommended that 24 hours should pass between exposure and digitizing, for maximum darkening, so absolute dosimetry is not always possible. Calibration on a batch of film can be performed with a source of known energy, and absolute dosimetry can then be performed with the same batch of film.

Some preclinical research is looking at novel methods for orthovoltage dose measurements. This includes absolute dose measurements for treatment delivery as well as relative measurements for values like beam distribution. Arrays have been used to perform 2D dose measurements using devices such as diodes or ion chambers. Depending upon the size of the array, the spatial resolution can be adequate for small animal

treatment fields. Another option is the use of scintillating fibers. These fibers can be water equivalent at orthovoltage energies, so as not to perturb the beam, and can give high spatial resolution based upon the size of the fiber. The scintillating element can be integrated into an array or scanned for a 2D measurement of dose distribution, as well as calibrated to be used as an absolute dosimeter. Beddar et al (1992) have demonstrated the use of plastic scintillating fibers in megavoltage dosimetry, and these methods can be translated to orthovoltage applications. The use of scintillating fibers for photon dosimetry can be translated to orthovoltage applications. In this project, a small scintillating element was used to evaluate the dose distribution and beam profiles of small fields in an orthovoltage irradiator.

The overall advantage of improved orthovoltage dose measurements will be more accurate small animal treatment planning and delivery. The more knowledge about the shape and dose delivery of a beam is acquired, the more precise and accurate a treatment can be. This will lead to more clinically applicable treatments and results.

6. LITERATURE REVIEW

Several groups are performing preclinical small animal irradiations with a variety of microirradiator. In the past, most small animal irradiations were performed by either irradiating the entire animal or using basic surface collimators. This method is vastly different from the protocols used in the clinic and was therefore producing results that were not clinically relevant. In an effort to improve these results, groups began to develop and utilize microirradiator capable of producing more conformal treatment beams.

At John Hopkins, Wong et al have developed the Small Animal Radiation Research Platform (SARRP). Similar to the Princess Margaret system, they use a single source with two focal spots to image and irradiate. They use a smaller focal spot for imaging than Princess Margaret, which can improve their imaging resolution. Treatment collimation is provided through a primary square collimator, followed by secondary cylinders which can be exchanged depending upon the treatment site. Contrary to the Princess Margaret set up and our set up, which rotates the source and detector, John Hopkins has a stationary source and detector and rotates the animal subject. They have been actively using SARRP for several years for small animal imaging and irradiation studies (Wong, et al., 2008).

Some groups have chosen to utilize a commercially available microirradiator, such as the X-Rad 320 Series, produced by Precision X-Ray [PXinc.com, 2012]. This system is available in a number of peak energies, such as 160, 225, 350, and 400. The 320 series features an 8 mm² focal spot and varying dose rates, which include 1, 3, and over 15 Gy/min depending upon the filter. The filters available are either 1 or 4 mm of copper. Commercially available systems offer the advantage of a readymade microirradiator to begin conducting experiments. The disadvantage is the lack of customization that can be done to develop a more unique experiment; however some groups have begun work to add on to the original system to provide more options, such as an advanced collimating system and image guidance capabilities [Pidikiti, et al., 2011]. Advanced versions of these systems also include turntables for multibeam irradiations. At Princess Margaret, they utilize the X-Rad 225Cx, which incorporates image guided irradiations to improve treatments. A single source, used for both imaging and treatment, is mounted on a C-arm gantry to allow for 360° of imaging and treatment. The source offers two focal spots, with a small 1 mm focal spot for imaging and a larger 5.5 mm focal spot for treatment. The source operates from 5 kVp to 225 kVp, imaging around 100 kVp and treating at 225 kVp. The group developed filters and circular and rectangular collimators to improve treatment. Image guidance is provided through CBCT imaging and fluoroscopic imaging. The Princess Margaret group has been actively using their microirradiator since 2008 for both imaging and treatment applications (Clarkson, et al., 2011).

7. REFERENCES

- Almond, P. R., Biggs, P. J., Coursey, B. M., Hanson, W. F., Huq, M. S., Nath, R., & Rogers, D. W. (1999). AAPM's TG-51 protocol for clinical reference dosimetry of high-energy photon and electron beams. *Med Phys*, 26(9), 1847-1870.
- Barth, N. H. (1990). An Inverse Problem in Radiation Therapy. *Int. J. Radiation Oncology Biol. Phys.*, 425-431.
- Beddar, A. S., T. R. Mackie, and F. H. Attix. (1992) "Water equivalent plastic scintillation detectors for high-energy beam dosimetry: I. Physical characteristics and theoretical considerations". *Phys Med Bio*, 37, 1883-1900.
- Bentzen, S. M., L. S. Constine, J. O. Deasy, A. Eisbruch, A. Jackson, L. B. Marks, R. K. T. Haken, & E. D. Yorke. (2010) Quantitative analyses of normal tissue effects in the clinic (Quantec): An introduction to the scientific issues. *Int J Radiat Oncol Biol Phys*, 76, S3-S9.
- Clarkson, R., Lindsay, P., Ansell, S., Wilson, G., Jelveh, S., Hill, R. P., & Jaffray, D. A. (2011).

Characterization of Image Quality and Image Guidance Performance of a Preclinical Microirradiator. *Med Phys*, 38(2), 845-856.

- Coleman, N. C & Mitchell, J. B. (1999). Clinical Radiosensitization: Why it Does and Does Not Work. *Journal of Clinical Oncology*, 1-3.
- Howlader, N., Noone, A., Krapcho, M., Neyman, N., Aminou, R., Altekruse, S., . . . (eds), C. K. (2012). SEER Cancer Statistics Review, 1975-2009 (Vintage 2009 Populations). Bethesda, MD: National Cancer Institute.
- International Specialty Products. (2010). GafChromic EBT2: Self Developing Film for Radiotherapy Dosimetry. Wayne, NJ.
- Johns, H. E., & Cunningham, J. R. (1983). *The Physics of Radiology*. Springfield, IL: Charles C Thomas.
- Khan, F. M. (2003). *The Physics of Radiation Therapy*. Philadelphia, PA: Lippincott Williams & Wilkins.
- Ma, C., M., Coffey, C. W., Dewerd, L. A., Liu, C., Nath, R., Seltzer, S. M. & Seuntjens, J. P. (2001) AAPM protocol for 40-300 kV x-ray beam dosimetry in radiotherapy and radiobiology. *Med Phys*, 28, 868-93.
- Pidikiti, R., S. Stojadinovic, M. Speiser, K. H. Song, F. Hager, D. Saha & T. D. Solberg. (2011) Dosimetric characterization of an image-guided stereotactic small animal irradiator. *Phys Med Bio*, 56, 2585–2599.
- Sheikh-Bagheri, D., & Rogers, D. (2001). Monte Carlo calculation of nine megavoltage photon beam spectra using the BEAM code. *Med Phys*, 29(3), 391-403.
- Stojadinovic, S., Low, D., Hope, A., Vicic, M., Deasy, J., Cui, J., & Khullar, D. (2007). MicroRT-Small Animal Conformal Irradiator. *Med Phys*, 34(12), 4706-5717.
- The TomoProcess, retrieved 04 18, 2012, from Tomotherapy.
- Townsend, D. W., & Cherry, S. R. (2001). Combining anatomy and function: the path to true image fusion. *European Radiology*, 11, 1968-74.
- Wong, J., Armour, E., Kazanzides, P., Iordachita, I., Tryggestad, E., Deng, H., . . . Deweese, T. L. (2008). High Resolution, Small Animal Radiation Research Platform with X Ray Tomographic Capabilities. *Int J Radiat Oncol Biol Phys*, 71(5), 1591-1599.

Research

1. IMPLEMENTATION OF A MICRO RESOLUTION DUAL GANTRY PRECLINICAL IMAGE GUIDED MICROIRRADIATOR: THE MICROIGRT

A. Introduction

The development of preclinical *in vivo* anatomical (microCT and microMRI) and functional (microSPECT, microPET, optical, and microMRI) imaging scanners contributed to a great advance in the development of radiopharmaceuticals and fundamental cancer research (Pomper and Lee 2005; El-Diery, Sigman et al. 2006). Equivalent progress in the fields of radiobiology, treatment planning, radiosensitizers, radiation therapy, and adjuvant chemo and radiation therapy are anticipated if dedicated preclinical microIGRT instruments are developed. In this article, we are presenting the implementation and commissioning of a small animal image guided microirradiator (microIGRT) based on a high resolution microCT for anatomical imaging and treatment planning and a submillimeter orthovoltage microirradiator for high resolution conformal microirradiation. The development of this instrument is the sum of a four year effort by our group toward its design, construction, characterization, and commissioning with phantoms and radiobiological animal models. The parametric and computer assisted design and numerical simulation of its operation to test the instrument design are reported in a companion article (Izaguirre, Birch et al. 2012). Both of the subsystems, the microCT and the microirradiator (microRT), have a separate gantry built to configure an instrument with coaxial architecture. This implementation has the benefit of allowing greater flexibility in the selection of the imaging and irradiation instrumentation best suited to achieve the highest performance for each subsystem without decision based mechanical or electrical constraints. As an example, the use of an independent microfocus source and higher resolution gantry motion for the microCT provides high contrast and imaging resolution, a constraint that is not feasible using the high power orthovoltage sources and heavier gantries required for the microRT components. Furthermore, flat panel sensors with small pixels do not tolerate high energy beams and will deteriorate (Lee, Kim et al. 2003).

These are the technical constraints which motivated our group to develop our instruments with a dual source and dual gantry architecture, as reported here.

The instrument architecture has a modular design that provides additional space for expandability to incorporate new imaging technologies, such as functional imaging, and to update the anatomical imaging capabilities to the latest available technology. This flexibility gives our instrument the additional function as a modifiable and upgradable research platform where new technologies and additional imaging modalities can be incorporated without disrupting the existing instrument functionality. A similar trend of coaxial and tandem operated architecture is currently followed by the major microSPECT, microCT, and microPET commercial and research instruments (Gleason, Austin et al. 2006; Jan, Ni et al. 2006).

The operation of our microIGRT resembles the work flow currently used in clinical practice to treat patients with external beam radiotherapy. This work flow includes simulation or tomographic scanning, treatment delivery formulation, dosimetric treatment verification, subject and planning target volume (PTV) positioning, portal imaging positioning and delivery verification, and treatment delivery. The technologies associated with this work flow in the clinical setting include a CT scanner or simulator, treatment planning station, immobilization devices for patient positioning repeatability, and clinical linear accelerators (linacs) with a portal imaging device and on-board cone beam CT. Each of these instruments is operationally independent and interconnected through the data transfer and handling computer network and software. Using the same work flow approach, we designed and developed our microirradiator system. However, in small animal radiobiological experiments, a significant difference arises in that all of these steps must be performed with the animal under anesthesia to avoid positional changes of the animal subject anatomy between anatomical imaging and irradiation. In preclinical research, the use of immobilization devices is limited (Kiehl, Stojadinovic et al. 2008) and has only been reported in a few cases of cranial irradiation (Clarkson, Lindsay et al. 2011). To achieve a high throughput from anatomical imaging and treatment, the instrument should have fast data interconnection and automatic animal handling between the anatomical imaging microCT, treatment planning, treatment verification, and radiation delivery. We developed our instrument by considering these requirements and designing a local network dedicated to handle the instrument control, dosimetric and imaging data processing, and treatment planning. Furthermore, software for all hardware and software operations was developed using a common C++

environment and file sharing protocols. This software and hardware architecture facilitates the work flow and enhances the instrument throughput by increasing the efficiency of all instrument operational processes and data communication between instrument subsystems.

The on-board microCT subsystem is a cone beam tomographic scanner constructed using a microfocus 80 kVp x-ray source and a flat panel amorphous silicon detector. The microRT subsystem was designed using a high power orthovoltage 320 kVp x-ray source. Each subsystem is sequentially operated, and a motorized animal bed transfers the murine animal model from the microCT imaging subsystem to the microRT subsystem. Treatment planning is performed during the transfer of the animal subject by using in-house developed treatment planning software.

For small animal treatments, we have utilized filters to provide significant skin sparing and to reduce the bone marrow depletion originated by enhanced photoelectric absorption at the bone from low energy x-rays. Our approach is to use an orthovoltage source operated at 300 kVp with a Thoreau's filter to eliminate photons with energies lower than 150 kVp. With this beam characteristic, skin sparing depth is comparable with a murine animal skin thickness and the absorption is predominantly Compton, consequently soft tissue and bone will have comparable energy absorption (Mayneord and Lamerton 1941; Izaguirre, Kassebaum et al. 2009). We would like to emphasize that a reduction in the dose delivered to the bone marrow in fractionated radiobiological experiments will not quench the generation of red blood cells (bone marrow depletion) which could destroy the animal models, and consequently data acquired to preclinically evaluate a treatment will not be biased by this biological effect.

In similarity with clinical external beam radiotherapy instruments, our instrument treatment subsystem was developed with an in-house developed micro electronic portal imaging device (μ EPID) for anatomical localization and positioning and portal beam delivery verification (Herman, Balter et al. 2001). These features provide a final submillimeter verification of the delivered beam and perform a highly accurate verification of the positioning and repetition of the treatment set up in a fractionated treatment. The μ EPID has a folded optical path between the scintillator and the sensor, to avoid radiation damage of the imaging sensor without moving shielding mechanisms (Price, Silviu et al. 2012).

The general overview of the instrument described in these sections demonstrates that there is a parallelism between our instrument and the clinical instrumentation utilized to image, compute treatment plans,

perform subject set up, and verify and deliver treatment. These closely related procedures greatly facilitate the interpretation and planning of radiobiological experiments and conclusions, which can be translated with greater efficiency to clinical trials.

B. The microIGRT mechanical implementation

The microIGRT's mechanical platform has been built using a modular structural system to allow for complete flexibility of the relative location between the microCT and microRT. The microIGRT instrument is shown in figure 1. Each gantry rotational motion assembly was constructed using the similar structural principle. A high precision turntable is mounted on the main instrument frame that supports the complete structure. The platform has a system of columns supporting the external fixed side of each turntable, and the gantry plate is mounted on the internal rotating ring of the turntable. The turntable of the microCT gantry can support a load of 16,782 kg and the microRT turntable can support a load of 27,215 kg. Both turntables were selected with the criteria of an axis shift less than 50 μm and a tilting angle smaller than 125 μrad . Both turntables have an opening of 11.5 cm to allow for the passage of the animal bed from the microCT side and passage of the high voltage cabling and cooling tubing in the microRT side. For the microCT, a conveyor belt guide is used to guide the cables when the gantry is rotating. For the microRT, a central guiding tube is used for the HV cables and cooling tubes which are placed along the isocenter to minimize the cable and tubing motion to simple torsion distributed along a 1 meter length. The microCT gantry can rotate continuously $1 \frac{1}{4} 2\pi$ rotation and the microRT can rotate $+(\pi+1/8 \pi)$ to $-(\pi+ 1/8 \pi)$ with respect to the home position.

The microIGRT resides inside a lead lined room. No additional shielding structure is required for the microCT beam, allowing for an open instrument for the microCT subsystem, which is very convenient for animal positioning and preparation. The microRT subsystem orthovoltage beam requires additional shielding, so the shielding enclosure was constructed using an aluminum framing system and lead panels, and an octagonal shape was used to minimize the amount of lead required to enclose the microRT gantry. The aluminum structure was built using the concept of an egg shell, where the walls contribute to the structural rigidity of the shell. To implement such a structure, the lead panels were encapsulated between aluminum sheets to increase their stiffness. To minimize lead dust environmental contamination, the panel

edges were painted prior to the aluminum encapsulation with a polymer sealing paint. The shielding has four doors that can be opened for instrument modifications or mechanical adjustments, and the interior of the instrument can be constantly overseen from the control desk by the user through two CCD cameras installed for this purpose. A third CCD camera is positioned to monitor the exterior, the CT section of the instrument, and the animal bed. The shielding has an axial opening located on the side of the microCT, to allow for the passage of the animal bed. The microRT shielding and the main frame are grounded for operator safety.

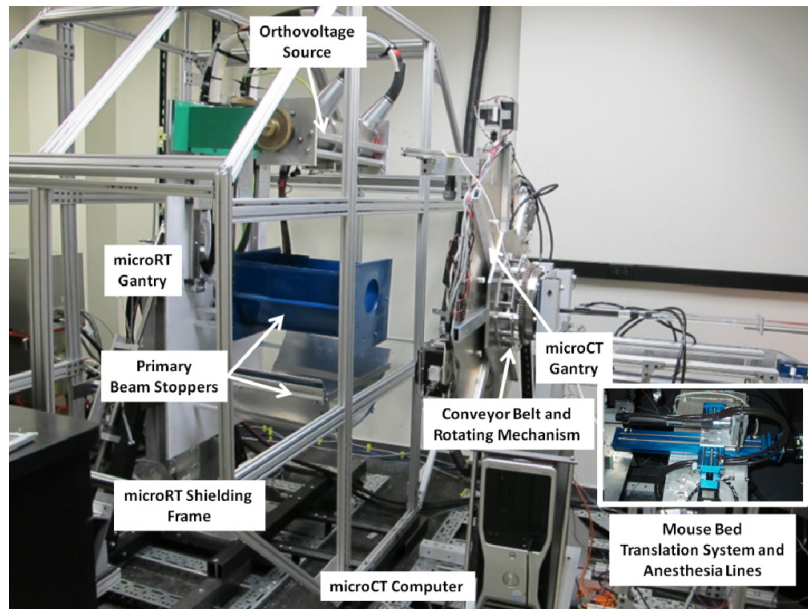


Figure 1. Image of the microIGRT during instrument construction. The image was taken during the instrument assembly before the microRT subsystem was shielded. The inset shows the animal bed translational x-y subsystem.

i. MicroCT implementation

The microCT gantry was constructed using an octagonal shaped plate reinforced with radial hollow beams connected to the turntable rotating ring through a central coupling plate. Along the gantry radial axis, two linear translation stages are placed at opposite sides. Each linear stage has a mounting plate where the microfocus x-ray source and detector are attached. The nominal mechanical resolution of the linear stages is 50 μm (McMaster-Carr 2012; Thomson 2012). There is space for two additional linear stages for instrument expansion or for imaging instrumentation development. To minimize the deflection of the linear stages originated by the imaging instrumentation weight, and to achieve a target resolution of 200 μm or

better, the linear slides have three supporting ball bearings which minimize the deflection of the imaging instrumentation and x-ray source to less than 25 μm .

On one of the slide mounting plates, we installed a microfocus x-ray source with a $75 \times 75 \mu\text{m}^2$ focal spot, 80 kVp maximum operating voltage, and 0.5 mA maximum current. This source was selected for our design considering that it has one of the smallest focal spots on the market for the intensity and kVp in the useful range of energies for the small animal imaging range of 30 kVp to 80 kVp. On the opposite slide mounting plate, a flat panel detector with a pixel size of $127 \times 127 \mu\text{m}^2$ was placed and aligned. The detector active area is $13 \times 13 \text{ cm}^2$, and the array consists of 1024×1024 pixels. These specifications correspond to small foot print Varian's PaxScan x-ray imaging receptors that have been optimized for the microCT source range of energies (Paulus, Gleason et al. 2000).

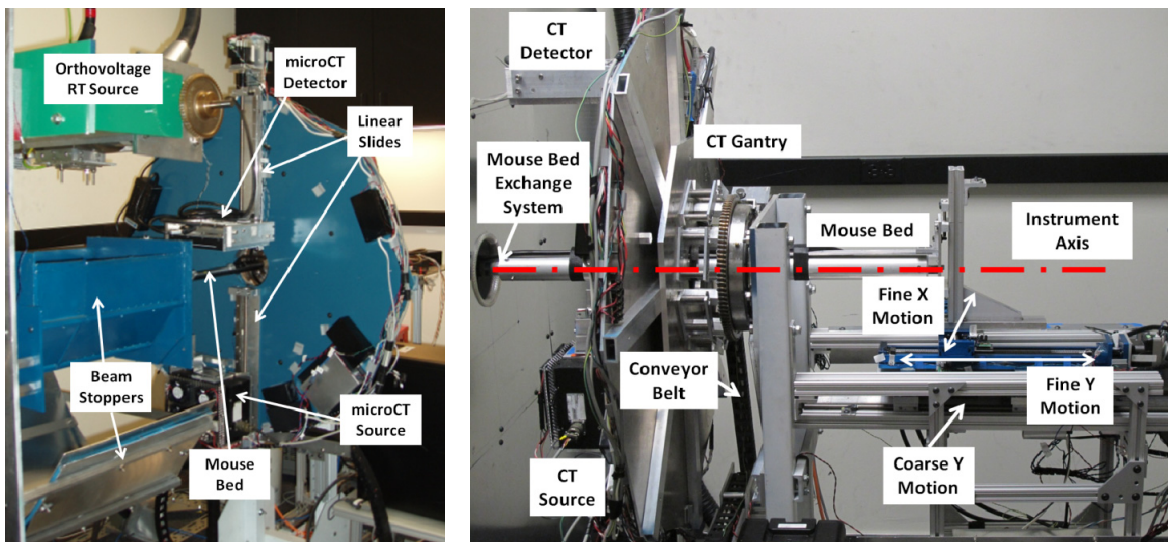


Figure 2. Images of the microCT subsystem. At the left, a front view of the microCT subsystem from the side of the microRT subsystem during microRT final construction. The micro focus x-ray source, slides, flat panel detector are indicated. At the right, a side view of the microCT, showing the instrument mouse bed x-y fine motion control slides, coarse long slide to transfer the animal from the microCT to the microRT, and instrument main axis (red dot-dashed line).

To precisely control the imaging time, and to avoid unnecessary dose to the animal during detector read out time, a mechanical beam shutter is placed at the output window of the source to control frame exposure during tomographic acquisition. The dose delivered to the animal model during imaging is reduced using a 0.75 mm thick aluminum filter. To further minimize the radiation dose and optimize the image contrast according to different animal sizes and species, the mechanical design allows for an easy exchange of the

filter. An image of the microCT subsystem constructed, using these specifications and showing details of their construction and location, is in figure 2. The flat panel detector was shielded to avoid radiation damage of the electronics from scattered x-rays.

ii. MicroRT subsystem implementation

The orthovoltage source is mounted on a specially designed rotating support that holds the source along its cylindrical enclosure. This supporting system has two ball bearings at each end of the holder that allow for the rotation of the source around its major axis. The holder has rubber pads at the ends to compensate for the differential expansion of the x-ray source with respect to the support frame originated by the source heating during operation. At the output window of the source is a filter holder where primary filters and the first collimator, a beam delimiting aperture, are installed. The filter is designed to cut off low photon energies and the aperture is to reduce the wide angle beam to 5.4 deg, which is the maximum beam divergence required for small animal irradiation. Following this delimiting aperture and the Thoreau's filter are two independent motorized orthogonal pairs of jaws, which are the secondary collimators. They are oriented perpendicular to the beam axis, in the x and y directions, to limit the beam size in each orthogonal direction.

The jaws, as shown in figure 3, were constructed using machinable tungsten plates (MITech 2012) and are translated using high precision linear ball bearing slides actuated by a programmable small foot print stepper motor and a micrometric screw with a nominal resolution of 25 μm . The third collimating element along the beam path is the BDMA which consists of a rotating wheel, where up to six tungsten-polymer molded micro apertures can be placed to shape the beam in any arbitrary profile (see figure 3). This architecture resembles the architecture of a linac, where a flattening filter, jaws, and multileaf collimators (MLC) modulate the linac beam.

There are two beam stoppers located opposite the x-ray source, across the axis of rotation of the instrument. The first lead beam stopper encloses the volume where the animal is irradiated and is where the μEPID is installed. This beam stopper shields the primary beam and the scattering originated from the animal, animal bed, and the μEPID . The second beam stopper has a thickness of 12.7 mm and provides the final shielding

of the primary and scattered beam. Both stoppers counterbalance the x-ray source torque to minimize motor effort in rotating the gantry.

The μ EPID was assembled using a high resolution low noise CCD camera with 1392x1040 pixels, a wide acceptance angle high resolution paraxial lens, and a fast gadolinium oxysulfide scintillator. The μ EPID can be used to determine the beam fluence and profile before and after it crosses the irradiated animal subject for beam fluence verification and absorbed dose determination, and to acquire anatomical images of the loco regional anatomy of the irradiation site. Further details pertaining to the μ EPID are presented in a following chapter.

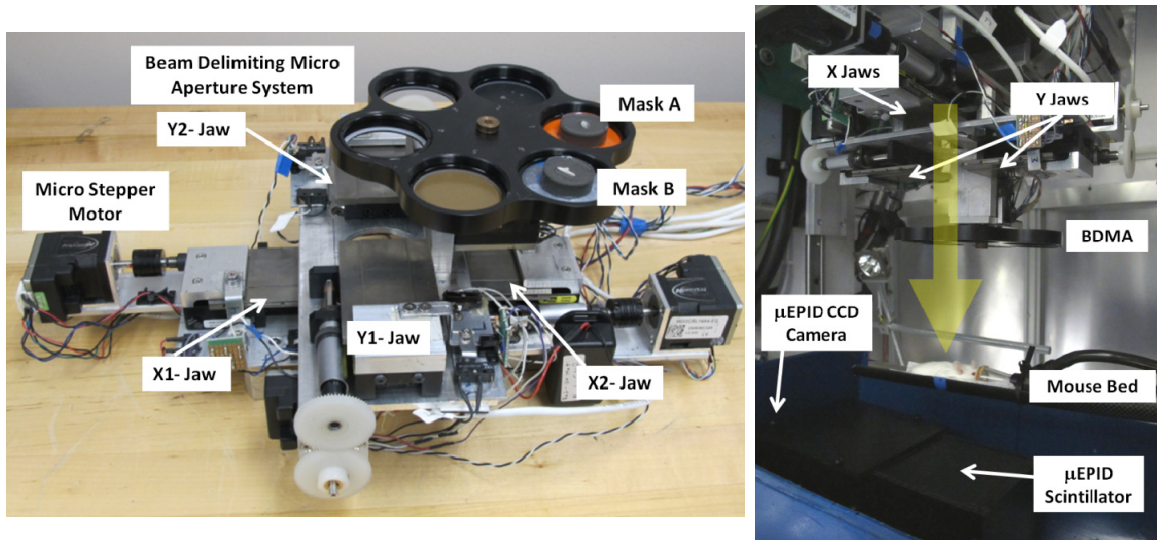


Figure 3. The microirradiator chamber and delivery system. At the left, a view of the jaws and BDMA to collimate and intensity modulate (step and shoot) the microRT treatment beam. At the right, a view of the microRT treatment chamber showing the location of the jaws, BDMA, mouse bed, and μ EPID at the moment of an animal irradiation. Yellow arrow indicates the beam path.

iii. Instrument controlling and data processing hardware

The instrument controller and data processing hardware consists of a local network where two command input computers are located at the exterior of the lead lined room on the operator countertop to control the instrument through input commands during the instrument operation, and two instrument computers (a microCT and microRT computer) are located inside the lead lined room to execute the commands transferred from the control computers. Additionally, there is a server connected to this local network to process the microCT image reconstructions and perform the treatment planning with high efficiency.

A diagram of this network and the instrument main electronic components is shown in figure 4. All the computers operate the instrument using a common program developed using visual C/C++ and specific C libraries from each electronic imaging and radiation device. This software and hardware architecture has high efficiency and facilitates development with no bottle necks in data sharing, where parameter files are continuously shared by computers to synchronize each instrument subsystem during all the experimental steps required for imaging, treatment planning, and treatment verification and delivery.

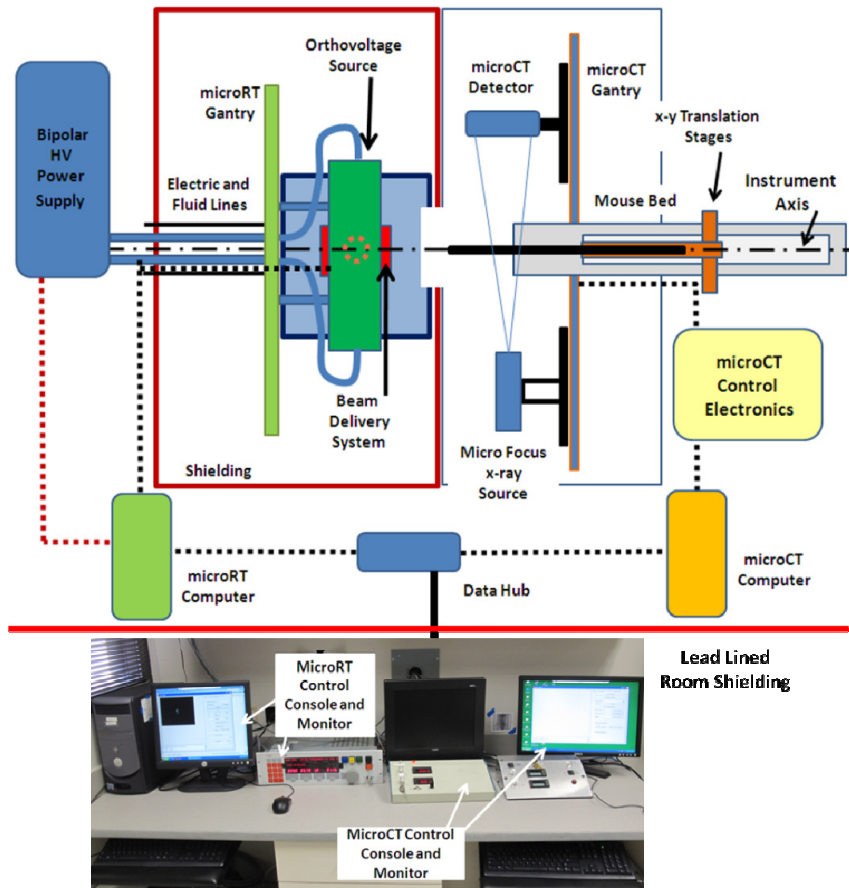


Figure 4. Block diagram of the instrument interconnection for instrument control and data handling. The diagram shows the hardware components. The lead lined room and microRT subsystem shielding are indicated to show instrument shielding barriers. Not shown in detail, the microRT beam delivery system and μ EPID for drawing clarity (see figure 3 for these components).

iv. *The animal bed and physiological interface*

Three motorized translation stages are used to position the animal in the microCT field of view for tomographic data acquisition and then position the animal in the irradiation beam where the target volume can be centered for isocenter or iso-distance irradiation techniques. Images of the animal bed and its

positioning system are included in figures 1 and 2. The animal holder was constructed using carbon fiber components to have minimal radiation absorption (radio-transparency) with high enough rigidity to support the animal weight. The animal bed and physiological interface have an isoflurane anesthesia non-rebreathing system to provide anesthesia to the animal during the imaging, treatment planning, and treatment delivery phases. The anesthesia is regulated using a high precision flow meter that is constantly monitored from outside the lead lined room. Two focused infrared lights are installed to warm the animal inside the irradiation chamber and keep the animal temperature in the range of normal physiological values, which will avoid animal hypothermia.

For high throughput, the animal bed is designed with an attach-and-release mechanism that facilitates exchange of the animal bed without perturbing the animal posture. To be able to perform multimodality radiobiological studies, connectors for the animal bed, anesthesia, and physiological sensors are compatible with other imaging instruments at Washington University such as microPET, microMRI, and optical imaging. This implementation of the animal bed facilitates imaging co-registration between different imaging modalities and the microIGRT anatomical images and treatment plans.

v. *Instrument software*

The instrument control and data acquisition software is based on Visual C++, national instrument libraries for the C and C++ language, and the Microsoft foundation class for the development of the visual interface shown in figure 5. The visual interface has a data imaging window and a series of panes to activate each main component of the instrument operation (software modules), which includes the microCT, microRT, portal imager, and mouse bed. During microCT positioning, the imaging window shows the acquisition of the projections in real time. During microRT operation, the imaging window shows portal images acquired to make final corrections to the animal positioning for irradiation. Each software module handles imaging data and files containing instrument operation parameters. The images are processed using an in-house image processing program developed to reconstruct microCT data, format changes, and perform image overlay and linear image transformations. The treatment planning computes the treatment according to input parameters such as number of beams, beam micro apertures, beam weight, cross section, reconstructed animal anatomy, and source parameters such as beam current, kVp, beam time on, and source

and gantry positioning. The treatment planning output parameter file is later accessed by the microRT software module to perform the irradiation delivery. This treatment planning process performs a fast elaboration of an irradiation plan and performs its delivery in a semi automatic procedure that improves animal throughput.

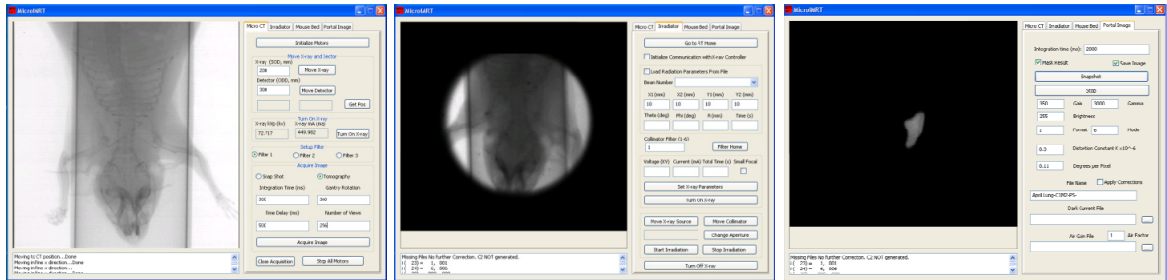


Figure 5. Diagram of the instrument software developed to handle the instrument functions. The interface consists of an object oriented software module for each subsystem, the microCT (left), the microRT (center), the μ EPID (right), and the animal bed (not shown). These modules are combined in a single main program where the visual interface is organized in dedicated data visualization and instrument control windows for each subsystem.

C. Methods

i. Testing the microCT subsystem imaging capabilities

We tested and optimized the microCT resolution and contrast using micro-resolution phantoms, and we used animal models to evaluate the instrument anatomical image quality. Two cylindrical resolution phantoms were specially built for this purpose, a wire phantom and a plexiglass micro-resolution phantom. A mechanical diagram of the resolution phantoms and their microCT images are shown in figure 6. The wire phantom consists of an arrangement of tungsten wires organized at the vertex of a pentagonal prism. The plexiglass micro-resolution phantom has five hole arrays organized in angular sectors according to their hole sizes in a plexiglass cylindrical body as a tissue surrogate. Phantom images were used to determine the resolution as a function of the incremental dose delivered when the numbers of projections were 512, 256, and 64. These projection values are the result of progressive pixel binning to reduce the original detector matrix of 1024 to form a data cube for isotropic image reconstruction according to the number of angular projections taken. The dose was determined with a 0.04 cm^3 micro ion chamber (Scanditronix and Wellhoffer, 2012) and a CNMC K602 electrometer (CNMC, 2012).

The microCT contrast was determined using a phantom developed for this purpose using five rods of different density materials, which include LDPE, Delrin, acrylic, Teflon, and polystyrene. Their respective

HU units are -100, 340, 120, 990, and -35, positioned following a pentagonal arrangement, enclosed in a water cylinder and. A diagram of this phantom is included in figure 6.

The microCT anatomical imaging quality was assessed using animal carcasses and *in vivo* animal subjects. We focused on two anatomical sites, the brain and lung. The brain was selected as a representative element of treatments where internal motion is minimal, and the lung was chosen to represent when respiratory motion can reduce image quality and organ visualization. This selection covers a broad range of preclinical experimental conditions where the microIGRT instrument will be utilized.

ii. Test of the microirradiator beam quality and fluence distribution

To test the microirradiator orthovoltage beam quality, we determined the half value layer (HVL) equivalent energy by measuring the beam transmission through increasing thicknesses of aluminum or copper, depending upon the beam energy, as described by Ma et al (Green, Seidel et al. 2001) for orthovoltage beams delivered at the source operating potentials of 120 kVp, 225 kVp, and 300 kVp. The orthovoltage beam dose was measured using an ionization chamber (Scanditronix and Wellhoffer 2012) inserted in a tissue equivalent material phantom with the diameter equal to a typical mouse, 25 mm. The dose rate was assessed for the beam sizes of 0.5x0.5 cm², 1x1 cm², 1.5x1.5 cm², and 2x2 cm² and output factors were defined as a function of the beam size and normalized to 1x1 cm² field. Ion chamber data was used to perform a dosimetric calibration of the radiochromic films for the subsequent beam dose distribution measurements.

To test the performance of the beam modulation subsystem (jaws and BDMA) and the properties of the treatment beam modulated using this device, we measured the percent depth dose (PDD), beam profiles, penumbra, asymmetry, homogeneity, and dose rate. These tests were performed using tissue equivalent phantoms and radiochromic films inserted in the phantoms at multiple longitudinal planes located at incremental depths across the phantom. The radiochromic films' dosimetric calibration was performed using a set of phantoms in which the ionization chamber was placed at three different phantom body depths, 6.35 mm, 12.7 mm, 19.05 mm, to perform a three point calibration along the PDD curve.

The beam homogeneity and symmetry were determined by scanning and analyzing the beam profile as measured with radiochromic film (Kutcher, Coia et al. 1994). These measurements were performed in

beams with cross sections of $0.5 \times 0.5 \text{ cm}^2$, $1 \times 1 \text{ cm}^2$, $1.5 \times 1.5 \text{ cm}^2$, and $2 \times 2 \text{ cm}^2$. These measurements were also checked against beam images and profiles acquired with the μEPID , to assure self consistency in our measurements and to dosimetrically calibrate the μEPID for future on line beam verifications.

The jaw mechanism motion was tested for beam size accuracy using beam fluence images acquired with the μEPID . Fluence distributions, homogeneity, and penumbra of the beam modulated to an arbitrary shape by the BDMA were determined with the μEPID . Two tungsten-polymer molded masks were developed for conformal irradiation of the right lung of a mouse, with one mask designed for AP/PA irradiation, and one mask designed to modulate an oblique beam. Masks were designed to minimize dose spill off to the heart and esophagus. Brain glioma irradiation was tested using a generic tungsten-polymer molded circular mask that conformally delimits the irradiation beam to the tumor.

iii. Tests of the beam positioning accuracy for multibeam and fractionated treatments

Beam delivery accuracy for the translational and angular directions were performed using tissue equivalent phantoms with radiochromic films inserted along the principal planes of symmetry. To determine the positioning accuracy according to coordinates specified by the treatment software along the instrument axis, we irradiated a cylindrical tissue equivalent mouse sized phantom with radiochromic films at its center plane along the instrument axis with thin 1 mm wide beams spaced in steps of 2 mm along the axis. The beam spacing was measured in the radiochromic film to determine beam delivery positional accuracy. Other translational delivery coordinates were tested using similar methods. Angular delivery coordinate precision and accuracy were determined using a process equivalent to a linac quality assurance gantry start test (Kutcher, Coia et al. 1994; Klein, Hanley et al. 2009).

To determine the accuracy of treatment fractionation, the on-off effect was determined for the microRT source. The dose rate was determined for a 300 kVp filtered treatment beam to evaluate the time required to deliver 2 Gy. An ion chamber in a build up cap was placed in the mouse bed and irradiated for 2 Gy. The output was recorded and this process was repeated 20 times, to simulate a typical 20 fraction, 40 Gy total dose treatment which was compared with a single 40 Gy fraction.

An important mechanical requirement in our system is to have high accuracy in the transfer of the animal from the microCT imaging system to the microRT, which will guarantee correct delivery of the dose to the

planned target volume, interfraction positioning repeatability, and treatment fractionation accuracy. The function of the μ EPID is to perform final portal beam verification and micrometric resolution final adjustments, if necessary, after the animal has been positioned in the microRT irradiation chamber.

In vivo treatment repeatability tests were performed using a marker on the animal bed to discern the variation of the mechanical positioning and the animal shift. To determine the accuracy in animal repositioning during a treatment, we performed irradiations of a mouse model with a glioma brain tumor and a fractionation schedule that consisted of 20 fractions with 2 Gy per fraction. The animal anatomy and beam images were coregistered with the portal imaging device. The upper rim of the eye sockets, the mid cranial lines and the posterior joint of the cranio-spinal cord were used as bony landmarks to define portal beam positioning and verification. The aim of this test is to show that fractionated irradiation can be performed with a resolution higher than the required precision of 200 μ m based on typical organ boundaries extracted from high resolution anatomical MRI images animal data (Umlaut 2012). A similar process was used to determine the localization and interfraction variation in a lung irradiation where organ internal motion is a concern.

iv. Treatment planning and treatment delivery evaluation

Anatomical microCT images were transferred to the treatment planning system and used to generate treatments for implanted glioma tumors and right lung irradiation to study healthy tissue response to ionizing radiation and radiation induced complications. Glioma cells were implanted in the brain hemisphere to construct a preclinical tumor model designed to study novel adjuvant chemo-radiotherapy treatments. The treatment planning for the lung is an example of a preclinical model to study healthy tissue response and complications induced by ionizing radiation. For the glioma model and the lung irradiation, the beam was modulated by combining the collimator jaws and the BDMA. The instrument is also used with jaw modulation alone when conformality is not of great concern, such as in xenograft breast tumor models. Treatment plans were optimized by scaling the beam size and intensity. Conformality of the dose distribution is visualized using the CT projection image of the animal anatomy and PTV. Predictions of the treatment plan were compared with the dose delivered to a point measured with ion chambers (Green, Seidel et al. 2001) and the dose profiles using orthovoltage calibrated radiochromic films.

We tested the instrument capabilities to deliver multibeam microconformal treatments with masks generated using the microCT projection images of the PTV boundaries (beam's eye view). Initial verification of the dose delivered to a phantom was performed using radiochromic films and ionization chambers inserted in a phantom that represents the section of the animal body to be irradiated. A body phantom, 25 mm diameter, and a head phantom, 18.75 mm, were used for this purpose. Films were irradiated with the multibeam treatments for a total dose of 2 Gy at the center of the PTV. The treatment plan calculations were compared with the calibrated films and ionization chamber readings to validate the treatment plan dose estimations. To have a fast dose verification method for high throughput microirradiation experiments, the μ EPID device was used as an imaging transmission dosimeter. Using the dosimetric calibration presented in the next chapter, we validated the beam dosimetry in the examples shown in the following sections.

D. Results

i. MicroCT imaging tests

Measurements for the determination of the microCT image resolution using the wire and micro resolution phantom are reported in figure 6. The wire phantom shows that a 50 μ m wire can be imaged, and the high resolution acrylic phantom shows that the 0.5 mm array of holes can be imaged in a volume of 10 cm length and 5 cm diameter. This volume encloses the imaging space required for experiments that we anticipate will be performed using our microIGRT instrument. We determined the modulation transfer function (MTF) from the line square function using a tilted tungsten wire phantom (Fujita, Tsai et al. 1992). The analysis of the MTF shows that the system has a maximum resolution of 4.65 line pairs per mm for 512 images.

The measurements of the microCT imaging dose as a function of the angular projection sampling, or resolution, using cubic voxel space provided the following results: the dose and resolution are 4.15 cGy and 790 μ m/pixel, respectively for 64 images, 16.62 cGy and 201 μ m/pixel for 256 images, and 33.24 cGy and 100 μ m/pixel for 512 images. Consequently, 64 image microCT scans provide a quick and low dose reconstruction when very high resolution is not necessary, such as for large tumor localization or scout imaging. 512 image microCT scans provide excellent high resolution reconstructions (Izaguirre et al.,

2005), however the dose is higher. For every day imaging, we determined that 256 volumetric microCT images are a good compromise between dose and resolution and satisfy the 200 μm resolution required of most of our small animal irradiation projects. We also performed calibration of the microCT with a contrast phantom and an image of this phantom is shown in figure 6.

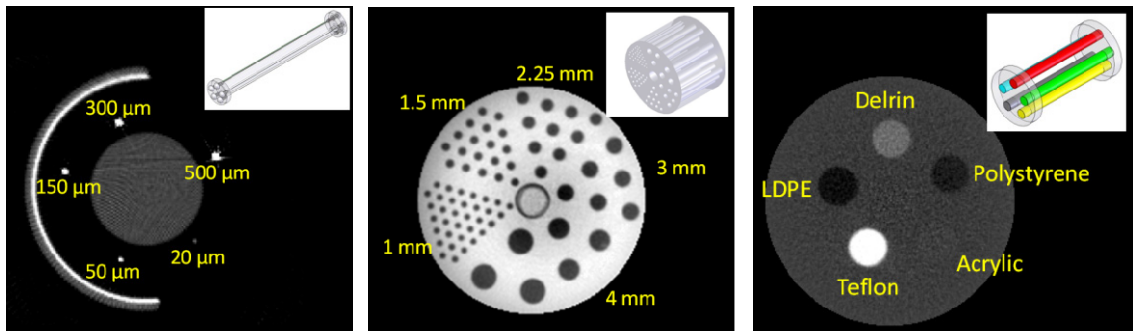


Figure 6. In-house developed microCT phantoms to test the microCT resolution and contrast in the microCT imaging volume (50 mm diameter and 100 mm length). Left: Five tungsten wire phantom. Center: Acrylic resolution phantom. Right: Five material contrast and HU calibration phantom.

An example of a 256^3 pixel microCT resolution image of an animal cranial anatomy is shown in figure 7. These images show that small features, such as the 500 μm skull wall thickness, is clearly visible. An image of the lung showing the bronchial tree is also included in figure 7. The smallest visible structure in the lungs is a branch of the bronchial tree, with a diameter of 600 μm . These images show appropriate resolution and contrast between the different tissues.

Following the phantom calibration, we performed a test for the assignment of HU to bone, muscle, and lung tissue. The results of this test showed that the assignment can be performed without noticeable erroneous pixels. The HU calibrated images are used in treatment planning to perform dose computations. The presented resolution and contrast phantoms are periodically used to perform microCT dose verification and imaging hardware and software quality assurance.

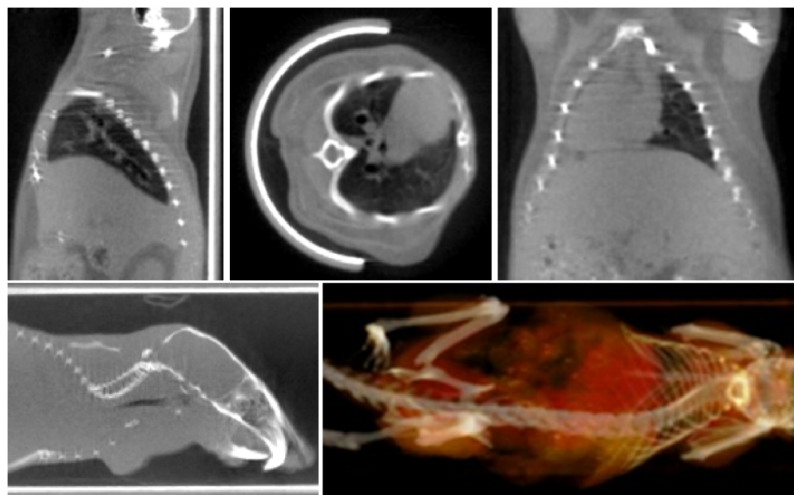


Figure 7. Examples of microCT image capabilities to determine animal anatomy. On the top row, we show a microCT scan of a rodent thorax anatomy. At the bottom left, a sagittal image of the head anatomy, and at the bottom right, a translucent rendering of the animal body.

ii. Microirradiator beam characterization

Results of the microRT subsystem testing include penumbra, beam asymmetry, homogeneity, and PDD to determine irradiation beam characteristics. The HVL for treatment beams, 225 kVp and 300 kVp, and for the imaging beam, 120 kVp, for both filtered and unfiltered beams are shown in table 1, and figure 8 illustrates the change in dose fall off due to filtering for the 300 kVp beam. The filter used for imaging is filter 1, which consists of 0.75 mm of Al. Filter A, used for treatment, consists of 0.8 mm of Sn, 0.5 mm of Cu, and 1.5 mm of Al.

Table 1. HVL for most commonly used source potentials. 120 kVp filter – 0.75 mm of Al. 225 kVp and 300 kVp filter - 0.8 mm Sn, 0.5 mm Cu, 1.5 mm Al.

	Unfiltered	Filtered	Filter Name
120 kVp	0.162 mm Al	2.694 mm Al	Filter 1
225 kVp	0.181 mm Cu	2.875 mm Cu	Filter A
300 kVp	0.435 mm Cu	3.875 mm Cu	Filter A

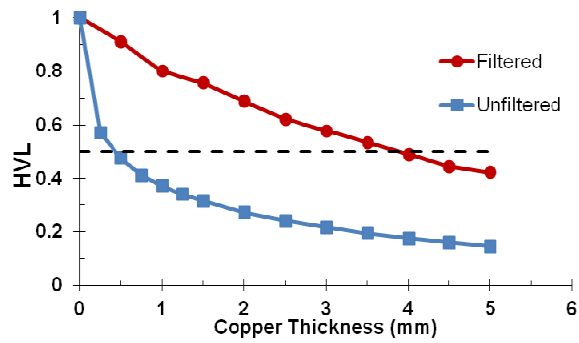


Figure 8. HVL for 300 kVp, filtered and unfiltered. 50% intensity dashed line. Filter composition: 0.8 mm Sn, 0.5 mm Cu, and 1.5 mm Al.

Results of the microirradiation beam symmetry, homogeneity, and penumbra are shown in table 2, for the 300kVp filtered beam (3.9 mm of Cu HVL) for different beam sizes. Figure 9 illustrates the beam profiles for $0.5 \times 0.5 \text{ cm}^2$ and $1.5 \times 1.5 \text{ cm}^2$ fields, in both the x and y directions.

Table 2. Beam homogeneity, symmetry, and penumbra for four field sizes.

Field Size [cm^2]	Direction	Homogeneity [%]	Symmetry [%]	Penumbra [μm]
0.5x0.5	x	9.8	11.8	207
	y	7.2	9.8	150
1x1	x	7.0	8.5	265
	y	7.0	8.6	178
1.5x1.5	x	8.0	8.5	257
	y	6.7	7.7	188
2x2	x	4.8	7.9	256
	y	5.3	6.7	209

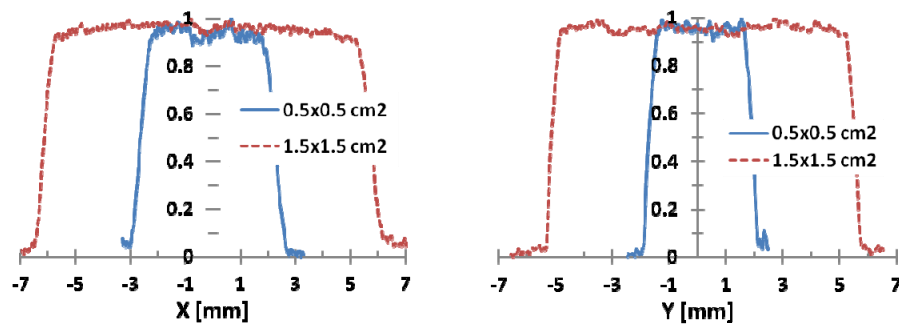


Figure 9. The x and y direction beam profiles for $0.5 \times 0.5 \text{ cm}^2$ and $1.5 \times 1.5 \text{ cm}^2$ square beams

The dose rate versus field size was determined for the 225 kVp and 300 kVp beams. The filtered beam was collimated with the jaw system to four common field sizes, and the dose rate was determined with a CC04 ion chamber. The results are shown in figure 10 and the output factor is normalized to the 1x1 cm² field, which is the reference beam for instrument QA.

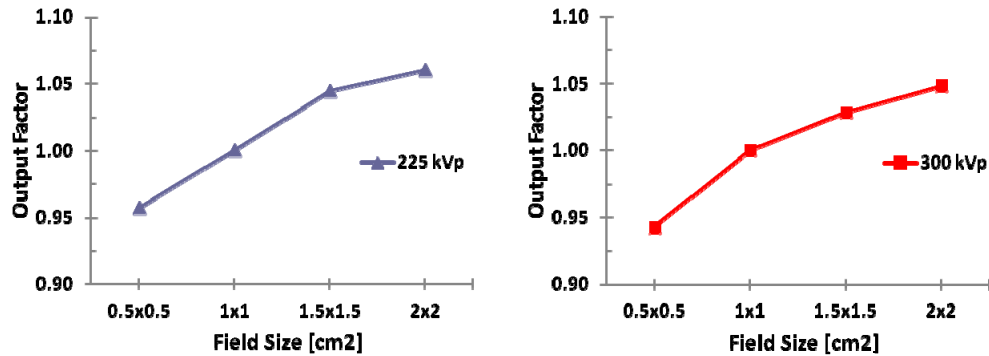


Figure 10. Output factor for 225kVp (left) and 300 kVp (right) beams. Beams are filtered with the standard treatment filter, 0.8 mm Sn, 0.5 mm Cu, and 1.5 mm Al.

In order to determine accurate beam dose distribution throughout the animal, the beam profile was evaluated with radiochromic film and a CC04 ion chamber. The ion chamber was used to determine the dose at three points across the subject, and the film was used to determine the shape of the dose distribution with 10 points across the subject. The dose distribution was scaled to match the actual dose, as shown in figure 11, for three beam energies and both the filtered and unfiltered beams are shown for each energy. The dose curve was fitted with a combination of linear and exponential values for the filtered and unfiltered beams at 120 kVp and 225 kVp. The filtered 300 kVp beam was fitted with a 6th degree polynomial due to the 3 mm build up region of the PDD. The lower energies do not experience this build up region, nor does the unfiltered 300 kVp beam.

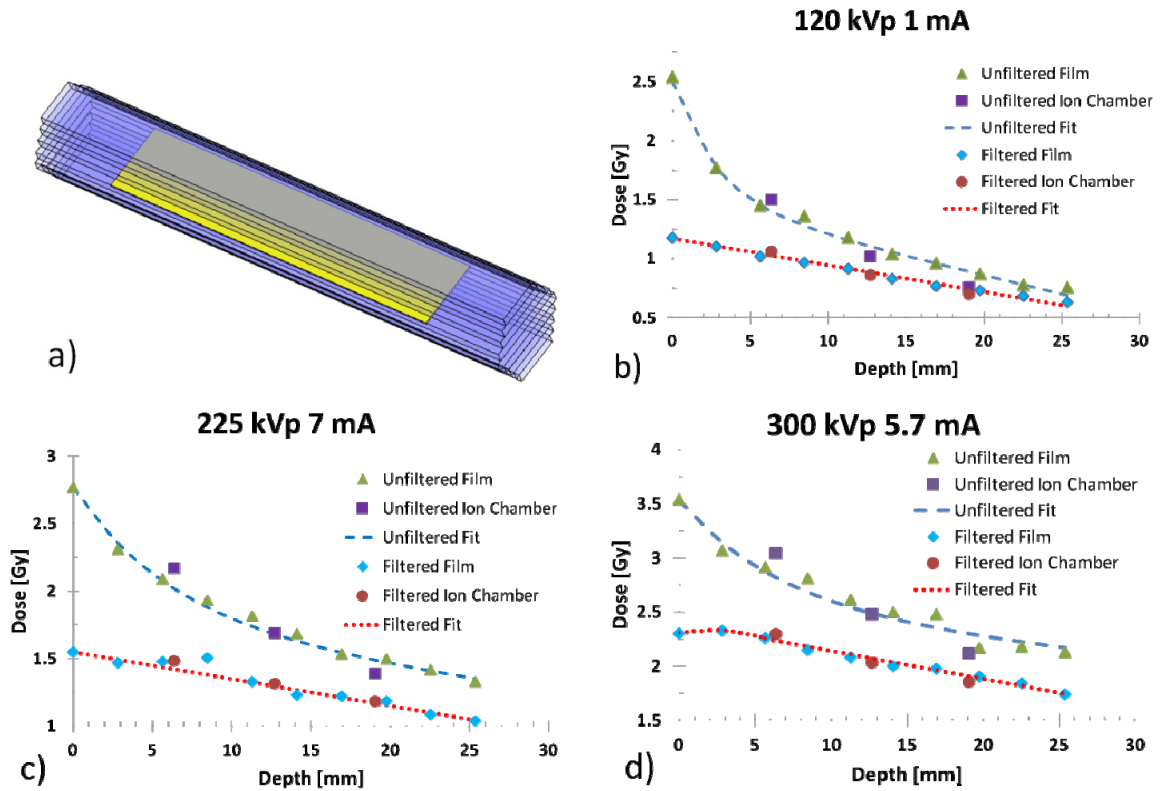


Figure 11. Phantom to determine PDD and results for filtered and unfiltered 120 kVp, 225 kVp and 300 kVp beams. a) PDD phantom with 10 points of measurement with radiochromic film. b) 120 kVp, 1 mA. c) 225 kVp, 7 mA. d) 300 kVp, 5.7 mA.

iii. Irradiation positioning delivery accuracy

The beam delivery spatial accuracy was determined to be $\pm 50 \mu\text{m}$ using a multiple sequence of narrow beams delivered to radiochromic film. These measurements are in agreement with the manufacturer specifications for the animal bed motion slides with $50 \mu\text{m}$ accuracy.

The source on-off effect was evaluated to determine the accuracy of fractionated treatments. A single dose versus a 20 fraction dose comparison shows a 2.4% overdosing with respect to a single fraction. This effect is corrected in the treatment plan by adjusting each fraction to match the single fraction treatment.

Results of the interfraction transverse and longitudinal positioning repeatability analysis in fractionated treatments are shown in figure 12, for a brain and lung irradiation experiment. In this test, the distance between a known bony landmark and a beam boundary was measured in both directions for each fraction and plotted against the expected planned value in each direction. The acceptable positioning error of $500 \mu\text{m}$, (scaling a nominal 6 mm accuracy from clinical treatment plans to small animal scales) has been

plotted as the tolerance limit in figure 12. The lung positioning repeatability varies a great deal more between fractions than the brain repeatability because of the increased motion in the thoracic cavity due to respiratory and cardiac motion, which results in a poorer definition of the bony landmarks with respect to the beam. In the brain, there is very little motion, leading to improved repeated positioning, well within the tolerance limit for 95% of the fractions.

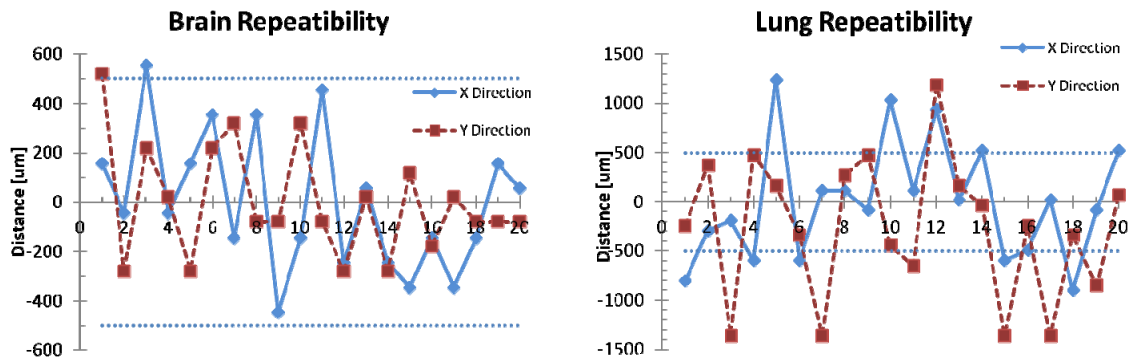


Figure 12. Irradiation conducted over 20 fractions. Each point represents the distance from the bony landmark of reference and expected planned value. 500 μm tolerance (dotted line) is scaled from clinical human irradiations (30 cm diameter) to mouse irradiations (2.5 cm diameter). Each point represents distance from bony landmark to edge of beam in x and y directions. Left: Brain irradiation, scale has been magnified for clarity. Right: Lung irradiation.

iv. *Multiple beam isocenter technique irradiation precision*

In order to determine the accuracy of delivering isocentric radiation to an animal with a multiple beam treatment, we performed a study using radiochromic films with parallel opposed beams, a four field box, three equally spaced beams, and five equally spaced beams. The beams were defined using the collimator jaws to deliver $5 \times 5 \text{ mm}^2$ beams for all experiments. A result of this evaluation is shown in figure 13. This test shows that multiple beam irradiations can be performed with an angular precision of 0.1 degree. For a two beam (AP/PA), three beam, four field box, and five beam irradiation, the beam isocenters are repeated within a circle of dispersion of 150 μm , 77 μm , 203 μm , and 115 μm , respectively. Three beam irradiations have lower isocenter dispersion than two beam irradiations because its theoretical isocenter can be defined more accurately. The same effect occurs between the four and five beam irradiations. Four beam irradiations have lower dispersion than five beam irradiations because the higher numbers of beams increases the isocenter circle of dispersion. Figure 13 also shows the submillimetric conformal distribution of the beam dose fall off outside the target volume.

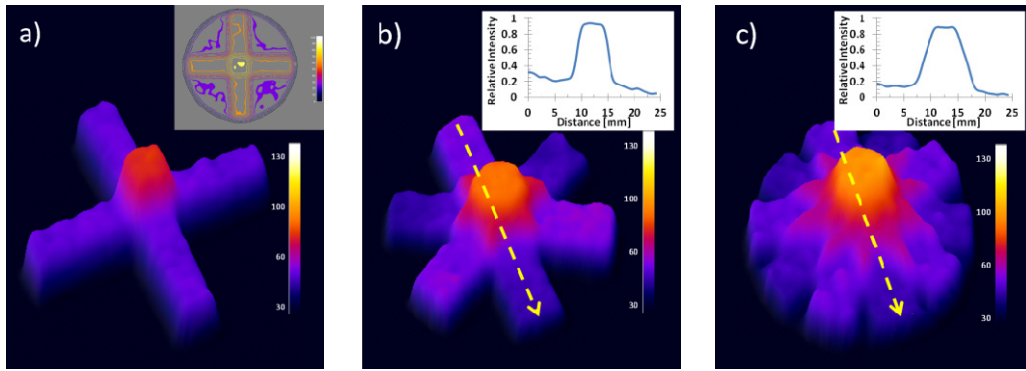


Figure 13. Test of the multiple beam irradiation of phantoms to determine the precision in localizing the treatment using isocentric irradiation. a) Four field box with isocontour inset. b) Three beams with line profile inset. c) Five beams with line profile inset.

v. *Validation of the treatment planning and treatment delivery*

We tested the capability of the treatment planning software to formulate conformal treatments delivered using the BDMA subsystem. In figure 14, we show the results of the process of formulating masks from microCT images and the dose profiles computed by the treatment plan. The figure shows that the dose profiles are highly uniform across the beam, with a very sharp beam penumbra of 500 μm .

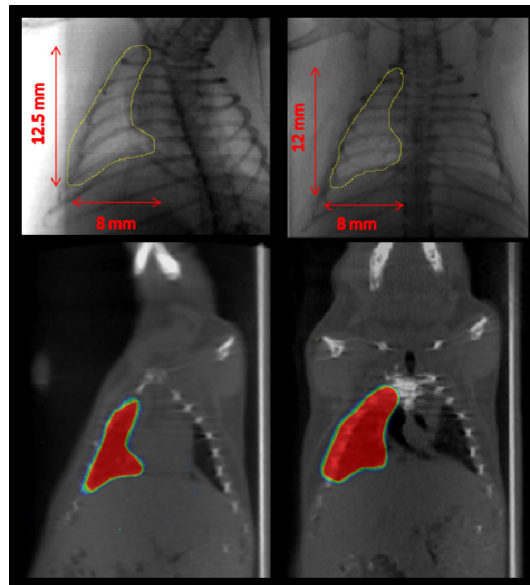


Figure 14. Formulation of a treatment using masks generated from rodent lung microCT images. Top row: Contoured masks using microCT projection data. Masks are formulated to avoid irradiation of the heart and esophagus. Bottom row: Treatment planning computed dose profiles of the beam in beams eye view projections. The figure shows the AP/PA beam in the right column and a right posterior oblique 45 degree beam in the left column.

The dose distribution computed by our treatment planning system indicates that the beam conformally follows the anatomy of the reconstructed microCT images. The irradiation parameters determined by the

treatment plan were used to operate the microRT and deliver the dose to an animal sized phantom. The measured dose corroborates that the treatment planning software can compute the dose with an error less than 5% with respect to ion chamber measurements, and the dose distributions match closely radiochromic film measurements.

We validated the delivery of conformal treatment computed with treatment planning and delivered with the BDMA using μ EPID portal images overlaid with the animal anatomical images for the two cases of study, brain gliomas and healthy right lung irradiation. Results of the validation of these multibeam treatments are shown in figure 15. In this figure, we present the portal imaging of the brain treatment where the tumor was localized using bioluminescence imaging, and the treatment was performed using three beams directed to the tumor and modulated with a 3 mm diameter circular mask.

In the same figure, we present the portal imaging verification of a treatment designed using the lung masks shown in figure 13. Image coregistration shows that a highly conformal treatment is delivered to the animal lung, and the esophagus and heart are spared. The central dose point was determined with an ion chamber in a phantom and with the calibrated image of the μ EPID. The overall dose determination error for both experiments is within 5%. Beam measurements with orthovoltage calibrated radiochromic films also support these results.

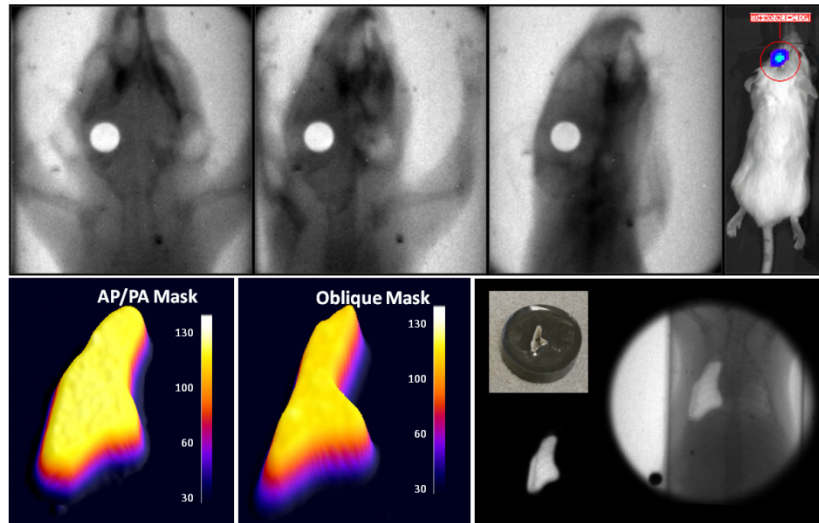


Figure 15. Top row: Verification of the microirradiation of a glioma tumor implanted in the right brain hemisphere. The irradiation was performed using a generic circular mask installed in the mask exchange system, and final positioning was performed using the μ EPID. Positioning resolution is 300 μ m and dose at tumor is 2 Gy per fraction. At the far top right, an optical image of the tumor to assess treatment response. Bottom row: Verification of delivered dose distributions using calibrated radiochromic films in a right lung irradiation example. At the bottom right, the AP/PA field mask and a beam portal image coregistered with the animal anatomy.

E. Discussion and conclusions

The work flow of the microIGRT was established using the methodology used in clinical external beam radiotherapy translated to animal handling procedures and special requirements to construct radiobiological models of cancer radiotherapy and tissue complications (Kiehl, Stojadinovic et al. 2008; Yuan, Holmes et al. 2010).

A clear advantage of the dual gantry architecture is that the animal is transferred from the microCT to the microRT while keeping the animal subject in precisely the same position during imaging and treatment. Consequently, motion from the microCT imaging is reduced to a nearly negligible value. This guarantees a successful microirradiation correlated with treatment planning, as shown in the lung irradiation example. Additionally, the precise positioning capabilities of both the software and hardware position the animal subject in nearly the same set up for each fraction, reducing interfraction motion to less than 500 μm for most of the fractions, especially in brain irradiation experiments where organ internal motion is minimal.

By constructing an independent microCT and microRT on a common platform, we were able to implement each subsystem with the most adequate x-ray sources and imaging components according to the requirements for anatomical imaging and microirradiation. The testing of the system corroborated this technical advantage by demonstrating high resolution microCT images using a microfocus source and amorphous silicon panel detector, the formulation of accurate treatment plans during animal transfer, the accurate delivery of orthovoltage beams to the PTV using a powerful source, high treatment conformality and accurate treatment doses using beams modulated by a novel BDMA, and verification of a treatment with an specialized μEPID imaging system. The reported data in this article demonstrates that anatomical imaging and treatment delivery can be performed with a precision and conformality that is comparable with current clinical treatment protocols, if they are compared using a factor of 10%, based on the size aspect ratio between mouse and human anatomy. Measured dose distributions show that skin sparing, low dose to the bone marrow, highly conformality to a PTV and adequate PDD profiles are achieved with the microIGRT to deliver clinically equivalent treatment in animal models of cancer.

A principal component of this instrument's microRT subsystem is the beam modulation capability designed with clinical similitude in mind, using jaws and micro apertures that mimic the clinical step-and-shoot external beam irradiation technique. This allowed us to use our experience gained in clinical treatment

planning for small animal preclinical research, with the aim to design and perform radiobiological experiments with a clear translational path to clinical protocols for a phase I clinical trial.

Currently the microIGRT is used in our institution to perform drug testing, investigate novel radioprotectors and radiosensitizers for brain gliomas, adjuvant chemotherapy and radiotherapy treatment of brain gliomas, investigate the onset of radiation induced side effects to establish an animal model of lung pneumonitis and fibrosis, and to determine the therapeutic gain of novel irradiation escalation protocols and techniques.

F. Acknowledgements

We would like to thank the NIH, ARRA 5 R01 EB007705-02, and Washington University for providing funding for this exciting development.

G. References

- Clarkson, R., Lindsay, P. E., Ansell, S., Wilson, G., Jelveh, S., Hill, R. P., & Jaffray, D. A. (2011). Characterization of image quality and image-guidance performance of a preclinical microirradiator. *Med Phys*, *38*(2), 845-856.
- CNMC. (2012). K602 Precision Electrometer, from <http://www.cnmcco.com/>
- El-Diery, W. S., Sigman, C. C., & Kelloff, G. J. (2006). Imaging and oncologic drug development. *Journal of Clinical Oncology*, *24*(20), 3261-3273.
- Fujita, H., Tsai, D.-Y., Itoh, T., Doi, K., Morishita, J., Ueda, K., & Ohtsuka, A. (1992). A Simple Method for Determining the Modulation Transfer Function in Digital Radiography. *IEEE Trans. on Medical Imaging*, *11*.
- Gleason, S. S., Austin, D. W., Beach, R. S., Nutt, R., Paulus, M. J., & Yan, S. (2006). *A New Highly Versatile Multimodality Small Animal Imaging Platform*. Paper presented at the IEEE Nuclear Science Symposium, San Diego, CA.
- Herman, M. G., Balter, J. M., Jaffray, D. A., McGee, K. P., Munro, P., Shalev, S., . . . Wong, J. W. (2001). Clinical use of electronic portal imaging: Report of AAPM radiation therapy committee task group 58. *Med Phys*, *28*(5), 25.
- Izaguirre, E. W., Birch, J., Su, I.-T., Price, S. G., & Low, D. (2012). Design of a preclinical image guided microirradiator: The microIGRT *Submitted to Phys Med Bio*.
- Izaguirre, E. W., Kassebaum, B. L., Birch, J., Su, I.-T., Goddu, S. M., & Low, D. A. (2009). *Development of a High Resolution Image Guided Microirradiator (microIGRT)*. Paper presented at the Nuclear Science Symposium Conference Record (NSS/MIC), Orlando, FL.

- Izaguirre, E. W., Sun, M., Carver, J., & Hasegawa, B. H. (2005). Dual modality micro-SPECT and micro-CT for small animal imaging: challenges and technical advances. *Proc. SPIE Int. Soc. Opt. Eng.* 5923.
- Jan, M.-L., Ni, Y.-C., Chen, K.-W., Liang, H.-C., Chuang, K.-S., & Fu, Y.-K. (2006). A combined micro-PET/CT scanner for small animal imaging. *Nuclear Instruments and Methods in Physics Research*, 314-318.
- Kiehl, E. L., Stojadinovic, S., Malinowski, K. T., Limbrick, D., Jost, S. C., Garbow, J. R., . . . Hope, A. J. (2008). Feasibility of small animal cranial irradiation with the microRT system. *Med Phys*, 35(10), 4735-4743.
- Klein, E. E., Hanley, J., Bayouth, J., Yin, F.-F., Simon, W., Dresser, S., . . . Holmes, T. (2009). Task Group 142 report: Quality assurance of medical accelerators. *Med Phys*, 36(9), 4197-4212.
- Kutcher, G. J., Coia, L., Gillin, M., Hanson, W. F., Leibel, S., Morton, R. J., . . . Wingfield, L. (1994). Comprehensive QA for Radiation Oncology: Report of AAPM Radiation Therapy Committee Task Group 40. *Med Phys*, 21(4), 581-618.
- Lee, S. C., Kim, H. K., Chun, I. K., Cho, M. H., Lee, S. Y., & Cho, M. H. (2003). A flat-panel detector based micro-CT system: performance evaluation for small-animal imaging. *Phys Med Biol*, 48(24), 4173-4185.
- Ma, C. M., Coffey, C. W., DeWerd, L. A., Liu, C., Nath, R., Seltzer, S. M., & Seuntjens, J. P. (2001). AAPM protocol for 40-300 kV x-ray beam dosimetry in radiotherapy and radiobiology. *Med Phys*, 28(6), 868-893.
- Mayneord, W. V., & Lamerton, L. F. (1941). A survey of the depth dose data. *The British Journal of Radiology*, 14, 255-264.
- McMaster-Carr. (2012)
- MITech. (2012). MI Tech Metals Inc.
- Paulus, M. J., Gleason, S. S., Kennel, S. J., Hunsicker, P. R., & Johnson, D. K. (2000). High resolution X-ray computed tomography: an emerging tool for small animal cancer research. *Neoplasia*, 2(1-2), 62-70.
- Pomper, M. G., & Lee, J. S. (2005). Small animal imaging in drug development. *Current Pharmaceutical Design*, 11, 3247-3272.
- Price, S. G., Silviu, A. A., & Izaguirre, E. W. (2012). A micro electronic portal imaging device for image guided conformal microirradiation of murine cancer models. *Submitted to the Journal of X-ray science and technology*.
- Scanditronix, & Wellhoffer. (2012). CC04 Technical Data, from http://www.rpdinc.com/html/scandatronix_wellhoffer_compac.html
- Thomson. (2012). Thomson Industries, Inc
- Umlaut. (2012). The Visible Mouse Atlas, 2012, from <http://www.umlautsoftware.com/?news&topic=visiblemouseatlas>
- Yuan, L., Holmes, T. C., Watts, R. E., Khosla, C., Broekelmann, T. J., Mecham, R., . . . Rich, K. M. (2010). Novel chemo-sensitizing agent, ERW1227B, impairs cellular motility and enhances cell death in glioblastomas. *J Neurooncol*.

2. A MICRO ELECTRONIC PORTAL IMAGING DEVICE FOR IMAGE GUIDED CONFORMAL MICROIRRADIATION OF MURINE CANCER MODELS

A. Introduction

In contemporary radiation oncology, treatments are delivered using clinical linear accelerators (linacs) capable of delivering highly conformal doses to a tumor or target organ while sparing the surrounding healthy tissue. The delivery of a highly conformal ionizing radiation beam to a target volume is achieved through the use of beam modulation devices such as orthogonal collimation jaws and multileaf collimators (Bortfeld, Kahler, Waldron, & Boyer, 1993; Chui, Chan, Yorke, Spirou, & Ling, 2001; Convery & Rosenbloom, 1991). The verification of beam positioning with respect to subject anatomy is performed using an imaging device, referred to as an electronic portal imaging device (EPID), which captures the patient loco-regional anatomy and the beam profile in transmission mode and aids the therapist in performing on line co-registration of patient anatomy with the treatment beam (Herman et al., 2001; Michael Partridge, Evans, Mosleh-Shirazi, & Convery, 1998; Mike Partridge, Symonds-Taylor, & Evans, 2000). The end point benefit of image guidance is appropriate patient positioning and treatment beam verification to improve treatment accuracy and outcome.

Currently, clinical radiation therapy treats more than 50% of cancer patients, and despite the high volume of patients radiation oncology has had for several decades, only in the last few years has there been development of high resolution instrumentation to perform radiobiological research to test irradiation techniques and improve clinical outcomes (Cho et al.; Motomura, Bazalova, Zhou, Keall, & Graves; Yuan et al.). These microirradiator show considerable advances in orthovoltage conformal microirradiation in radiobiological models that mimic treatment conditions and techniques currently implemented in clinical protocols scaled from human to small animal dimensions (Kiehl et al., 2008; Medina et al., 2008; Pidikiti et al., 2011). These developments aim to establish instruments used as a test bench for new radiotherapy and adjuvant chemo-radiotherapy treatment techniques tested on murine models of cancer and tissue response using highly conformal volumetric doses delivered to a small planned target volume (PTV), e.g., a tumor or organ, with submillimeter precision. This is a significant engineering challenge which requires the integration of high resolution anatomical imaging devices and a precise orthovoltage x-ray beam delivery

system. Because portal imaging is the imaging treatment verification standard in clinical practice, preclinical microirradiator development followed this paradigm. In particular, our group implemented a small animal image guided microirradiator with an architecture and working principle based on clinical image guided radiotherapy that we termed: the microIGRT (Izaguirre et al., 2009).

In preclinical research, high resolution portal imaging provides a method for performing quality assurance of beam to PTV conformality, beam aiming, animal subject positioning, beam fluence verification during animal set up prior to the delivery of the treatment, and verification of the treatment beam prior to and at any required time point during the course of a fractionated radiobiological experiment. High beam conformality indicates the efficiency of delivering a prescribed dose to a malignancy while avoiding healthy tissue irradiation to enhance tumor control probability and reduce normal tissue complications. Beam positioning accuracy minimizes the risk of changes in the irradiated tissue, especially organs at risk, originated by interfraction subject positioning and intrafraction subject motion during treatment delivery. Beam fluence verification allows for accurate determination of the dose delivered to the animal subject in each treatment fraction and thus the entire treatment, consequently allowing for comparison and accurate statistical analysis of the experimental outcomes. Each of these parameters influence the outcome of a treatment and their accuracy is fundamentally important to obtain unbiased experimental conclusions which can be translated to the clinical setting, thereby providing clinical benefit in the future by improving cancer treatment outcome.

The translational nature of micro portal imaging devices indicates that a path for the specification of a μ EPID should be based on comparing the use of an EPID in clinical image guided external beam radiotherapy with the equivalent irradiation technique in a murine model applied to the same anatomical treatment site or malignancy location (Hill, Rodemann, Hendry, Roberts, & Anscher, 2001). To illustrate this point, we will focus our discussion on lung cancer external beam radiotherapy. The average human lung has an approximate cross sectional surface area of $25 \times 13 \text{ cm}^2$, and the average mouse lung has a cross sectional surface area of $10 \times 6.6 \text{ mm}^2$. This indicates the need for, on average, 25 times higher beam aiming precision and beam profile modulation resolution in small animal microirradiation without an increase in dose spill off to establish the same level of beam conformality, treatment repeatability, and surrounding healthy tissue and vital organ sparing.

Furthermore, in a murine lung cancer model, a typical tumor size is on the order of 1 to 2 mm, which can be as close as 1 mm to the 2 mm diameter spinal cord (Segars, Tsui, Frey, Johnson, & Berr, 2004). Therefore, a millimeter shift in beam positioning will produce healthy tissue complications or under-dosing in the tumor. In similar clinical protocols, the required resolution will be 5 to 10 mm for fractionated treatments. Here, we are not considering stereotactic radiosurgery, a technique which presently has no preclinical counterpart and is under development by our group. Considering the previously discussed precision and anatomical scales, an image quality requirement for microirradiation portal imaging devices is highly homogeneous distortion free imaging to provide a faithful representation of anatomical details, beam dimensions, and beam fluence with submillimeter accuracy (Clarkson et al.).

Images acquired during treatment should not contribute significantly to additional dose, to ensure no alteration of the animal model. For example, a typical lung treatment dose is 40 Gy to the PTV (20 fractions of 200 cGy at 1 Gy/min) (M. Partridge, Ramos, Sardaro, & Brada), therefore the total imaging dose throughout the treatment must be less than 40 cGy to avoid biasing the experiment outcome (Murphy et al., 2007). This means that during each positioning imaging (3-4 images per animal per fraction), the dose delivered to the animal subject should not exceed 40 cGy over the entire treatment (2 cGy per fraction) while still providing clear high resolution images for anatomical regional imaging and beam treatment verification. This example indicates a dose constraint in micro portal imaging with respect to the total dose delivered during the treatment, which will define requirements for the sensitivity of the μ EPID.

Loco regional anatomical imaging is required to determine beam positioning with respect to reference anatomical landmarks. Consequently, the field of view should be large enough to image the anatomy landscape for recognition of characteristic bone features, which in our example of the lung are the vertebrae, rib cage, sternum, clavicle joints, etc. For typical murine models, a practical field of view should be larger than the maximum animal diameter, which is approximately 6 cm (rat body diameter). Additionally, the portal imaging system should be capable of generating an on line distortion free overlay of the microirradiation beam and the anatomical regional image for fast visualization of co-registered beam boundaries with target volumes and local anatomical landmarks (Cho et al.).

Current small animal microirradiator treatment beams operate at 120 kVp (Graves et al., 2007), 225 kVp (Clarkson et al.; Wong et al., 2008), and 320 kVp (Izaguirre et al., 2009). Additionally, a low energy wide

beam, from 60 kVp to 120 kVp, is used for anatomical imaging (Schambach, Bag, Schilling, Groden, & Brockmann). Consequently, a small animal microirradiator portal imaging device must be capable of generating high quality anatomical and beam images in this wide range of energies. At the orthovoltage energies, the radiation exposure will damage the imaging sensors; therefore it is important to choose the appropriate imaging device. Some low energy portal imagers utilize amorphous silicon detectors designed for clinical mammography (Winkler, Hefner, & Georg, 2005). The electronics of these detectors are susceptible to radiation damage at energies higher than 120 kVp (Lee et al., 2003). A folded beam optical path is a solution to position the imaging sensor away from the radiation beam path and to avoid mechanical movable components that could compromise the beam to anatomy registration precision. This solution was implemented in the μ EPID described in this article.

Accompanying the instrument hardware, software should be implemented to optimize image settings such as integration time, gain, gamma correction, and selection of region of interest to perform high quality and rapid image acquisition to increase imaging throughput and to switch between the two ranges of imaging; the anatomical imaging and the beam fluence distribution imaging. Additionally, a microirradiation session may need multiple portal images. A standard experiment with 12 animals will require 3-4 portal images per animal, so it is necessary to have proper software for quick and convenient acquisition and fusion of portal images.

In this article, we present the development and application of a preclinical μ EPID specifically developed for small animal microirradiation of murine models of cancer and radiobiological research which satisfies the requirements based on translational radiotherapy previously described in this section. To our knowledge, there is no commercially available radiation hard imaging device designed for the energy range with the imaging parameters required for small animal imaging and treatment delivery verification as described above. We show in this article that the developed μ EPID is capable of handling high levels of ionizing radiation without damage to the electronics during irradiation procedures, operating in a wide range of energies (60 kVp to 320 kVp), and acquiring low dose, high resolution anatomical images. Reduced cost is also an advantage of our imaging system, but it is not the driving motivation for this work. To validate this technical development, we demonstrate the use of the μ EPID to provide *in vivo* verification of radiation treatment, including proper animal and beam positioning, and dosimetric image calibration for

accurate dose rate delivery and verification in phantoms and *in vivo* pilot studies of healthy lung tissue complications, treatment of gliomas with adjuvant chemo-radiotherapy therapies, and radiotherapy of breast cancer xenograft tumor models.

B. Methods

i. General construction details

An image of the developed μ EPID installed in a microirradiator beam stopper and a 3D rendering showing the main components which constitute the device are shown in figure 16. The μ EPID consists of four main body parts: the CCD sensor and image acquisition electronics, a radiation shield for radiation sensitive electronics, a high resolution wide acceptance angle folded optical system, and a high resolution scintillator screen embedded in a supporting and encapsulating frame. All of the elements are assembled on a reel to allow for easy device installation and micro alignment on another mechanical fixture, such as the gantry of a small animal microirradiator.

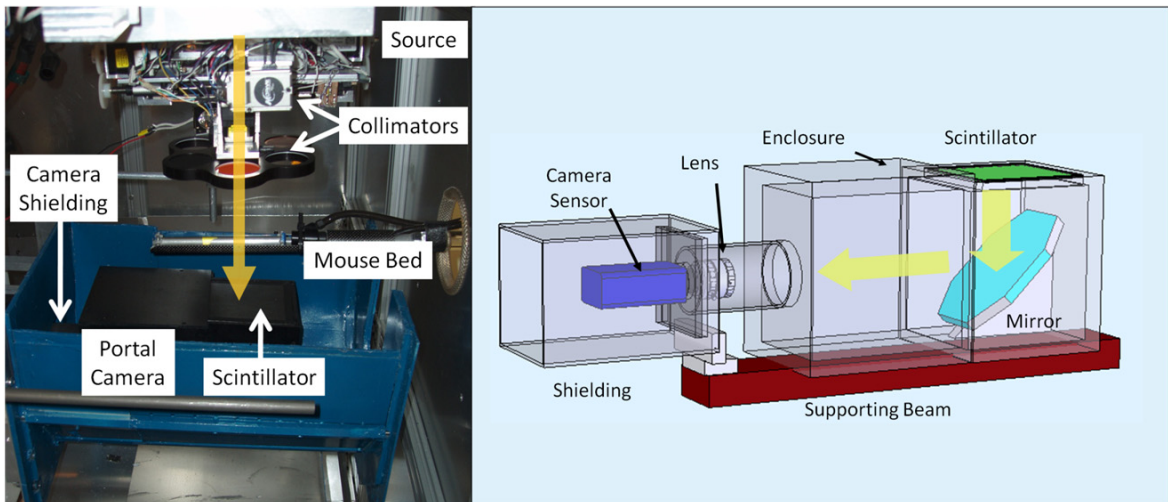


Figure 16. Left: Image of the developed portal μ EPID installed on a small animal microirradiator beam stopper. Right: 3D rendering of the developed portal μ EPID showing the main mechanical and imaging components. The arrow indicates the path of the light emitted by the scintillator.

To avoid radiation damage, the optical system is folded to place the CCD camera electronics away from the direct path of the orthovoltage beam. The camera signal processing electronics and CCD sensor have been encased in a shielding enclosure to prevent the scattered ionizing radiation from reaching the camera's sensitive electronics. The shielding consists of steel and lead, with the steel providing shielding

and support, and the lead providing high stopping power against the penetrating orthovoltage beam. The total attenuation of the enclosure is 6.6 HVL at 189 keV, which is the typical average energy of a 320 kVp filtered orthovoltage small animal microirradiator (NIST, Hubbell, & Seltzer).

The optics of the μ EPID, a high resolution lens and an optical path folding mirror, are placed inside a polyethylene enclosure. All of the materials are blackened to minimize straight light and are made with polyethylene to minimize x-ray scattering and generation of secondary x-rays which can generate a fuzzy or phantom emission in the scintillating screen. The scintillator is supported by an acrylic frame attached to the μ EPID polyethylene body. On the beam side of the μ EPID is a thin 750 μ m black garolite screen, which protects the scintillator screen and prevents exterior light from interfering with the scintillator emission. The x-ray attenuation of this material is 5% for 120 kVp, which is typically the minimum energy orthovoltage x-ray sources emit. At treatment energies, such as 300 kVp, the attenuation is less than 1%.

ii. Imaging requirements and implementation

The imaging optics components specifications are defined by the field of view, imaging resolution, lens light collection efficiency, scintillator spectral emission, and CCD sensor spectral sensitivity. There is a trade-off between field of view and resolution because a larger field of view, as determined by the lens magnification, will have lower sampling for the same detector pixel array size and density. In this application, the field of view is defined at the object plane, which is at the mid-plane of the animal subject under microirradiation, and it should be at least larger than the torso diameter of the rodents to be imaged. With this consideration in mind, the required field of view is estimated to be 25x25 mm² for mice, and estimated to be 60x60 mm² for rats (Hans, 2004). Imaging animal anatomical structures for treatment beam aiming and microirradiation verification requires that a portal imaging device should have a resolution of 500 μ m or better, an observation based on the average distance between organs in digital models of mice based on high resolution MRI images (Software, 2012).

The μ EPID resolution and field of view at the object plane are obtained by back projecting the CCD pixel array to the scintillator plane using the optical ray path and then back projecting the CCD array image from the scintillator plane to the object plane using the x-ray path. Therefore, resolution varies according to the position of the object and the irradiation source. In our irradiator geometry, the scintillator is located 9

cm beneath the central plane of the mouse bed and the source position can range from 30 cm to 38 cm from the mouse bed. This range of distances will provide a low resolution of 200 μm and a maximum resolution of 150 μm at the animal plane for the selected CCD detector array with a pixel size of 4.65 μm and a multi element lens with a magnification of 0.043. Higher resolution can be achieved by reducing the x-ray source to animal distance, but this is not a feasible approach in small animal microirradiators because the distance between the source and the mouse must be kept higher than 20 cm to avoid the fast $1/r^2$ decay of the beam intensity across the animal body (Mayneord & Lamerton, 1941). Due to the $1/r^2$ effect, the ratio of entrance dose to exit dose at a source to axis distance (SAD) of 38 cm for a mouse (25 mm diameter) is 87.5%. For a rat (60 mm diameter), the entrance to exit dose ratio is 72.9%. This indicates a percentage depth dose (PDD) from 12 to 27% between when the beam enters and exits the rodent body, compared to a PDD of approximately 45% if the SAD were decreased to 20 cm. The 27% PDD is comparable with the clinical values in a human body and consequently shorter source to animal body distance is avoided in small animal irradiators.

To focus the scintillator plane onto the CCD sensor plane with high definition, we used a camera lens with a nominal focal length of 12 mm and an ultrafine micrometric adjustable focal distance. This system has better alignment capabilities than previous systems reported in the literature, which were constructed using sliding rods to adjust the scintillator camera sensor distance to perform a fine focus of the scintillator emission onto the CCD detector (Tate, Chamberlain, & Gruner, 2005). The folded optical system was constructed by placing a $1/10 \lambda$ front surface mirror oriented at 45° , located beneath the scintillator as shown in figure 16. As mentioned above, this design prevents direct exposure of the electronics to the ionizing radiation through the camera lens by orienting the camera axis orthogonal to the irradiation beam path.

Due to the availability of large continuous screens, gadolinium oxysulfide ($\text{Gd}_2\text{O}_2\text{S}$) scintillators are optimal for cameras designed with lenses which couple a single detector element to a large scintillator because the images are free of junction lines, which is a typical defect of detectors based on crystal scintillators bonded to build a larger sensing surface (Kyriakou, Prell, & Kalender, 2009). The μEPID scintillator has a surface area of $10.2 \times 10.2 \text{ cm}^2$, a high speed grade, or sensitivity, of 600 nm with a spectral emission in the green portion of the optical spectrum (540 nm) (Gorokhova, Demidenko, Mikhrin, Rodnyi,

& Eijk, 2004). This corresponds to the highest sensitivity of the CCD camera (500 nm +/- 100 nm) sensor when the long wavelengths are filtered by the lens elements and the sensor front window. The high scintillator speed reduces the imaging integration time and consequently reduces the dose absorbed by the animal subject during imaging. The selected multi element lens has a speed of f/1.4 and a broad anti-reflecting coating for light with wavelengths from 400 to 600 nm to maximize the acquisition of the light emitted by the scintillator. As a whole, the selection of these elements assures a maximum optical coupling between the scintillator emission and the CCD camera sensor to minimize the imaging dose delivered to the animal as discussed in the introductory paragraph.

iii. Instrument interface

The μ EPID interface is through an IEEE 1394b port which allows image data transfer with a speed of 780 Mb/s to a personal computer. The μ EPID software was written using ANSI C++ and allows for the control of the gain, contrast, and brightness of the image acquisition and the integration time. The μ EPID can acquire images with a rate of 17 frames per second with 12 bit depth and the integration time can be selected from 1 msec to 165 sec in steps of 1 msec. Imaging overlay of the anatomical image, with a large field, and the beam image, with a reduced targeted field, can be performed during the image acquisition for pre-irradiation beam anatomy co-registration or later for post processing and evaluation of experimental results. Acquired images are displayed in a window screen with a delay of 100 msec and can then be saved in a storage device for future analysis. For high speed data acquisition and to reduce the volume of the imaging data when the region of interest is smaller than the whole image, the unused pixels are not transferred from the imaging device to the computer frame grabber. Standard procedures of image gain flattening and bias reduction used to process the image can be found in the literature (Bushberg, J. Anthony Seibert, Jr., & Boone, 2001; Russ, 2007). In short, the air image (beam only) and the dark image are divided out of the raw image to reduce noise, μ EPID sensitivity heterogeneities, and x-ray beam intensity non-uniformities.

iv. *Image adjustments and calibration*

Testing and calibration of the portal imager were performed using phantoms specifically designed for scrutinizing the μ EPID performance in image guided microirradiation applications. The testing phantoms can be subdivided into optical alignment and scintillator imaging calibration. For optical alignment calibration, we used high resolution printed grid patterns of bars, reticules, and calibrated targets. These phantoms were used as an aid to determine the μ EPID's optical elements alignment, optical resolution, barrel or pincushion distortion, etc. These tests were performed according to the usual procedures described by Rastogi and Malacara (Malacara, 2007; Rastogi, 1997). Here, we will only describe additional procedures used in this development. The CCD camera, lens, and folding mirror were aligned to achieve uniform imaging of a patterned phantom located at the scintillator screen plane. The fine adjustment of the focal length was used to fine tune the sharpest image of the reticular pattern placed at the scintillator plane. Experimentally, it was found that the point of maximum resolution is when the lens is adjusted to image a test pattern located 0.25 mm deep with respect to the scintillator screen surface, which compensates for the light spread inside the 0.5 mm thick scintillator screen. Imaging testing for pincushion and barrel distortion showed that the optical system has less than 500 μ m barrel distortions across the field of view. These distortions were corrected through software to achieve no more than 1/2 pixel of barrel distortion (San, Hwang, Funk, & Izaguirre, 2004) with an obliquity response fall off of no more than 1% with respect to the central axis intensity.

v. *Testing of imaging quality and resolution with phantoms*

After completion of the optical system alignment, the optical elements were locked and the portal imager was placed into position along the irradiation beam at the appropriate distance from the mouse bed and the irradiator source as discussed in section 2.2. Beam imaging and anatomical imaging testing were performed using acrylic phantoms designed to determine resolution and contrast in conditions which mimic animal irradiation and *in vivo* portal imaging. To determine the modulation transfer function (MTF) of the imaging system, we used a tilted wire technique to increase the sampling frequency above the camera resolution as described by Fujita, et al. (Fujita et al., 1992). Tests were performed using a beam generated with the x-ray tube operating from 60 kVp to 320 kVp. Beam quality was modified using Thoreau's filters

to obtain average equivalent energies from 0.5 mm of Cu to 5 mm of Cu, to ensure the use of the portal imager at all energies and beam qualities of recently developed microirradiator (Izaguirre et al., 2009; Pidikiti et al., 2011; Wong et al., 2008).

Imaging contrast was assessed in relation to the dose delivered to the small animal during irradiation considering that minimization of the dose will reduce the contrast and decrease the signal to noise ratio. Dose measurements were performed using a Scanditronix Wellhofer compact air ionization chamber CC04 ("CC04 Technical Data," 2012) and a CNMC K602 nanocoulomb resolution electrometer ("K602 Precision Electrometer," 2012). The ionization chamber was secured in a build up phantom with the diameter of a typical mouse torso diameter to determine the dose at the central point of an animal body. Measurements of the image contrast for typical organ thicknesses versus dose were performed using a wedge phantom developed to mimic varying tissue thicknesses throughout a small animal body to produce graphs to guide the selection of contrast, source operating kVp, current, integration time, and dose during an image guided microirradiation session.

In order to determine the detective quantum efficiency (DQE) of the developed μ EPID, we followed the methods described in the references (Bath, Sund, & Mansson, 2002; Boyer et al., 1992; Dobbins et al., 1995). This method requires the determination of the beam fluence, MTF, noise power spectrum, and scintillator emission efficiency for the operating energy range, the lens light collection efficiency, and the CCD sensor spectral sensitivity. The beam fluence was determined using ion chambers and silicon diodes, and the average of both methods was used to establish the weighted average fluence. The noise power spectrum was measured using multiple averages of air images as recommended by Dobbins (Dobbins et al., 1995), lens efficiency was computed using the method described by Liu (Liu, Karellas, Harris, & D'Orsi, 1994), the scintillator emission efficiency for the range of energies was determined using data from the NIST database (NIST et al.), and CCD spectral sensitivity was acquired from the manufacturer ("Basler scA 1390-17fm Camera Specification," 2007).

vi. Dosimetric calibration

Orthovoltage treatment beams were delivered to determine the sensitivity and accuracy of this portal imaging device to be used as a transmission dosimeter to measure beam dose rate. Using a 1 inch acrylic

rod to simulate the attenuation of a beam through rodent tissue, the transmitted intensity at the central plane was determined for the two most common treatment beam tube accelerating potentials, 225 kVp and 300 kVp, filtered to achieve 2.9 mm of Cu and 3.9 mm of Cu, respectively for the operational range of tube currents, from 0.5 mA to 7 mA. Imaging variables such as gain, gamma, and integration time were kept constant to facilitate the formulation of an image intensity to dose rate calibration. Dose rates were measured with the CC04 ion chamber inserted in a build up phantom with the same dimensions as the imaged phantom.

C. Results

i. μ EPID imaging characterization

The μ EPID resolution was determined using the MTF acquired from a line spread function (LSF) using the technique mentioned previously. In figure 17, we present the LSF measurements, a Lorentzian fitting of the LSF, and the resulting MTF. The MTF obtained from the Fourier transform of the LSF indicates that a spatial resolution of 3.92 line pairs/mm at 50% contrast is achieved. The error in the MTF was estimated to be approximately 10% of this value and is originated by image blurring at the edges of the wire image. A resolution test using a multi-wire phantom array shows that a rectangular test pattern with 200 μ m spacing can be resolved at any point in the camera field of view. Considering these results, we conclude that the nominal resolution for the system is 200 μ m across the field of view.

The image contrast as a function of the beam energy and fluence was measured using step wedge phantoms, setting the orthovoltage x-ray source to practical operating kVp and current parameters for anatomical imaging and orthovoltage treatment. The step wedge phantom is tissue equivalent and mimics increasing thicknesses of soft tissue. Other imaging parameters, such as gain and brightness, were kept at constant values, selected where the highest overall contrast and image quality was achieved for the naked eye observer. The results of these measurements for imaging tube operating voltages of 60, 80, and 120 kVp and currents from 0.5 to 1 mA versus phantom depth from 2.5 to 30 mm are shown in figures 18 and 19. The first set of curves show contrast of different tissue thicknesses relative to air, to determine the visibility of tissue according to its thickness along the beam path. The second set of curves, presented in figure 19, shows that tissue contrast diminishes as a function of the location of the imaged tissue thickness

with respect to depth location in the body. The maximum contrast reduction is at the highest depth, and is more pronounced for beams of lower energy, which indicates that this effect is a result of beam hardening.

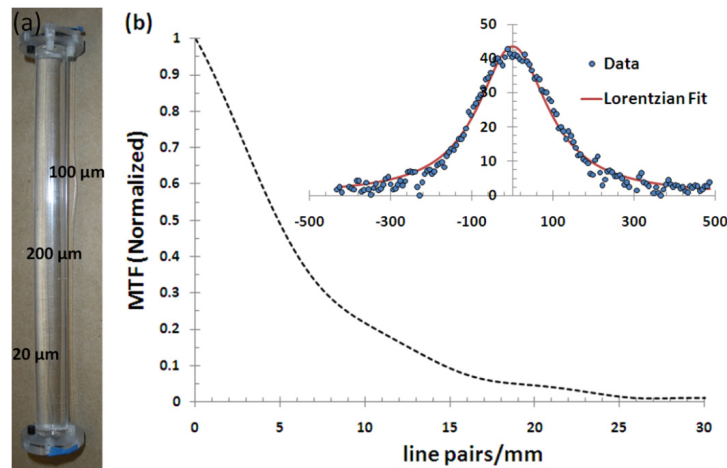


Figure 17. (a) Multi-wire phantom constructed with tungsten wires of different thicknesses to determine imaging resolution in a small animal equivalent volume. (b) MTF graph obtained from the LSF data shown in the inset. LSF was fitted using a Lorentzian function.

Evaluation of the contrast between soft tissue and bone was performed using animal carcasses imaged at different anatomical locations to obtain averaged measurements. Contrasts between tissue and bone are shown in figure 20 as a function of the dose delivered to the animal with the μ EPID integration time adjusted to keep a constant contrast for the same range of x-ray source operating potentials and currents. The curves were obtained for contrast values of 400 and 500, because after an exhaustive scan of the μ EPID operational parameters, we determined that these are the optimal contrast values where the anatomical images have the best quality and definition to multiple observers. It's important to note that similar curves were observed for other contrast values and are not included in this article for clarity. These graphs show the lowest dose in this system is achieved when imaging is performed with 120 kVp for the same contrast and is therefore the most commonly used x-ray tube operational parameter for murine portal imaging.

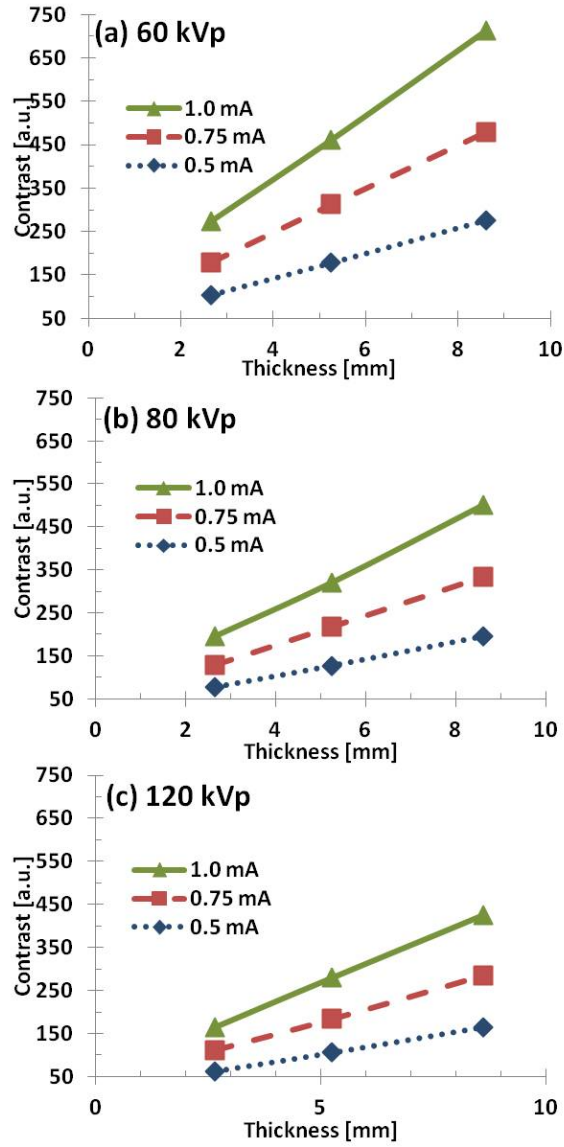


Figure 18. Tissue contrast in relative pixel intensity values with respect to air as a function of the phantom thickness and the imaging beam operating potential and current. Operating potential is reported in the figure for the practical values of x-ray energies

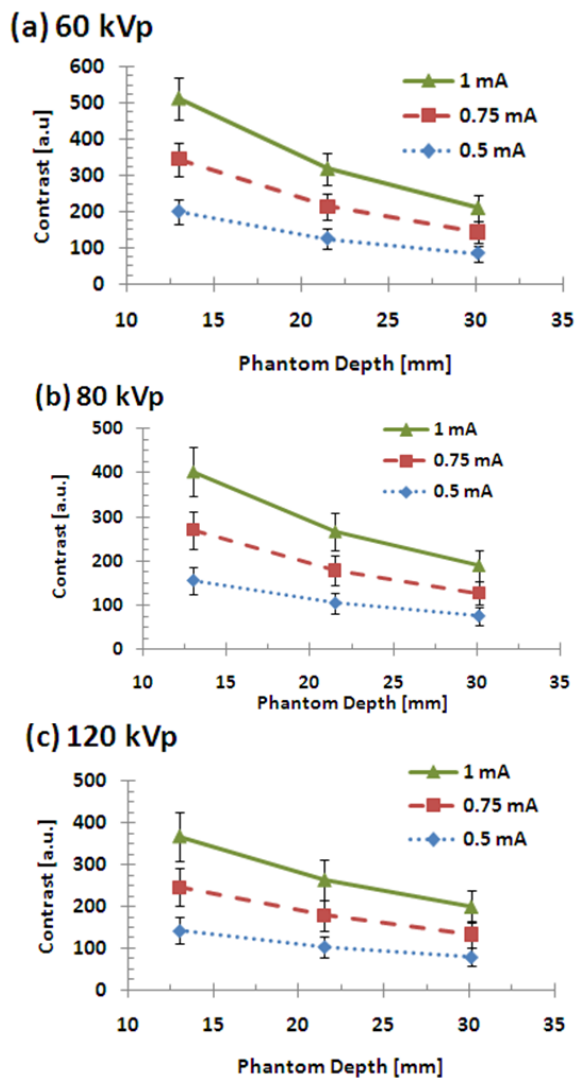


Figure 19. Contrast gradient as a function of phantom depth for the useful range of microirradiation source practical imaging potential and currents, which include 60 kVp, 80 kVp, and 120 kVp with current values of 0.5 mA, 0.75 mA, and 1 mA.

The μ EPID detective quantum efficiency was measured for both ranges of operation, the anatomical imaging (120 kVp) and the orthovoltage treatment beam fluence imaging. Results of the DQE for the 120 kVp, 225 kVp, and 300 kVp are shown in figure 21. At all energies, the DQE drops as a function of the spatial frequency and its “frequency zero” value is higher at the imaging energies. These graphs show that a considerably lower DQE is achieved with treatment beam imaging, however in microirradiation applications, the treatment beam can be delivered for longer times and consequently, the DQE deficiency is compensated for by the integration time.

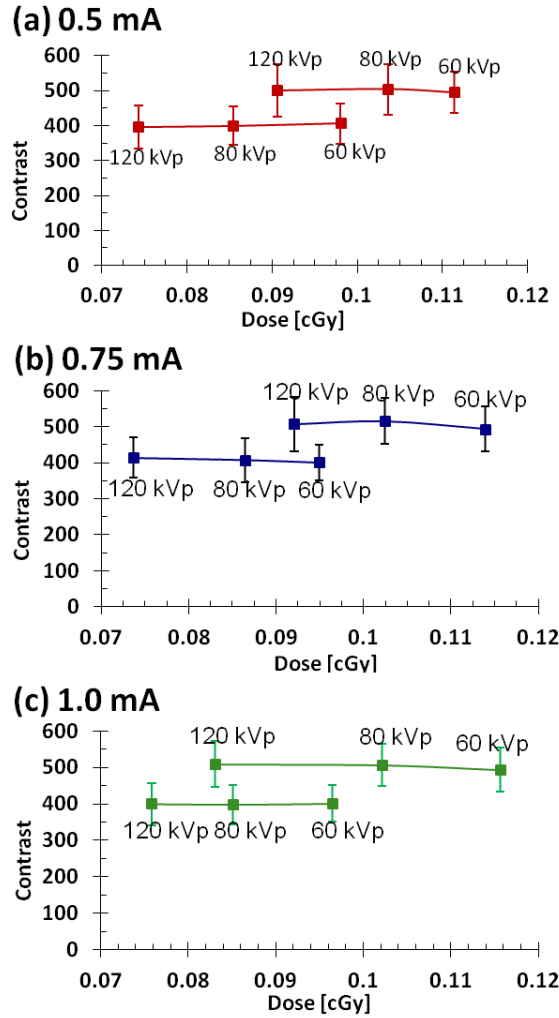


Figure 20. Constant contrast curves for contrast values of 500 and 400 as a function of small animal absorbed dose for microirradiation source practical imaging potential and currents.

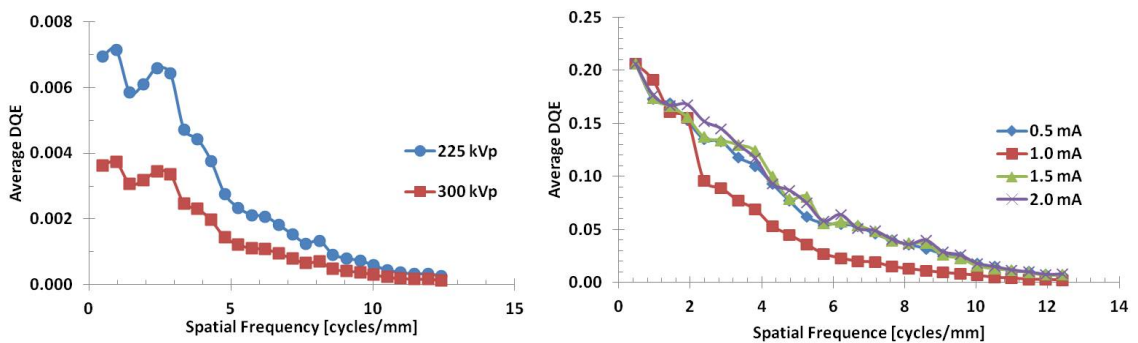


Figure 21. Left: DQE for filtered treatment orthovoltage beams of 225 kVp and 300 kVp, with 2.9 mm of Cu and 3.9 mm of Cu, respectively. Right: DQE for anatomical imaging beam of 120 kVp, filtered with 2.8 mm of Al and operating currents of 0.5, 1, 1.5, and 2 mA.

ii. Coregistration resolution

Experiments of multiple animal positioning for irradiation were performed to determine the maximum spatial sensitivity to detect shifts in the co-registration between anatomical beam images. The co-registered images show that the images are adequate to perform beam positioning using the beam boundary or beam isocenter with respect to the animal anatomy landmarks used as a reference with a precision of 250 μm . Repeatability experiments of beam to anatomy correlation were performed to establish the robustness of the μEPID to determine the error in multiple sequential beam positioning and cross section measurements as required in fractionated treatments.

Images were analyzed to determine the minimum detectable beam cross section variations in a beam size of $10 \times 10 \text{ mm}^2$, which is our standard microirradiator calibration and reference beam. A similar concept is used in the calibration and quality assurance of clinical linacs where the reference beam has a cross section of $10 \times 10 \text{ cm}^2$ (Almond et al., 1999). This test shows that the portal imager can detect 200 μm variations in the beam cross section and the beam centroid can be determined with a precision of 100 μm .

iii. Determination of dosimetric calibration and sensitivity

We tested the μEPID to perform dosimetry of the orthovoltage microirradiation beams, and we validated the calibration accuracy and precision in performing portal beam dosimetry. The calibration was performed for the 225 kVp and 300 kVp beams, and the current was used as a parameter to control the dose rate. Dosimetric calibration curves are presented in figure 22. These tests show that the μEPID can determine a variation in dose rate with a relative sensitivity of 0.25 cGy/min for a 300 kVp orthovoltage beam, with a quality of 3.9 mm of Cu, and a relative sensitivity of 0.16 cGy/min for a 225 kVp beam, with a quality of 2.9 mm of Cu.

The accuracy of the calibration was determined by comparing the average pixel intensity values of a flood image with the dose measured with ion chambers in a mouse cylindrical phantom for exposures of 1 min, with a beam delivering an average dose rate of 50 cGy/min. This calibration was found to have 2.5% accuracy with respect to ion chambers. The precision of the μEPID as a dosimeter was validated using these curves in a test with a delivered beam dose rate of 40 cGy/min and the measured dose, using the calibration curves, was compared against a CC04 ion chamber used as a gold standard. Dose rate

determination based on portal image pixel intensity and the calibration curve of figure 22 shows a maximum error of 4.1% with respect to the ion chamber. This test validates the use of the μ EPID as an imaging dosimeter for small animal micro conformal irradiation.

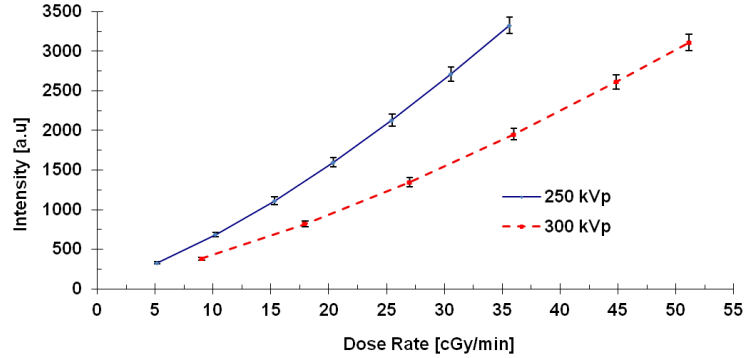


Figure 22. Intensity vs. dose rate for two treatment energies. 250 kVp (solid line) for 1–7 mA and 300 kVp (dashed line) for 1–5.7 mA.

D. In vivo portal imaging evaluation

We evaluated the developed portal imaging device for imaging and treatment quality assurance of animal models of lung tissue response to ionizing radiation, gliomas, and breast cancer xenograft tumors. For these tests, the rodents were anesthetized with isoflurane and placed in the animal bed, which was subsequently positioned in the field of view of the μ EPID.

i. Evaluation with model of normal lung tissue response to irradiation

This experiment was designed to show the capability of the μ EPID to image and guide conformal microirradiation in an animal model of normal lung tissue complications originated during treatment of a lung cancer tumor. For this evaluation, the portal imaging system must use a large field of view which encompasses the entire thoracic cavity of the animal. The irradiation beam is limited to the cross section of both lungs with a margin to compensate for lung motion. The esophagus and spinal cord are protected from the irradiation beam by attenuating the beam using a lead mask with a nominal thickness of 8.5 HVL, creating a split irradiation field, as shown in figure 23a. The location of the beam must be determined with a precision of 500 μ m or better in the transverse direction to avoid esophagus irradiation while conformally irradiating the lungs. To assess the accuracy of the microirradiation positioning based on portal images, a

low dose image of the anatomy is taken at 120 kVp, with a beam quality of 2.8 mm of Al, to image the lung, vertebral column, and lung chest wall with high definition. After the animal is positioned according to the treatment plan, an image of the irradiation beam at 300 kVp is acquired for a short fraction of time. In this set up, visual analysis of the images shows that the animal anatomy and the beam can be co-registered with a resolution of 700 μm in the animal longitudinal direction and 400 μm in the animal transaxial direction. This resolution accounts for the uncertainty originated in the animal positioning by respiratory motion, which contributes with a larger motion in the longitudinal axis of the image (head to tail direction). This analysis shows that the requirements for performing lung microirradiation are satisfied using the developed μEPID imaging capabilities.

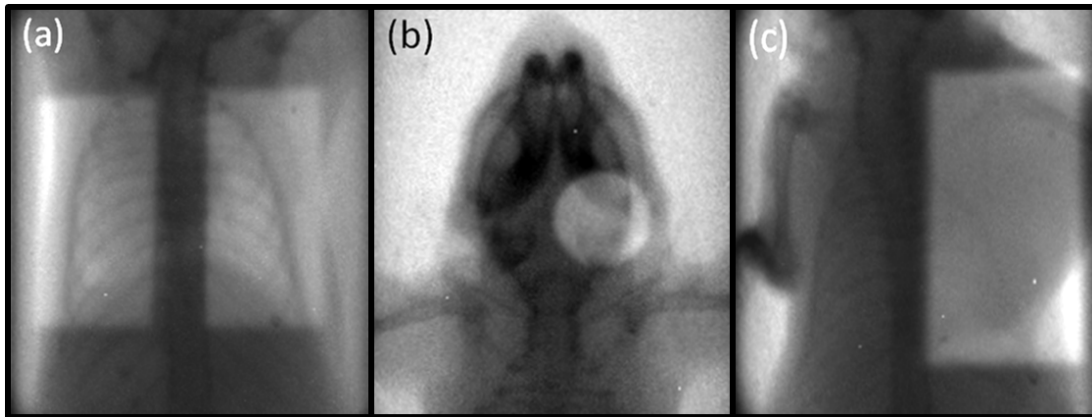


Figure 23. Anatomical portal images coregistered with orthovoltage treatment beams. (a) Portal image of a mouse thoracic cavity overlay with a split beam to irradiate both lungs. (b) Portal image of a mouse head showing the bony anatomy with the circular treatment beam placed at the right hemisphere. (c) Portal image of a mouse torso with a xenograft tumor in the mammary fat pad and an overlay of the treatment field.

ii. Evaluation with a model of glioblastoma brain tumor treatment

In this test, we used animal models with gliomas implanted in the right hemisphere of the brain. In this application, the small 2 to 5 mm diameter tumors were irradiated with 6 mm diameter circular beams to investigate the potential enhancement of tumor response when ionizing radiation therapy is combined with radiosensitizers.

The cranial image of the animal was analyzed to determine the anatomical landmarks of the animal head. In this experiment, it is important to determine the upper rim of the eye sockets, the mid cranial lines and the posterior joint of the cranio-spinal cord to define the position of the brain hemisphere. A portal image of the

animal head is in figure 23b with a co-registered image of the irradiation beam directed to the tumor. The treatment beam covers the upper half of the cranial region where the tumor is located. In these experiments, precise beam localization is required to avoid high function and vital organs. For this purpose, higher resolution images are taken to visualize details in bony structures and to localize the irradiation beam with higher precision. The absence of body motion and simple localization of the animal head anatomical structures facilitates beam positioning with an accuracy of 300 μm , which satisfies the estimated requirements to perform conformal microirradiation of the glioma implanted in the brain with high conformality.

iii. Evaluation with xenograft tumor models

In general, xenograft tumor irradiation requires good delineation and beam boundary control at the interface between tumor tissue and healthy tissue. For this purpose, a high resolution image of the animal body is taken to determine the extent of the tumor to define where the location of the field boundary should be placed to avoid excess dose to the animal body. A xenograft animal model of breast cancer bearing a tumor located at the mammary pad was imaged to determine the tumor boundary, and the field was then adjusted to match that boundary as shown in figure 23c. In this experiment, we performed a repeatability study to determine the precision that can be achieved using the μEPID to perform image guided radiotherapy in a fractionated irradiation experiments. The positioning error in a xenograft experiment that consists of 35 fractions was estimated to be within 400 μm along the complete treatment.

E. Discussion and conclusions

The use of high resolution portal imaging in radiobiological experiments with animal models provides a valuable tool for animal positioning, beam localization, and beam treatment verification (Izaguirre et al., 2009; Zhou et al.). Portal imaging provides a method to conduct accurate beam delivery to a target organ as well as a means to avoid unnecessary dose to normal tissues. Digital portal imaging devices offer a distinct advantage with respect to film imaging because of the nearly real time visualization of the animal anatomy and beam localization provided by portal imaging, an important requirement to assure translational results in preclinical microirradiation. Furthermore, a portal imaging device can provide dosimetric verification of

the treatment by calibrating the detector response with the dose rate delivered to the animal subject for each operating mode of the irradiation source. Dose rate determination during an experiment confirms proper beam source operating parameters, such as tube potential and tube current, as well as the use of appropriate filters to avoid experimental failure which will consequently minimize animal burden.

Dosimetric calibration curves were generated for the two typical energies used in preclinical microirradiation. We tested the predictive value of these curves by performing treatment delivery experiments where dose was measured using the μ EPID and ion chambers. The point measurements were within 4.1%, indicating that the μ EPID can be used as a daily dosimeter in fractionated irradiations. Furthermore, images of the beam profiles can be calibrated using the calibration curves reported in figure 22. A calibration of the beam profile used for glioma microirradiation is shown in figure 24. The calibration of this beam is within 5% of the dose measured by an ion chamber, and it provides additional dose distribution information that is difficult to obtain with ion chambers.

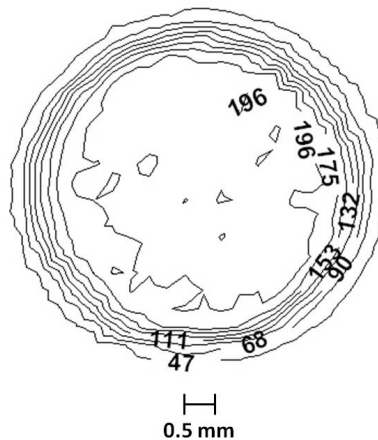


Figure 24. Determination of the dose profile delivered to the glioma implanted in the brain hemisphere as shown in figure 23b. The dose contours, labeled in cGy, are based on the dosimetric calibration of the μ EPID dose curve reported in figure 22 for the 300 kVp orthovoltage treatment beam.

Phantom tests show that the developed μ EPID can be distortion corrected to capture anatomical and beam profile images with 200 μ m resolution when performing small animal anatomical imaging at x-ray energies in the range of 60 kVp to 120 kVp and high fluence orthovoltage beam profiles measurements for 225 kVp and 300 kVp beams without exchanging scintillators or applying an attenuating screen with movable parts that can affect high resolution correlation between beam and animal model anatomy. Furthermore, the image overlay can be achieved immediately after portal image acquisition, allowing fast microirradiation

verification and animal positioning, which is a limiting factor for the animal throughput in preclinical irradiators that is overcome with the developed μ EPID technology. Additionally, the μ EPID has been validated in several experiments for extended exposures with no evidence of any noticeable deterioration in the electronics, sensor, or image quality from ionizing irradiation for more than one year since the installation of our image guided microirradiator, consequently showing the robustness and stability of its design.

Dose delivered during anatomical imaging is a concern in small animal irradiation because multiple images are required during a study and this additional dose could bias the experiment. Measurements of the dose required to image with optimal contrast and resolution demonstrated that a minimum of 1/200 of the dose delivered in a treatment fraction (typically 2 Gy) is required for the developed μ EPID imaging. This is an optimal performance that will allow the experimenter to perform animal positioning verification with high accuracy without damaging the integrity of the radiobiological model by delivering radiobiologically significant dose during imaging.

Finally, the μ EPID was tested using animal models with different treatment sites selected because each of these radiobiological models have special requirements in animal handling, positioning, and beam localization. Anatomical and beam images show that the required animal positioning, beam aiming to the target volume, beam profiling and boundary determination, and beam co-registration with animal anatomy can be achieved to accurately perform and satisfy all of these radiobiological experiments with submillimeter accuracy and the specific concerns of the local organs at risk involved in each microirradiation experiment.

The development of this μ EPID was a response to the need for a portal imaging system which meets the experimental requirements of contemporary small animal microirradiation and radiobiological experiments. The constructed micro electronic portal imaging system was calibrated and tested with phantoms and animal models to determine its anatomical imaging resolution along its operating range of energies, image contrast as a function of the dose delivered to the animal subject, co-registration of irradiation beam fluences and anatomical imaging, and calibration for high resolution imaging dosimetry. All of these parameters satisfy the special requirements of contemporary radiobiological experiments, and consequently

validate the development of the μ EPID as a tool to improve and perform image guided preclinical microirradiation therapy.

F. References

- Almond, P. R., Biggs, P. J., Coursey, B. M., Hanson, W. F., Huq, M. S., Nath, R., & Rogers, D. W. (1999). AAPM's TG-51 protocol for clinical reference dosimetry of high-energy photon and electron beams. *Med Phys*, 26(9), 1847-1870.
- Basler scA 1390-17fm Camera Specification. (2007): Basler Vision Technologies.
- Bath, M., Sund, P., & Mansson, L. G. (2002). Evaluation of the imaging properties of two generations of a CCD-based system for digital chest radiography. *Med Phys*, 29(10), 2286-2297.
- Bortfeld, T. R., Kahler, D. L., Waldron, T. J., & Boyer, A. L. (1993). X-ray field compensation with multileaf collimators. *Int J Radiat Oncol Biol Phys*, 28, 8.
- Boyer, A. L., Antonuk, L., Fenster, A., Herk, M. v., Meertens, H., Munro, P., . . . Wong, J. (1992). A review of electronic portal imaging devices. *Med Phys*, 19(1).
- Bushberg, J. T., J. Anthony Seibert, Jr., E. M. L., & Boone, J. M. (2001). *The Essential Physics of Medical Imaging* (2nd Edition) Lippincott Williams & Wilkins.
- CC04 Technical Data. (2012), from http://www.rpdinc.com/html/scandatronix_wellhoffer_compac.html
- Cho, J., Kodym, R., Seliounine, S., Richardson, J. A., Solberg, T. D., & Story, M. D. High dose-per-fraction irradiation of limited lung volumes using an image-guided, highly focused irradiator: simulating stereotactic body radiotherapy regimens in a small-animal model. *Int J Radiat Oncol Biol Phys*, 77(3), 895-902.
- Chui, C.-S., Chan, M. F., Yorke, E., Spirou, S., & Ling, C. C. (2001). Delivery of intensity modulated radiation therapy with a conventional multileaf collimator: comparison of dynamic and segmental methods. *Med Phys*, 28(12), 9.
- Clarkson, R., Lindsay, P. E., Ansell, S., Wilson, G., Jelveh, S., Hill, R. P., & Jaffray, D. A. Characterization of image quality and image-guidance performance of a preclinical microirradiator. *Med Phys*, 38(2), 845-856.
- Convery, D. J., & Rosenbloom, M. E. (1991). The generation of intensity modulated fields for conformal radiotherapy by dynamic collimation. *Phys Med Biol*, 37, 16.
- Dobbins, J. T., Ergun, D. L., Rutz, L., Hinshaw, D. A., Blume, H., & Clark, D. C. (1995). DQE(f) of four generations of computed radiography acquisition devices. *Med Phys*, 22(10), 12.
- Fujita, H., Tsai, D.-Y., Itoh, T., Doi, K., Morishita, J., Ueda, K., & Ohtsuka, A. (1992). A Simple Method for Determining the Modulation Transfer Function in Digital Radiography. *IEEE Trans. on Medical Imaging*, 11.
- Gorokhova, E. I., Demidenko, V. A., Mikhrin, S. B., Rodnyi, P. A., & Eijk, C. W. E. v. (2004). Luminescence and scintillation properties of Gd₂O₂S:Tb ceramics. Paper presented at the Nuclear Science Symposium Conference.
- Graves, E. E., Zhou, H., Chatterjee, R., Keall, P. J., Gambhir, S. S., Contag, C. H., & Boyer, A. L. (2007).

- Design and evaluation of a variable aperture collimator for conformal radiotherapy of small animals using a microCT scanner. *Med Phys*, 4(11), 8.
- Hans, H. (2004). *The Laboratory Mouse, Handbook of Experimental Animals*: Academic Press 1 edition
- Herman, M. G., Balter, J. M., Jaffray, D. A., McGee, K. P., Munro, P., Shalev, S., . . . Wong, J. W. (2001). Clinical use of electronic portal imaging: Report of AAPM radiation therapy committee task group 58. *Med Phys*, 28(5), 25.
- Hill, R. P., Rodemann, H. P., Hendry, J. H., Roberts, S. A., & Anscher, M. S. (2001). Normal tissue radiobiology: from the laboratory to the clinic. *Int J Radiat Oncol Biol Phys*, 49(2), 353-365.
- Izaguirre, E. W., Kassebaum, B. L., Birch, J., Su, I.-T., Goddu, S. M., & Low, D. A. (2009). Development of a High Resolution Image Guided Microirradiator (microIGRT). Paper presented at the Nuclear Science Symposium Conference Record (NSS/MIC), Orlando, FL.
- K602 Precision Electrometer. (2012), from <http://www.cnmcco.com/>
- Kiehl, E. L., Stojadinovic, S., Malinowski, K. T., Limbrick, D., Jost, S. C., Garbow, J. R., . . . Hope, A. J. (2008). Feasibility of small animal cranial irradiation with the microRT system. *Med. Phys.*, 35, 10.
- Kyriakou, Y., Prell, D., & Kalender, W. A. (2009). Ring artifact correction for high-resolution micro CT. *Phys Med Biol*, 54(17), N385-391.
- Lee, S. C., Kim, H. K., Chun, I. K., Cho, M. H., Lee, S. Y., & Cho, M. H. (2003). A flat-panel detector based micro-CT system: performance evaluation for small-animal imaging. *Phys. Med. Biol.*(48), 12.
- Liu, H., Karellas, A., Harris, L. J., & D'Orsi, C. J. (1994). Methods to calculate the lens efficiency in optically coupled CCD x-ray imaging systems. *Med Phys*, 21(7), 3.
- Malacara, D. (2007). *Optical Shop Testing* Wiley-Interscience; 3 edition
- Mayneord, W. V., & Lamerton, L. F. (1941). A survey of the depth dose data. *The British Journal of Radiology*, 14(164), 255-264.
- Medina, L.-A., Herrera-Penilla, B.-I., Castro-Morales, M.-A., García-López, P., Jurado, R., Pérez-Cárdenas, E., . . . Brandan, M.-E. (2008). Use of an orthovoltage X-ray treatment unit as a radiation research system in a small-animal cancer model. *Journal of Experimental & Clinical Cancer Research*(27).
- Motomura, A. R., Bazalova, M., Zhou, H., Keall, P. J., & Graves, E. E. Investigation of the effects of treatment planning variables in small animal radiotherapy dose distributions. *Med Phys*, 37(2), 590-599.
- Murphy, M. J., Balter, J., Jr, J. A. B., Das, I. J., Jiang, S. B., Ma, C.-M., . . . Yin, F.-F. (2007). The management of imaging dose during image-guided radiotherapy: report of the AAPM task group 75. *Med Phys*, 34(10), 23.
- NIST, Hubbell, J. H., & Seltzer, S. M., from <http://www.nist.gov/pml/data/xraycoef/index.cfm>
- Partridge, M., Evans, P. M., Mosleh-Shirazi, A., & Convery, D. (1998). Independent verification using portal imaging of intensity modulated beam delivery by the dynamic MLC technique. *Med Phys*, 25(10), 8.

- Partridge, M., Ramos, M., Sardaro, A., & Brada, M. Dose escalation for non-small cell lung cancer: Analysis and modelling of published literature. *Radiother Oncol*, 99(1), 6-11.
- Partridge, M., Symonds-Taylor, J. R. N., & Evans, P. M. (2000). IMRT verification with a camera-based electronic portal imaging system. *Phys Med Biol*, 45, 14.
- Pidikiti, R., Stojadinovic, S., Speiser, M., Song, K. H., Hager, F., Saha, D., & Solberg, T. D. (2011). Dosimetric characterization of an image-guided stereotactic small animal irradiator. *Phys. Med. Biol.*(56), 14.
- Rastogi, P. K. (1997). *Optical measurement techniques and applications*: Artech House.
- Russ, J. C. (2007). *The Image Processing Handbook* (5th ed.). Boca Raton, FL: Taylor and Francis Group, LLC.
- San, M., Hwang, A., Funk, T., & Izaguirre, E. (2004). Distortion Correction For a MicroCT Subsystem in a SPECT/CT Dual-Modality Small Animal Imaging System. Paper presented at the Society of molecular imaging annual meeting, St. Louis.
- Schambach, S. J., Bag, S., Schilling, L., Groden, C., & Brockmann, M. A. Application of micro-CT in small animal imaging. *Methods*, 50(1), 2-13.
- Segars, W. P., Tsui, B. M., Frey, E. C., Johnson, G. A., & Berr, S. S. (2004). Development of a 4-D digital mouse phantom for molecular imaging research. *Mol Imaging Biol*, 6(3), 149-159.
- Umlaut Software. (2012). *MR Visible Mouse Atlas*.
- Tate, M. W., Chamberlain, D., & Gruner, S. M. (2005). Area x-ray detector based on a lens-coupled charge-coupled device. *Rev. of Scientific Instruments* 76.
- Verhaegen, F., Granton, P., & Tryggestad, E. (2011). Small animal radiotherapy research platforms. *Phys Med Biol*, 56, 29.
- Winkler, P., Hefner, A., & Georg, D. (2005). Dose-response characteristics of an amorphous silicon EPID. *Med Phys*, 32(10), 10.
- Wong, J., Armour, E., Kazanzides, P., Iordachita, I., Tryggestad, E., Deng, H., . . . DeWeese, T. L. (2008). High-resolution, small animal radiation research platform with x-ray tomographic guidance capabilities. *Int J Radiat Oncol Biol Phys*, 71(5), 1591-1599.
- Yuan, L., Holmes, T. C., Watts, R. E., Khosla, C., Broekelmann, T. J., Mecham, R., . . . Rich, K. M. Novel chemo-sensitizing agent, ERW1227B, impairs cellular motility and enhances cell death in glioblastomas. *J Neurooncol*.
- Zhou, H., Rodriguez, M., van den Haak, F., Nelson, G., Jogani, R., Xu, J., . . . Graves, E. E. Development of a micro-computed tomography-based image-guided conformal radiotherapy system for small animals. *Int J Radiat Oncol Biol Phys*, 78(1), 297-305.

3. BUILDING A BRIDGE BETWEEN PRECLINICAL AND CLINICAL RADIOTHERAPY

A. Introduction

Preclinical radiobiological research, specifically in the study of cancer treatment, can involve the use of small animals, such as mice and rats, cancer cell lines, and instrumentation and techniques for imaging and radiation treatment. Small animals provide an *in vivo* representation of tumor growth, cancer progression, and drug and ionizing radiation effects on the target malignancy. In the 1950's, the NCI began to screen anticancer drugs developed through preclinical testing (Curt, 1994). This screening was possible primarily through the use of small animal models. As part of this effort, the development of dedicated instruments to image small animal anatomy and function, such as microCT, microSPECT, microPET and microMRI, played a key role in providing a unified approach for drug development by facilitating preclinical testing of all cancer treatment related drugs (El-Deiry, Sigman, & Kelloff, 2006; Pomper & Lee, 2005). This revolution in preclinical trials had a great impact on accelerating the process for translating cancer drugs into the clinic (Sharpless & DePinho, 2006). Radiotherapy is one of the most commonly used treatment modalities to fight cancer (AMA, 2008), but it has been left behind in this preclinical trial paradigm because of the lack of dedicated instrumentation capable of performing similar cancer treatment with clinical techniques, such as image guided conformal irradiation, IMRT, and radiosurgery. During recent years, the appropriate instrumentation for radiotherapy preclinical research has become available, and we are currently seeing an expansion of translational research in radiation oncology (Baumann et al., 2001; Jong & Maina, 2010; Taghian & Suit, 1999). In this article, we demonstrate the use of this technology modified for this area of research and how preclinical radiobiological experiments using animal models and these novel image guided microirradiators can be implemented to advance radiation oncology. In this work, we will first compare small animal microirradiation with current technology and clinical radiotherapy and then apply these concepts and technologies for a comparative discussion of specific treatment sites such as lung, brain, liver, and spine. These treatment sites were chosen to demonstrate the guidelines for preclinical small animal treatment design with maximized clinical relevance which can be used as a model to foster the advancement of this field for other cancer treatment sites.

B. Preclinical and clinical radiation oncology

Many novel radiation techniques currently proceed to clinical trials only after preliminary clinical data has been obtained or testing is performed with computer and *in vitro* models. Preliminary clinical data can take years to assemble, thus costing additional time and money. Computer models can be a useful tool for the basic understanding of the effects of a therapy on humans. However, these models don't necessarily consider every parameter which could be affected by cancer, such as metastases and immunologic interaction, so the results are limited (Duchting, Ulmer, & Ginsberg, 1998). *In vitro* models can provide good data on the biological reactions of the novel technique, but cells will not react in the same way as large tissues, such as entire organs. To resolve these issues, radiation oncology could follow the example of drug discovery through the use of preclinical testing with small animals. Because the field of radiation oncology is still relatively new, with the first linear accelerator treatment in 1956 (Schulz, 1975), there has not been extensive research conducted on the understanding of the translational path between preclinical and clinical radiation treatments. The same radiation therapy technique used in a human treatment may not produce the same results in a small animal. These discrepancies in results arise from differences in treatment beam energy and dose distribution, treatment subject size, and biological interactions.

Based on the smaller dimensions of a mouse and rat when compared to a human, different treatment modalities and techniques are required for preclinical treatment of small animals. Preclinical treatment modalities include small animal microirradiators or clinical irradiators repurposed for small animal testing. More accurate preclinical testing can arise from the use of protocols and equipment designed for small animals which account for the discrepancies between preclinical and clinical environments. Equipment, such as imaging and therapy devices, has been designed for small animals to provide for their specific sizes and needs which may not necessarily match the design of a device for humans. For instance, if a microirradiator with orthovoltage beams has inadequate filtering, there could be high dose to the bone marrow and skin, which is not seen in human treatment. This bone marrow dose could lead to red blood cell depletion, providing an experimental bias in cancer treatment, because it is unknown if tumor shrinkage is due to proper treatment or a lack of blood supply to the tumor. Another example is the collimation of a microRT beam. A clinical linac will use high resolution multileaf collimators (MLCs) for

an IMRT treatment, which can provide good conformality. Because of the small animal size, MLCs with comparable preclinical resolution may not necessarily be feasible, so while microRTs can successfully treat a tumor to a high radiation dose with alternative methods, surrounding tissues might receive higher unnecessary doses than would be seen in the clinic, leading to an incongruity in a preclinical study. These discrepancies can lead to inaccurate treatment results from a preclinical trial that would not translate to the clinic. One method for handling these issues has been the use of clinical devices for small animal treatment, such as brachytherapy sources which have been adapted to better suit the needs of preclinical treatments (DesRosiers et al., 2003; Stojadinovic et al., 2007). Many universities and hospitals have developed small animal microirradiators with orthovoltage linear accelerators which are better suited for small animal treatments than clinical megavoltage devices (Clarkson et al., 2011; Izaguirre, Price, Su, Birch, & Low, 2012; Wong et al., 2008). Verhaegen (2011) provides an excellent review of preclinical irradiators currently in use and work under development. It has recently been demonstrated that the use of jaws and masks in preclinical treatments can be utilized to deliver conformal treatments to small animals (Izaguirre et al., 2012). Multibeam irradiations have also begun to be used, similar to those used in the clinic. As more microirradiators begin to implement these clinical techniques and protocols, preclinical treatments will improve, with the goal of clinical similarity.

C. Comparative analysis of preclinical and clinical treatment technology and protocols

In a typical clinical radiation therapy treatment, the patient is first imaged on a CT simulator, which features high resolution, distortion free imaging with accurate CT numbers and localization methods for treatment positioning. Distortion free images with accurate CT numbers are necessary for proper treatment planning, to accurately plan the value and distribution of dose in a patient (Mutic et al., 2003).

In the clinic, a patient is imaged sometimes every week and sometimes only once before a treatment to establish the treatment plan. To acquire a pre-treatment image, the patient is positioned as they would be during a treatment using positioning markers on their skin, lasers, and cradles to support the patient. This ensures that the patient is in nearly the same position for imaging and subsequent treatments. If only a pre-treatment image is used throughout the treatment, it is assumed that the patient anatomy will not change significantly. If an image is acquired weekly, the treatment can be adjusted according to the weekly set up,

which can potentially improve the treatment through more adaptive methods, but will provide higher imaging dose. Image guided therapy can use daily images to provide even more adaptive treatments. This type of therapy is typically seen with TomoTherapy using their on-board CT scanner for daily images [TomoProcess].

Clinical linear accelerators produce megavoltage beams, (between 6 and 20 MV) and provide conformal treatment using multileaf collimators (MLCs). In a Varian linear accelerator, the MLCs come in two sizes, 5 mm width in the center portion of the field and 10 mm width on either side (Trilogy, 2012). The smaller width in the center of the field is designed to provide higher dose delivery resolution than is required on the perimeter of the field. A BrainLab micro MLC design uses 3 mm, 4.5, and, 5.5 mm widths for higher resolution (Xia et al., 1999).

Clinical human treatments use a fractionated schedule for many treatment options because fractionation has been shown to improve the radiobiological effectiveness of radiation therapy. There are some methods, such as stereotactic brain irradiations, which occur in a single high dose fraction due to the highly conformal nature of the treatment, but most methods, such as IMRT and brachytherapy, utilize fractionation to reduce dose to healthy tissues. A fractionated schedule delivers a low dose, typically around 2 Gy for an IMRT treatment, every day for several weeks. This is designed to take advantage of the differences in DNA damage repair between tumors and healthy tissue. A tumor will repopulate after having been damaged by radiation, but it has been shown that a tumor will repopulate more slowly than healthy tissue (Withers, 1985). Tumors will also cycle the cancer cells to a more radiation sensitive portion of the cell cycle as damage occurs and reoxygenate the tumor, which increases sensitivity. All of these qualities mean that a tumor will recover more slowly than healthy tissue, so a low daily dose of radiation to a tumor will slowly kill the tumor while allowing the more rapidly healing healthy tissue to recover.

This entire treatment process can be emulated for small animal therapy, with some modifications. For a pre-treatment image, an animal can unfortunately not be instructed to maintain a treatment position, so an animal will typically be anesthetized and restrained in a cradle, if necessary. This method will be used for each treatment, as well. It is unlikely that a researcher will position a mouse exactly the same way for each treatment, so image guided therapy can be used to verify positioning. This image guided therapy utilizes an imaging modality, such as CT or MRI, to provide animal positioning information for each fraction so

treatment can be adjusted accordingly. Our microIGRT uses this method, with a microCT and microRT, to provide highly conformal image guided radiation therapy for each fraction. This method allows a closer match to clinical treatments due to more accurate treatment based on interfraction positioning.

In order to provide more accurate conformal small animal microirradiation, preclinical treatment planning software can be used with forward planning and conformal masks to determine proper treatment. A CT reconstruction is acquired using one mouse from a study to provide the template for treatment. It is assumed that each mouse in the study will be similar in size, due to identical breed and nearly identical age, so that a single treatment plan will be accurate for each of the mice. For implanted tumor treatment, each mouse is implanted with nearly the same number of cells, so tumor growth is similar across each cohort. For a large variance in tumor size, unique masks can be developed as necessary. The template is used to determine the conformal masks to be created and then the treatment plan is developed which will be used throughout the treatment. Although the treatment plan will be the same for each mouse, the positioning will have to be particular to an individual mouse and will change each day. In this way, the treatments are image guided and conformal for each mouse without the complication of an individualized plan for each mouse.

Preclinical microirradiators typically use orthovoltage beams (120-320 keV), which are smaller than megavoltage linacs, thus are more convenient and affordable for preclinical small animal research. However, the difference in beam energy can cause discrepancies between preclinical and clinical treatments. These discrepancies arise from the different beam qualities and dose fall off across the animal. Through proper filtration and isocenter distances, these discrepancies can be accounted for to better translate the treatment beam between preclinical and clinical studies.

The MLCs used in the clinic provide highly conformal treatments and it would be ideal to translate this concept to small animal treatments. In order to provide clinically comparable resolution, a preclinical MLC would need to scale appropriate to a mouse. Mice are roughly 10% of a human, so a 3 mm BrainLab MLC in the clinic would translate to a 300 μm MLC width in a small animal treatment. This size is simply not practical; however, there are methods to provide comparable treatment without the use of MLCs. For instance, some groups are using orthogonal jaws to provide rectangular beams (Izaguirre et al., 2012) or inserts to provide circular beams (Wong et al., 2008). Deng et al (2007) uses a lens system to focus the beam, which improves beam resolution but can be expensive. These methods can provide basic treatments

with limited conformality. Another method is the use of masks, which can utilize 2D or 3D imaging of the target area to create a silhouette of the area to be treated. A mask can then be constructed out of lead or tungsten of an appropriate HVL to conformally treat the target. This method is similar to a treatment option used in the clinic. Using either lead or tungsten masks, or MLCs, the step and shoot method uses multiple beam angles and multiple beam shapes to conformally treat the target. Preclinical irradiators can offer the same treatment, with conformal masks and a rotational source or rotational mouse bed for multibeam treatments.

The use of a fractionated schedule is advantageous for small animal treatment because it is a simple method for a strong correlation with clinical treatments. If a preclinical radiation treatment treats a small animal with a single high dose of radiation, it does not accurately portray the same results which would be seen in humans treated with a fractionated schedule. To improve our preclinical methods, we use a fractionated schedule for the testing of drugs and treatments for small animal research. The schedule is the same as that used in the clinic, 2 Gy per day for up to 40-60 Gy, depending upon the treatment site. This schedule allows for more accurate results to compare to clinical irradiations.

Finally, portal imaging can be used for real time treatment verification, similar to the portal imagers and on-board imagers used on clinical linear accelerators. These portal imagers provide positioning verification of the patient, first through initial set up verification, then through monitoring of intrafraction motion, which can occur even when the small animal is under anesthesia. To monitor this motion, our group developed a portal imager which is installed in the microRT system to provide treatment verification. This preclinical portal imager is similar to electronic portal imaging devices (EPID) used in the clinic, which also use a scintillating screen and a CCD camera. EPIDs are used in the clinic largely to verify proper beam collimation and energy (Herman et al., 2001). For preclinical purposes, we developed a similar imager to verify not only beam collimation and energy but also proper animal positioning (Price, Silviu, & Izaguirre, 2012). The portal imager allows us to ensure accurate radiation treatments and better simulate the clinical environment.

D. Matching preclinical and clinical external beam delivery dose distributions

Beam characterization is used in the clinic to define beam delivery parameters. These parameters are then used during treatment planning to accurately model how the delivery system will perform a treatment. If the treatment beam is well characterized, then each aspect of the treatment with respect to the beam is well understood and can be accounted for to obtain the desired treatment results. These parameters include beam quality, field uniformity, dose fall off, dose rate, and output factor.

When deciding to emulate clinical protocols in small animal treatments, it's important to understand the differences between the two modalities and the challenges microirradiators present. Measurements of microirradiator beams can prove to be more difficult based on the small field sizes and the limitations of ion chambers and phantoms. AAPM's TG-61 is an excellent resource for the calibration of megavoltage irradiators used in a clinical setting (Ma et al., 2001; Yoo et al., 2002). TG-61 uses a 100 cm SSD and 10x10 cm² field size as a reference, but in small animal irradiations, smaller field sizes are required. Clinical acceptance testing and quality assurance practices provide a good framework for microirradiator characterization; however, some characterization methods must be altered to better suit microirradiators. These values are measured with ion chambers or film, both of which can be utilized in preclinical practices. Each of these methods helps ensure proper and repeatable patient treatment. Many of these characterization methods can be translated to preclinical treatment with only minor adjustments, which would create a stronger relationship between clinical and preclinical treatment.

To determine the quality of an orthovoltage beam, the half value layer (HVL) can be calculated. The beam quality is dependent upon filtering of the beam; a more highly attenuating filtered beam will have a higher HVL. An unfiltered orthovoltage beam will be composed of a spectrum of energies between zero and the peak energy, with a higher quantity of lower energy photons. While a filtered beam will still be comprised of a spectrum of energies, the filters preferentially remove the lower energy photoelectric photons, leaving the higher energy photons which are ideal for treatment. The low energy photons, such as those below 150 keV, can cause skin damage and bone marrow depletion when used in a fractionated schedule, such as those used in the clinic. Due to the filtered megavoltage beam used in the clinic, these secondary effects would not be seen in a clinical treatment, creating a discrepancy between the two studies. Through the use

of filters and HVL determination, an orthovoltage beam can safely deliver a fractionated treatment to better match a clinical treatment.

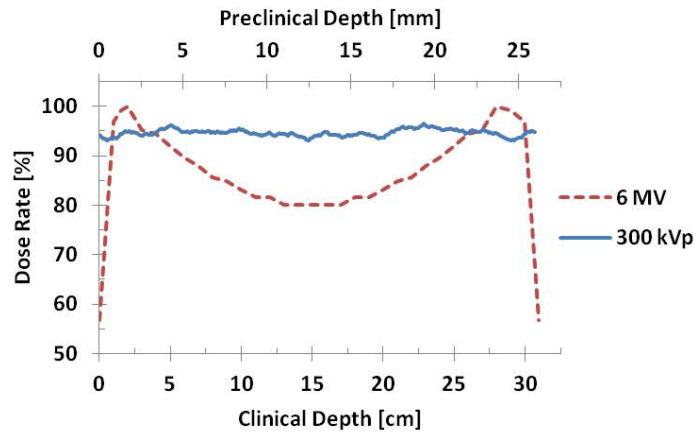


Figure 25. Dose rate versus normalized depth for parallel opposed beams. A clinical 6 MV beam, dotted line, delivered for a 31 cm depth, plotted on the lower x-axis. A preclinical 300 kV beam (189 keV average energy), solid line, delivered for a 25 mm depth and plotted on the upper x-axis.

Depending upon the energy and quality of the beam, it will have a different dose fall off across a patient. Figure 25 compares the dose rate of parallel opposed beams for clinical and preclinical treatments. This figure illustrates the relatively homogenous dose delivery for an orthovoltage beam across an animal diameter, when compared to a megavoltage beam across a human diameter. For megavoltage beams used in the clinic, the dose fall off across a 30 cm human diameter is 60%. This indicates this gradient of dose across the patient. In the clinic, a typical source to surface distance is 100 cm. At 100 cm, the $1/r^2$ effect is less than it is as shorter source to surface distances, such as 40 cm, used in preclinical applications. The other effect to consider is the much smaller diameter of a mouse, around 2.5 cm, when compared a human. All of these effects combine to give a dose fall off of 31% for a mouse when using a beam with a HVL of 3.875 mm Cu, typical for preclinical irradiations. The dose fall off for a rat, with a diameter of 5 cm, is 62% for the same beam quality.

Multibeam irradiations are commonly used in the clinic to spread out the lower doses delivered to healthy tissue surrounding the target. Research has shown that in clinical practice, no more than nine beams are necessary to deliver a sufficiently conformal beam (Soderstrom & Brahme, 1995; Stein et al., 1996). An increased number of beams will complicate the plan and not improve treatment. This beam number is partly based on dose fall of the treatment beam across the patient, as indicated by the PDD. If there is a more

pronounced fall off, there will need to be a greater number of beams to provide a very high dose at the beam intersection with lower surrounding doses. In preclinical irradiations, multibeam irradiations can be used in the same manner, through either rotation of the x-ray source or rotation of the animal, and fewer beams are necessary due to the shallower dose fall off of an orthovoltage beam through a mouse. Typically, three to five beams are sufficient in a small animal orthovoltage irradiation. If we choose to examine the possibility of adding an additional two beams, for a seven beam treatment, the first aspect we must consider is the time required to perform the treatment. A five beam irradiation will require approximately 10 minutes to complete per mouse, which includes the treatment time, gantry rotation time, and positioning verification imaging time. A seven beam irradiation will require 4 additional minutes for each mouse. A mouse study can include up to 20 mice every day, thereby adding 80 minutes to the daily treatment time. Each mouse can require up to 35 fractions, now adding an additional 47 hours to the overall treatment time. Based on the limited improvement in treatment conformity due to increased number of beams, the drastically increased treatment time is not worth the additional beams.

Another important aspect of beam characterization is beam uniformity. Uniformity can be presented through the homogeneity and penumbra of the photon beam. For clinical beams, homogeneity is evaluated across the central 80% of the beam at the level of d_{max} . This d_{max} specification is due to the design of the flattening filter, which produces a flat beam at this predetermined depth. Due to the small focal spot and highly collimated beam used in many preclinical irradiators, a flattening filter is not necessary. However, the flatness can be evaluated at the level of treatment to determine the homogeneity of the treatment beam. Similar to clinical methods, the central 80% of the beam is used to determine homogeneity. The penumbra is determined as the physical distance between the 20% and 80% of the beam fall off.

The output factor can be measured for both megavoltage and orthovoltage beams. The output factor measures the increase in output based on the increase in field size. Like clinical machines, many microirradiators offer beam collimators, in the form of jaws. These jaws can collimate the beam for a variety of field sizes, both square and rectangular. The output factor is normalized to a nominal square field size. This field size is typically $10 \times 10 \text{ cm}^2$ for the clinic and can be set to $10 \times 10 \text{ mm}^2$ for microirradiators. The output factor ultimately is a combination of the collimator scatter and the phantom scatter. Phantom scatter is produced by the ion chamber build up cap used during measurement. A challenge in measuring

the microirradiator output factors arises in the small field sizes, therefore a small volume ion chamber is used in microirradiator characterization than is typically used in clinical characterization. The phantom scatter will change significantly with varying field sizes.

Many of the characterization methods used in the clinic have a range of acceptable values. These acceptable values typically provide the amount the value can divert from the accepted value, and these are based on percentages. The normal percentage of error is 3-5% of the accepted value. This percentage translates well to preclinical and can define how preclinical characterization is done. For instance, when determining the HVL, the value determined experimentally can be off as much as 5% from the known value and maintain tolerability.

E. Metrics to formulate a translational path

A treatment can be defined in terms of the treatment beam, e.g. x-ray energy, beam filter, dose rate, etc, the instrument used to deliver the treatment, and the results of the treatment. The results of a treatment can be defined with a set of metrics which represent the important factors of a treatment. These metrics can then be used to compare preclinical and clinical radiation therapy. These metrics must define a therapy in terms of radiation dose distribution in both the target and normal tissues. The metrics used in this study include the maximum, minimum, and mean dose in the target, target dose homogeneity index, penumbra, conformity index, ratio of mean dose in the target to mean dose in critical structures, and dose non uniformity ratio. Each of these metrics can be determined for clinical human irradiations and small animal irradiations. With these metrics, a human clinical irradiation can be defined which will guide a small animal irradiation to produce similar results. The preclinical treatment beam and delivery instrument should be designed and characterized according to clinical protocols as well as small animal constraints.

The first metric to be determined was the scaling between mice and humans. As seen in table 3, a mouse organ is between 7-10% of a human organ, on average, with some variation in organs, like lungs. For simplicity, a 10% scaling was used to design the experiment for metrics like penumbra, which should scale appropriately from humans to mice. In most cases, care was taken to deliver a conservative value, better than 10%.

Table 3. Organ volume comparison between mice and humans

Organ	Mouse Volume [mm ³]	Human Volume [cm ³]	Mouse/Human [%]
Brain	479	1200	7.36
Kidney	95	280	6.97
Lungs	93	5000	2.65
Liver	424	3828	4.80
Heart	79	612	5.04
Prostate	16	24	8.73
Pancreas	165	72	13.18
Bladder (full)	41	500	4.34

The maximum, minimum, and mean doses in the target define the overall dose delivered to the target. The mean dose should be the planned dose to be delivered to the target. The maximum and minimum doses define the presence of hot and cold spots, respectively. These can then be correlated with the homogeneity index and the penumbra, which define beam distribution and dose fall off around the beam. The homogeneity defines how well a beam is distributing dose across the target. A heterogeneous beam is undesirable for a radiation therapy treatment because it could potentially create hot or cold spots in the target, depending upon the level and location of heterogeneity. A homogenous beam is predictable and will deliver a uniform treatment. The penumbra defines the level of dose fall off around a target. A large dose fall off, i.e. a large penumbra, will cause dose leakage around the target, leading to unnecessarily higher doses to the surrounding healthy tissues. The ratio of mean doses between the target and critical structures defines the level of conformity of the treatment beams. The purpose of a conformal beam is to irradiate the target to a high dose while sparing the surrounding tissues as much as possible.

When comparing the ratio of mean doses of target to critical structures, a large ratio will identify good conformity and target treatment with low doses to the organs at risk. In a clinical treatment plan, dose volume histograms (DVHs) are used to illustrate the dose to a contoured volume. This metric is useful for comparing the doses in each contoured volume, which can include the target tumor and surrounding healthy tissues, to define treatment conformity and efficacy.

For this study, we examined lung, brain, liver, and spinal treatment sites because they are common human therapy sites. Each of the metrics was determined for a typical human therapy at each site. It is important to

note that each treatment site will have different parameters which could affect a treatment and it is crucial to consider each site independently, rather than using a single metric for every site. For instance, a small animal lung treatment could be used to study the effects of healthy tissue irradiation during a treatment. The critical structures in a lung treatment include the contralateral lung, heart, ipsilateral and contralateral breast. In a human treatment, these structures have organ spacing on the order of centimeters, whereas in a small animal treatment, the spacing is on the order of millimeters. A brain irradiation could be used to study the effects of a cancer drug, such as a radioprotector or radioenhancer, in combination with radiation therapy. The effects of both the radiation and the drug must be accounted for, thus providing an ideal opportunity to utilize a small animal trial with several drug and x-ray doses. Each treatment will feature different organs at risk with different sensitivity and response to radiation, so it is important to plan a treatment specifically for the treatment site, as opposed to a generic treatment. Because of these differences between treatment sites, the metrics were defined for each site to better characterize a human treatment in order to design a small animal treatment.

i. Maximum, minimum, and mean dose in the target

The maximum, minimum, and mean doses are the most basic metrics that are going to define how a target or organ should be treated. For instance, the PTV should be almost entirely treated with a minimum of the prescription dose. The maximum dose, i.e. a hotspot, should be limited to a certain volume in the PTV and surrounding structures. Critical organs can be limited by either the mean dose or the maximum dose, depending upon the organ structure. Serial organs, such as the spinal cord and esophagus, will have limits determined by the maximum dose. Parallel organs, such as the lungs and kidneys, are limited by the mean dose. Hotspots in parallel organs are not as detrimental as they would be in a serial organ, due to the nature of the organ. A serial organ, if exposed to a hotspot, could lose function not only in the area exposed, but also further along the path of the organ. Parallel organs are more sensitive to volume effects rather than hotspots. In a preclinical irradiation, the basic idea for limiting hotspots and delivering minimum doses will remain the same; however, dose limits may vary between mice and human organs.

ii. *Target dose homogeneity index and penumbra*

The homogeneity, according to AAPM TG-45, is defined in equation 1.

$$F = \frac{M-m}{M+m} * 100\% \quad 1$$

Where M and m are the maximum and minimum dose values, respectively, in the central 80% of the profile. In the clinic, the homogeneity is acceptable when it is within $\pm 5\%$ (Nath et al., 1994). The homogeneity can be determined for an open field as an input value for treatment planning, as well as in a multibeam conformal irradiation to determine target irradiation homogeneity. These latter values will differ from those for an open field, single beam irradiation. The penumbra is defined as the distance of the dose fall off between 80% and 20%. The homogeneity and penumbra values are shown in table 4 for both a preclinical 300 kVp filtered open field beam and a clinical 6 MV open field beam.

Table 4. Metric comparison for single open field beam

	Homogeneity [%]	Penumbra [mm]
Preclinical 1x1 cm ² beam at 1.25 cm depth	7.0	0.221
Clinical 10x10 cm ² beam at 10 cm depth*	2.6	6.15

*(Moore, 2010)

The homogeneity in the preclinical beam is higher than that of the clinical value based on the stochastic noise which arises from high resolution scanning of GafChromic film, which was used to evaluate the preclinical metrics. Figure 26 illustrates this point with three line profiles of the same film of a 1x1 mm² beam. The graph has been zoomed in to the central 10% of the beam to demonstrate the inherent noise in the film which leads to a less homogeneous beam than actually exists. The inset of the figures shows the full beam profiles.

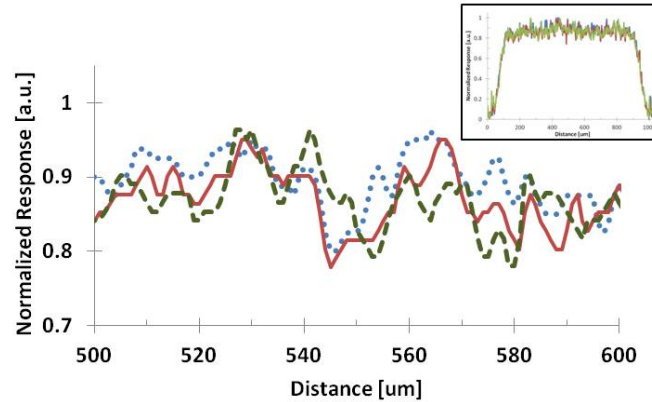


Figure 26. Demonstration of the stochastic noise inherent in high resolution film analysis. Each pixel is approximately 1 μm . The graph has been zoomed in to show a 100 μm distance of the central portion of the beam. Each line represents a line profile of the same film, spaced 2 pixels apart. Inset: Three complete line profiles.

A more practical value is the homogeneity and penumbra of a multibeam irradiation. When using a small field size centered in the beam at the intersection of three beams, the preclinical homogeneity and symmetry are acceptable and comparable to clinical values, as shown in table 5. The improvement in homogeneity for only three beams in a preclinical irradiation is due to the shallower dose fall off for an orthovoltage beam. This leads to the conclusion that fewer beams are necessary in a preclinical irradiation to achieve the same target dose as a clinical treatment. There is a 6% ratio between a preclinical and clinical three beam lung treatment penumbra. When we compare this to the 10% ratio used a starting point when scaling the penumbra, we find that we have exceeded our requirements and produced a more conformal irradiation than originally designed.

Table 5. Metric comparison between clinical and preclinical for a 3 beam lung treatment.

	Homogeneity [%]	Penumbra [mm]
Preclinical	8-13	0.625
Clinical*	10-15	10

*(Moore, 2010)

iii. Conformity index

The conformity index is a helpful method to describe how well a target volume was irradiated. In our preclinical irradiations, the clinical target volume (CTV) includes the tumor or target volume with an

additional margin to account for microscopic disease spread. The planning target volume (PTV) includes the CTV plus a margin which accounts for patient set-up errors and motion. In a brain irradiation, there is little intrafraction motion, so the PTV margin is narrow. In a lung irradiation, the PTV is actually the ITV, which accounts for the total respiratory motion, as described in further detail in the lung cancer example. In order to design a preclinical PTV, the PTV margin used in the clinic, specific to the treatment site, was scaled by 10% and used as the small animal PTV margin. The planned dose is prescribed to the entire PTV and masks are developed to conformally irradiate the PTV. A clinical and preclinical conformity index should be comparable, since these values are relative, as opposed to based on physical dimensions. Therefore, clinical values for the conformity index provide excellent guidelines for designing preclinical irradiations with comparable conformity.

The conformity index is a measure of how well the CTV was treated with respect to the planned target dose, as shown in equation 2.

$$CI = \frac{CTV_{100\%}^2}{CTV * V_{100\%}} \quad 2$$

where CTV=CTV volume, CTV_{100%}=volume of CTV receiving 100% of the prescribed dose, V_{100%}=treated volume receiving 100% of the prescribed dose (Paddick, 2000).

iv. Ratio of mean dose in the organ at risk to mean dose in target

Another method for determining appropriate conformity is the ratio of mean dose in the organs at risk (OAR) to the mean dose in the target. This ratio should be kept as low as possible, to deliver the entire prescription dose to the PTV and avoid dose to the surrounding healthy tissues. This ratio for clinical irradiations is a good value to match for preclinical irradiations. Preclinical irradiations will have a smaller penumbra and therefore improved dose fall off around the target, but due to the limited technology, the conformity may not be as good as clinical irradiations. Through a combination of these advantages and disadvantages, the dose ratio between the organs at risk and the target should be comparable for preclinical irradiations.

v. *Dose non-uniformity ratio*

In order to measure the magnitude of a hotspot in the target, the dose non-uniformity ratio (DNR) is the ratio of the volume of the CTV receiving the maximum dose to the volume of the CTV receiving the prescribed dose. Hotspots should be avoided in order to maintain appropriate homogeneity in the treatment as well as reduce the possibility of producing tumor necrosis (Saw & Suntharalingam, 1990; Zwicker & Schmidt-Ullrich, 1995).

vi. *Dose volume histograms*

Dose volume histograms display the percentage of a contour's volume receiving different dose totals. These provide an excellent view of delivered conformity based on the shape of the curve. For instance, a target contour DVH should be level at nearly 100% of the volume up to the prescription dose, with a sharp fall off at the end. An OAR, on the other hand, should have a low percentage of the volume receiving a low dose, with the curve ending at the maximum allowable dose. A DVH graph can provide a quick visual analysis of the effectiveness of a treatment based on the maximum doses and conformity as indicated for each contour.

F. Experimental methods

Clinical treatment plans for each treatment sites were analyzed using the DVH outputs. The metrics were evaluated for the target, typically the CTV or PTV, and the OARs. The OARs typically included the healthy tissue of the organ surrounding the target as well as one additional adjacent organ.

For the preclinical treatments, three or five beams were chosen for each treatment site and delivered using a circular aperture to treat a basic tumor in the organ or a mask to treat the entire tumor, specific to the lung treatment. Radiochromic film (GafChromic, 2010) was inserted in a tissue equivalent mouse size phantom. The body phantom was used for the lung, liver, and spine treatment, with a 25 mm diameter, and the head phantom was used for the brain irradiation, with an 18.75 mm diameter. The beams were equidistantly arranged for a complete 360° treatment around the entirety of the phantom. In the case of a tumor treatment, the circular aperture was chosen such that the entire CTV was irradiated to 2 Gy and 10 Gy at the intersection of the beams, according to the scaled CTV value. A PTV was evaluated by scaling the

clinical margin by 10% for small animal applications. The 2 Gy films were used to identify doses to the target and the 10 Gy films were used for OAR dose evaluation. GafChromic saturates at 5 Gy, so the 10 Gy films were only analyzed around the saturated target, in order to ensure that the doses to surrounding organs were accurate. A 2 Gy irradiation would not necessarily reflect very low doses to surrounding areas. Films were acquired for treatments in both the transverse and coronal views. Using the same batch of GafChromic film, calibration films were acquired with the microIGRT from 0 to 5 Gy in increments of 0.5 Gy. After 24 hours, the film was scanned in full color, and the red spectrum of the image was measured. The beam images were overlaid with our microCT images and the target and OARs were contoured. The contoured images were analyzed in MathCAD to determine the dose from the pixel intensity values and the calibrated films, and these doses were scaled to the prescribed dose. The transverse and coronal film results were combined in MathCAD to produce the weighted averaged DVHs. An isodose line distribution was created in ImageJ (NIH, 2012) with a color intensity spectrum which ranged from 105% at the center hotspot to 0% at the perimeter of the film to visualize the isodose contours.

It is important to note that the DVHs were determined in a phantom, rather than a heterogeneous treatment plan, so the results do not yet account for tissue attenuation variation in the mouse body. In-house developed treatment planning software is currently under development in our lab for subsequent evaluations. Using these DVHs, metric values were determined in the same manner as the clinical treatment plans.

For each treatment site, a table has been produced comparing preclinical and clinical treatments. The metrics in the tables include the volume of the CTV receiving 100% of prescribed dose, the conformity index, and dose non uniformity ratio. The tables also include a coefficient of agreement, which is the percent difference between the preclinical and clinical metric, where the clinical value stands as the gold standard. This coefficient is used as a measure of the similitude between the preclinical and clinical values. In cases of conformity index and CTV coverage, we'd like the preclinical metric value to be comparable or higher than the clinical value. However, in the case of DNR, we'd like the preclinical value to be comparable or lower than the clinical value. The coefficient in the table, to define whether the preclinical value is better or worse than the clinical, will use a positive value to represent a metric which is better than

the clinical, and a negative value for a preclinical metric which is worse than the clinical value. It's important to understand that negative does not mean "less than", it simply means "not as good".

G. Cases of study

i. Partial and whole lung irradiation

In humans, non small cell lung cancer is the second most common cancer in the US, behind prostate cancer in men and breast cancer in women. It is also the number one cause of cancer death in the world (Jabbari, Hansen, & Haas-Kogan, 2010). Based on this prevalence, it is an excellent choice for improved treatment options. Inoperable stage T2 tumors are typically treated with 2 Gy daily fractions up to 66 Gy. There have been some studies concerning hypofractionation and stereotactic body radiation therapy, using 4 Gy fractions for a total of 48 Gy. An IMRT plan will use between 6 MV and 10 MV beams for a gross tumor volume (GTV) which includes the primary and nodal disease, which are lymph nodes greater than 1 cm. The CTV includes the GTV and a 1-1.5 cm margin, and the PTV adds an additional 0.5-1.5 cm margin for set up error and respiratory motion. The organs at risk in this treatment are the spinal cord, contralateral lung, esophagus, and heart.

In order to treat a lung tumor accurately, motion management is required in a clinical treatment. After 3D imaging has been acquired, maximum intensity projection (MIP) images are produced. These images indicate the location of the tumor in each phase of the breathing cycle, thus indicating the full range of motion of the tumor. The breathing cycle is monitored via a surrogate, such as bellows or infrared tracking. After the breathing cycle and tumor motion is well understood, a treatment can either use gating to turn off and on the treatment beam when the tumor is in a particular phase of the breathing cycle or use the internal target volume (ITV) to treat the tumor during its entire motion. There are advantages and disadvantages to both systems. Gating will require a greater treatment time, especially if the patient's breathing motion is erratic. In preclinical mouse lung treatment gating is not always a viable treatment option based on microirradiator technology and mouse breathing rate. Adult humans typically take 12-20 breaths per minute (Sherwood, 2006) while a mouse will take 163 breaths per minute (Green, 1966). When mice are fully anesthetized their breathing rate is reduced to about 60% of their typical rate, around 100 breaths per minute (Cavanaugh et al., 2004). The typical breathing motion is a gasping breath with a relatively long

time between breaths. Compared with humans, this is a very rapid breathing rate and would mean that beam time on would be short, assuming a breath is every 600 msec. However, a shutter would be required to eliminate the beam between treatments, and this shutter would need to be very fast and rugged, to endure opening and closing 100 times per minute. In addition, the total treatment time would be drastically increased, since a large portion of the total treatment time is with the shutter closed. This would decrease animal throughput and reduce the preclinical trial efficiency.

Through the use of either a bellows system or a ventilator, microCT imaging can be gated to improve resolution and allow for imaging the lung at full inspiration, when the volume is greatest, thus improving contrast. Using this same bellows or ventilator technique, the breathing cycle can be viewed and MIP images can be produced to generate an ITV. Similar to the clinic, an ITV is developed from the MIP images to determine the maximum target motion. Based on current microCT systems with cone beam imaging, a ventilator or bellows is not necessary. During a microCT scan with a short integration time, such as that used with the microIGRT, the point of maximum inhalation and exhalation will be viewed based on the motion of the diaphragm or motion of the tumor. From this, an ITV can be developed. Treating an ITV poses the same difficulties in small animal irradiations as it did for clinical irradiations, which is the overdosing of healthy tissue when treating a small portion of the lung, like a tumor. When treating the entire lung, the overall motion of the lung is limited, so there is little irradiation outside the PTV. When treating only a portion of the small animal lung, the tumor will move up to 2.5 mm, based on the motion of diaphragm, so the ITV will irradiate only a small volume of healthy tissue in a small animal. This motion can be limited if a compression device is added. Compression will reduce motion without hindering the animal's ability to breathe.

When considering the OARs, according to QUANTEC, the heart has a mean dose limit of 26 Gy to the entire volume and 30 Gy to 46% of the volume. Because the heart is considered a parallel tissue, the mean dose is of more concern than the max dose. The spinal cord has a max dose limit of 50 Gy to 5 cm of the organ. The contralateral lung has a mean dose limit of only 7 Gy to avoid pneumonitis. Finally, the esophagus has a mean dose limit of 34 Gy or up to 35 Gy to 50% of the volume (Gagliardi et al., 2010; Marks et al., 2010).

The most typical metric used to define a lung treatment is the V20, which is the percentage of lung tissue receiving 20 Gy. For clinical lung treatments, the V20 should be less than 35%. This value stems from clinical data pertaining to the onset of pneumonitis in patients. On average, if less than 35% of the lung receives a total dose of 20 Gy, then the risk of pneumonitis is very low, thus improving the patient quality of life. This value is based on years of experience with megavoltage irradiations of human tissue. It can be theorized that, based on a different beam energy and tissue volume, this value in small animals may not be equivalent. This will be examined in future studies, but for current our current designs, it is assumed that this value is relevant to orthovoltage treatments.

Lung tumor sizes will vary, but for an example, we will use a PTV of 900 cm³ and a CTV of 600 cm³, according to a clinical treatment plan with nine beams at 6 MV. For a typical fractionated lung treatment, the maximum, minimum, and mean dose in the PTV are 73, 43, and 68 Gy, respectively. As an example of a typical organ at risk, we will look at the heart dose. The ratio of the mean dose in the heart to the mean dose in the PTV is 39%. This ratio is a good indicator of the distance of the critical organ from the PTV but also the importance of reducing dose. To evaluate the conformity index, the prescription for a lung irradiation is 200 cGy per fraction to 97% of the PTV for 33 fractions, for a total of 6600 cGy. In a typical treatment, 90% of the CTV receives the prescribed isodose, while a small volume of the ipsilateral and contralateral lung, the esophagus, the heart, and the liver also receive up to the prescribed dose. The metrics for a typical clinical lung treatment are shown in table 6.

Now we shall compare these values to a simple preclinical irradiation with three beams at 300 kVp, with a slight offset of the beam intersection from the center of the mouse, to irradiate a tumor in the right lung. The isodose contours for the three beam treatment are shown in figure 27, overlaid with microCT images of a mouse in both the coronal and transverse views. The CTV and PTV were scaled by the same ratio seen in a clinical treatment, specific to the lung, to determine a treatment volume typical of what is seen in mice lung tumor volumes (Regales et al., 2007).

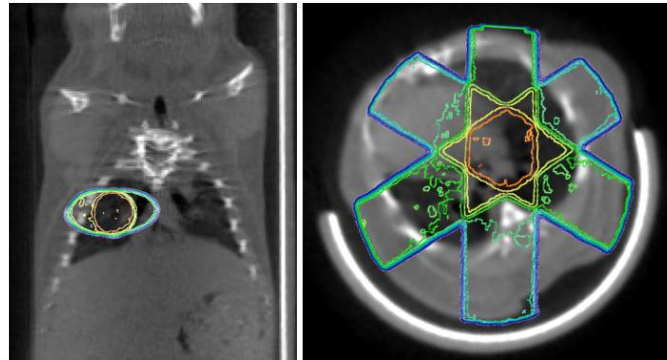
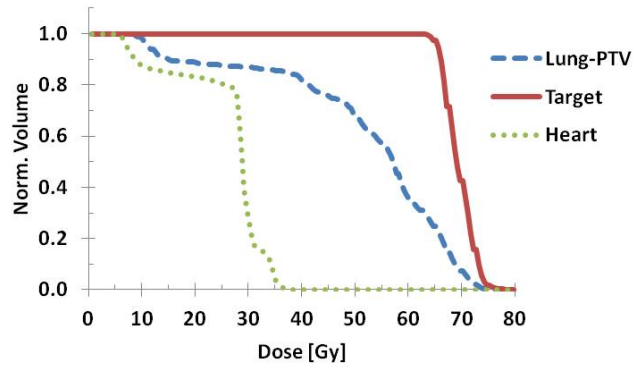


Figure 27. Three beam lung tumor irradiation. Top: DVH illustrating the doses to the target, heart, and healthy lung. Bottom: Isodose contours overlaid with microCT imaging.

According to table 6, the preclinical CTV coverage is comparable, within 11%, but based on the negative coefficient value, it's clear that the preclinical metric value is not better than the clinical value. The conformity is 16% lower than the clinical value, thus indicating that this treatment is not as clinically comparable as we would like. The dose non uniformity ratio is higher than the clinical value due to a larger hot spot. This hot spot is likely due to underestimating the intersection dose of the three beams. The minimum, mean, and maximum doses in the target are 62, 69, and 87 Gy, respectively.

Table 6. Comparison of preclinical and clinical metrics for a lung tumor treatment

	Clinical		Preclinical		Coefficient of agreement [%]
CTV	623.29	cm ³	10.32	mm ³	
PTV	913.77	cm ³	12.06	mm ³	
CTV V _{100%}	90	%	80	%	-11.11
CI	73	%	61	%	-16.44
DNR	5	%	10	%	-100.00

We then looked at the dose to the organs at risk by overlaying the multibeam film image with the microCT reconstruction of a BALBc/Byj mouse, from Jackson laboratories, acquired with our microIGRT system. Using this method, we developed DVHs for the target within the lung, the entire lung, and the heart, as an organ at risk. The DVH in figure 27 clearly indicates good dose conformity of the target, with a curve fall off at the prescribed dose of 70 Gy. The heart receives a maximum dose of 35 Gy, with less than 25% of the volume receiving less than 30 Gy, as allowed by QUANTEC standards. This heart dose is even higher than we would like to see, but the higher dose is based on the relatively high volume of a mouse heart compared to a human heart. A mouse heart is 5% of a human's, while a mouse lung is only 2.5% of a human lung. A larger heart volume means that more of the heart will be in the beam path. This would indicate that improved conformity, with masks rather than a circular beam, will reduce the heart dose. When we compare the mean dose in the heart to the mean dose in the target, the ratio is 38%, which is almost exactly the result for a clinical treatment. Even though the heart dose is higher than seen in humans, the ratio relative to a mouse lung target is comparable, possibly indicating that the treatment is clinically comparable based on the requirements of a mouse and an orthovoltage treatment. The clinical V20 requirement was not met in this treatment, so it can be assumed that this treatment is not yet clinically comparable and requires improvement. A more conformal beam, as opposed to our basic circular aperture could potentially reduce healthy lung tissue dose.

We also wanted to examine the effects on a total lung irradiation, based on the need for an animal model to predict the onset of fibrosis and pneumonitis. By irradiating the entire lung, we can provide uniform irradiation to all healthy tissue and begin to understand the different tissues within the lung and when radiation side effects will occur.

A three beam treatment was developed using a microCT reconstruction on which the entire right lung was contoured. A back propagation of the contour was used to develop a mask from our in-house developed tungsten epoxy method. Two masks were created, one for an AP/PA beam and one for a beam at a 45 degree angle, with a shape specifically designed to spare the heart. These masks were used in our BDMA and a three beam treatment was delivered. The DVH results are shown in figure 28 for the entire irradiated lung as the target, and the left lung and the heart as healthy tissues. Also shown in figure 28 are the colored intensity images of the beams to illustrate high intensity throughout the entire treatment area and very sharp

penumbra at the edges. This treatment is not typically conducted in the clinic, so the results are purely for preclinical applications.

As seen in the figure, the entire targeted lung is receiving 100% of the prescribed dose to 50% of the volume. Because a single lung mask is used for an entire cohort of mice, based on the assumption that the same breed and age of mouse will produce the same size lung, some compromise is made in beam size. This is clinically acceptable coverage of the target. The heart is receiving less than 20 Gy to 20% of the volume, so it is acceptably spared. The contralateral lung is receiving almost zero dose and has been entirely spared. This treatment is appropriate for studies of the onset of radiation side effects and will be useful in future preclinical studies for determining dose limits in the lung.

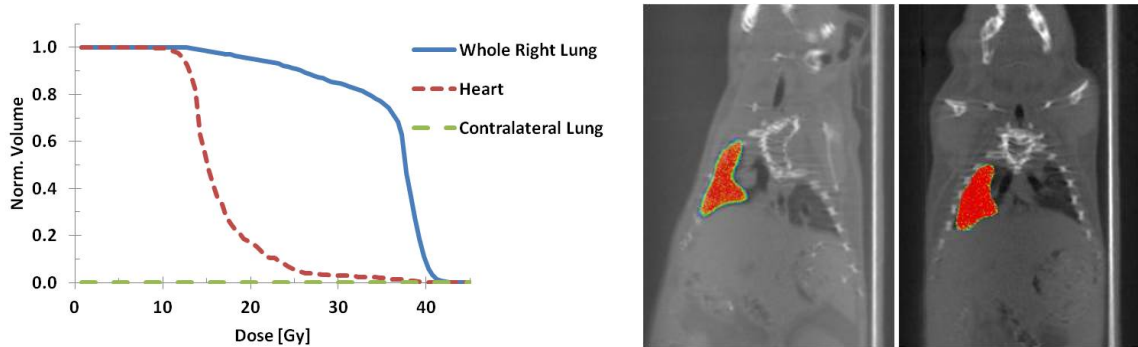


Figure 28. Three beam irradiation of the entire right lung of a mouse. Left: DVH with the targeted right lung, contralateral lung, and heart contoured. Center: Intensity map overlay of the 45 degree angle beam. Right: Intensity map overlay of the AP/PA whole lung irradiation.

ii. Glioma irradiation as a case of brain cancer malignancy

A common brain tumor, especially in pediatric patients, is a glioma. When treating children, it's vitally important to reduce dose to healthy tissue as much as possible, to prevent radiation side effects which could occur in later years. With very young children, they potentially have more than 60 years of life remaining, so side effects in 10-15 years could be detrimental. When the brain is irradiated, the acute and late effects of radiation therapy can be significant. Improvements in radiation delivery methods could decrease these effects and reduce morbidity. Acute effects include nausea, vomiting, vertigo, and headache. Late effects include tissue necrosis, cognitive deterioration, and possibly death. The two most important aspects of brain irradiation to consider to reduce normal tissue complications are dose and volume. For instance, the complication rates can change significantly for a target diameter change of only 10 mm (Lawrence et al.,

2010). One organ at risk, rather than being a particular portion of the brain, is the healthy brain tissue itself. One does have to consider other specific organs, such as the optics, but overall, the healthy brain tissue is the most vulnerable organ at risk.

There are several treatment options, especially when considering fractionation. The brain is highly susceptible to changes due to fractionation, so options include daily fractionation, twice daily fractionation, and hypofractionation using devices such as Gamma Knife. The most important aspect of brain irradiation is positioning precision of both the beam and the target (Maitz et al., 1995). Because there is no respiratory or cardiac motion in the brain, irradiation precision can be much greater, hence the use of hypofractionated treatments. Patient positioning is achieved through stereotactic holders, such as the Leksell G Frame for single fraction treatments (Elekta, 2012). This frame attaches to the patient's skull with small metal pins and is then attached to the treatment machine to define the treatment coordinates. For multiple fractions, the Leksell Extend frame can be used, which utilizes a bite block to hold the patient in position for the treatment and allow repeatable positioning. This same type of stereotactic system can be used in small animal irradiations with a bite block and neck support. Because the animal must be anesthetized during treatment, the front teeth can be clamped into place within a nose cone to hold the mouse still and provide anesthesia. Adjustable pins at the base of the neck can hold the mouse in place and can be marked for each mouse to provide repeatability between fractions.

In addition to stereotactic holders to improve target positioning, image guidance can be utilized in small animal irradiations to further enhance positioning precision. Clinical protocols use 2D-2D matching with on-board kV or MV imaging devices before and during treatment to position the patient for each treatment fraction according to daily changes. This same method can be used with preclinical irradiations through the use of the μ EPID, which provides real time target and beam positioning verification to account for inter- and intrafraction motion.

Useful metrics for brain irradiations include the max, min, and mean dose to identify hot and cold spots. Because brain irradiation can be hypofractionated, it's important to provide very conformal and very uniform dose. A cold spot in a fractionated treatment may occur for one or two fractions. This scenario is undesirable, but can still provide a successful treatment because the same spot will theoretically be treated with the full prescription dose in the remaining fractions. In a hypofractionated treatment, a cold spot can

be detrimental because it could spare tumor tissue, thus leading to an unsuccessful treatment. Likewise, a hot spot in a fractionated treatment could be overlooked, but in a hypofractionated treatment, it could lead to tissue necrosis. Therefore, the max, min, and mean dose can identify the homogeneity of a treatment. Similarly, the homogeneity and conformity index and penumbra will provide a measure of dose distribution across the target. DVHs are a good source of information for defining how well organs at risk were spared relative to target irradiation. The brain stem, according to clinical QUANTEC data, has a limit of 54 Gy to the entire volume and less than 59 Gy to 1-10 cm³ of the volume to avoid permanent cranial neuropathy or necrosis (Lawrence et al., 2010). The optic chiasm has a D_{max} value of 55 Gy to avoid optic neuropathy. The brain itself has a D_{max} value of 60 Gy to 1/3 of the total volume to avoid necrosis. A highly conformal beam is crucial for brain irradiation and can be accomplished with treatment planning software and a microirradiator. As seen in figure 29, a three beam irradiation is sufficient to provide conformal, high dose treatment to the malignancy with limited healthy tissue irradiation.

In a clinical brain irradiation, the PTV is defined as the CTV plus a 5 mm margin to account for set up error and beam penumbra. In a preclinical irradiation, the PTV can be reduced to the CTV plus a 0.05 mm margin, which was scaled from a clinical brain treatment by 10%.

An important metric in a clinical brain irradiation is the target coverage. 95% of the prescription dose should be delivered to more than 98% of the PTV. Another important aspect is the shape of the 80% isodose line. The 80% isodose line should follow the shape of the PTV, to further improve conformity and avoid high dose spillage outside the PTV. To avoid hotspots, no more than 20% of the PTV can receive more than 110% of the prescription dose. Conversely, to avoid underdosing in the target, no less than 1% of the PTV can receive less than 93% of the prescription dose. These metrics define conformity and target coverage, which should be independent of treatment environment, therefore the preclinical values for these metrics should be, at the minimum, the same. In other words, the preclinical conformity and PTV coverage should be at least identical to clinical values.

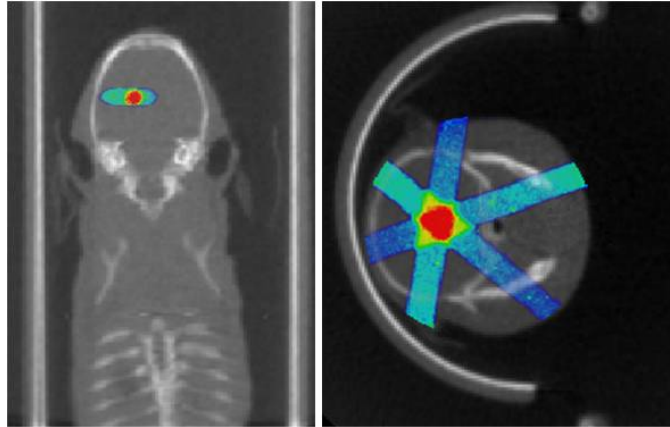
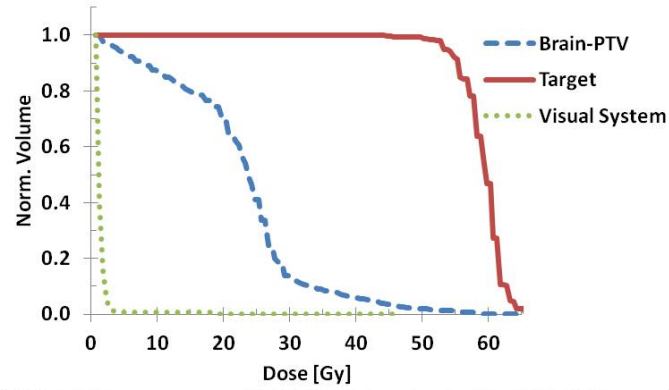


Figure 29. Three beam brain tumor irradiation of a mouse. Top: DVH with target, healthy brain tissue, and visual system contoured and a prescribed dose of 60 Gy. Bottom: Coronal overlay. Bottom right: Transverse overlay.

Typical clinical maximum, minimum, and mean doses for a glioma irradiation are 60, 49, and 64 Gy, respectively for a PTV volume of 245 cm³, with a CTV volume of 170 cm³. Typical ratios between mean doses in critical structures and the mean dose in the PTV are 27% and 13% for the optic chiasm and ipsilateral lens, respectively. 80% of the CTV receives the prescription dose, and 43 cm³ of organ volume external to the target receives 100% of the prescription dose, which includes the healthy brain tissue and right hippocampus. These values are compared with the preclinical values in table 7.

Table 7. Comparison of preclinical and clinical metrics for a brain tumor treatment

	Clinical		Preclinical		Coefficient of agreement [%]
CTV	171.52	cm ³	0.50	mm ³	
PTV	246.21	cm ³	0.64	mm ³	
CTV V _{100%}	80	%	70	%	-12.50
CI	61	%	62	%	1.64
DNR	1	%	3	%	-200.00

A preclinical three beam irradiation was delivered to a mouse, and the circular aperture chosen for this irradiation was developed using a scaled CTV value from the clinical treatment plan described above.

The DVH was calculated for a glioma irradiation, shown in figure 29, considering the target, the entire brain, and the visual system as OARs. The visual system includes the eyes and the optic nerve, and as seen in the figure, the target has good conformity, with low dose to the entire brain and to the visual system. The color intensity maps in figure 29, overlaid with microCT images, illustrate the homogeneous irradiation at the center of the beam with a narrow penumbra. There is little dose outside of the beams, with high intensity at the intersection.

The brain minus the PTV receives no more than 55 Gy, with less than 10% of the volume receiving more than 30 Gy. QUANTEC requires that the optic chiasm receive no more than 55 Gy, and the visual system, in this irradiation, received a maximum dose of only 4 Gy. The ratio of the mean doses in the visual system and the brain is less than 0.5%, indicating very low dose to the visual system. This value is lower than the clinic ratio, so a comparable value was, in this case, improved upon. This very low visual system dose is due to the position of the tumor in the brain. The treated CTV had a 0.5 mm^3 volume, compared to the entire brain volume of 480 mm^3 . The positioning of the treatment beams was such that the visual system were only slightly within the beam path and received very little dose.

iii. Liver tumor treatment

Hepatocellular cancer is common in patients who suffer from Hepatitis B. Radiation therapy can be used to treat part of the liver at each lesion. It can also be used to treat the entire liver as palliative treatment or if an abundant number of lesions are present. In order to visualize the tumor for treatment planning, a CT with contrast agent is performed. This helps distinguish the liver from the surrounding soft tissue. The organs at risk around the liver are the bladder and the lung and must be considered when determining total dose. The total mean dose which can be safely delivered to a single kidney is 1500 cGy and V80 for the bladder should be less than 15%. When treating the entire liver, the typical treatment is 21 Gy over 7 fractions. Radiation induced liver disease is a possible side effect of radiation therapy and typically occurs 2-8 weeks following treatment (Chen, Huang, & Roach, 2010).

Stereotactic body radiation (SBRT) is often used to treat lesions in the liver, with 13 Gy and 3 fractions or 18 Gy and 6 fractions. SBRT requires high resolution imaging and contrast agents to precisely locate and delineate the target. In order to improve motion management, a body frame is used in the clinic to reduce motion, excluding breathing. Breathing motion is controlled through treatment gating. Finally, on-board imaging is used to verify proper positioning of the target. With these motion management controls, treatment can be reduced to 1-5 high dose treatments, as opposed to a typical 20 fraction treatment with much smaller doses. As mentioned in the lung treatment section, treatment gating is not practical for the breathing rate of mice, however similar motion management techniques can be employed, such as a body frame. While the small animal is anesthetized, a body frame can be inserted into the mouse bed to securely hold each arm and leg, the tail, and head, to minimize lateral and transaxial motion. The image guidance system of a microirradiator can be used similarly to the clinic, to verify subject and beam positioning.

For partial liver RT of primary liver cancer, QUANTEC limits the mean dose to less than 28 Gy for 2 Gy fractions. For our preclinical study, both lungs were considered to be organs at risk, with a limit of less than 20 Gy to 30-35% of the volume (Pn et al., 2012).

In a clinical IMRT treatment of the liver, the conformity index is 69% for a 334 cm³ CTV and a prescribed dose of 5500 cGy. In this treatment, only 5 fractions were delivered, at 1100 cGy per fraction, for a prescribed dose of 5500 cGy. 100% of the CTV receives 100% of the prescribed dose. The dose non uniformity ratio is low, at only 1%, indicating very few or very small hot spots, with the highest dose at 116% of the prescribed dose. The mean dose ratio between the organ at risk, the lungs, and the liver was 28%.

Table 8. Comparison of preclinical and clinical metrics for a liver tumor treatment

	Clinical		Preclinical		Coefficient of agreement [%]
CTV	334.07	cm ³	13.08	mm ³	
PTV	535.07	cm ³	15.14	mm ³	
CTV V _{100%}	100	%	90	%	-10.00
CI	69	%	76	%	10.14
DNR	1	%	10	%	-900.00

When we compare this to a preclinical treatment, the prescription dose is 60 Gy delivered in 30 fractions. The CTV volume is 13 mm³, and the PTV volume was scaled according to the clinical ratio. The preclinical metrics are compared in table 8 with the clinical metrics for a liver treatment.

The DVH, as seen in figure 30, illustrates the good conformality for a prescribed dose of 60 Gy. The lungs are well below the QUANTEC limit, with a maximum dose of 22 Gy and a mean dose of 7.5 Gy, so there is little dose to the organs at risk. The position of the tumor within the liver was several mm superior to the lungs, thus reducing the lung dose. The ratio of mean doses between the lungs and the liver is only 13%, compared to a clinical value of 28%, which indicates lower lung dose compared to the target dose in the preclinical treatment compared to the clinical treatment. The liver, however, has slightly lower mean dose than the QUANTEC limit. The mean dose in the liver minus the PTV is 26 Gy.

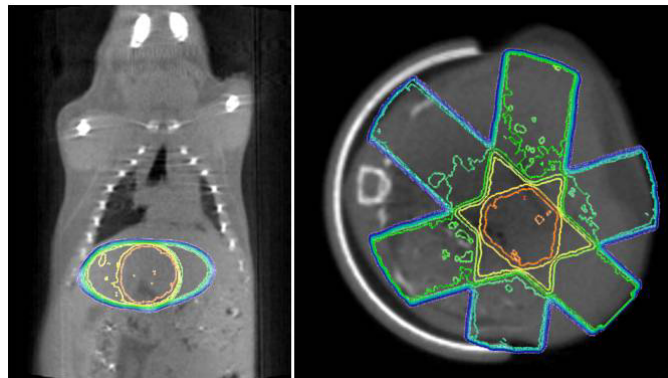
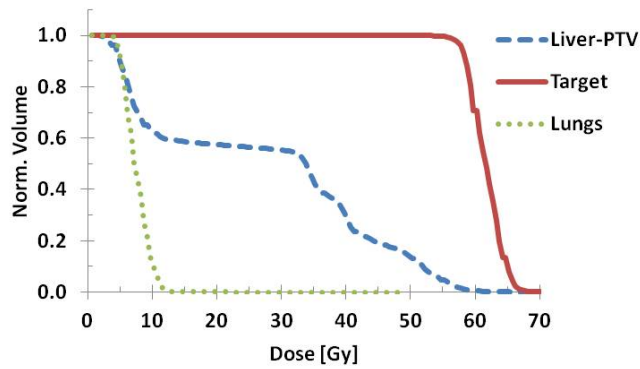


Figure 30. A three beam liver irradiation with a circular aperture. Top: DVH for the target in the liver, the healthy liver tissue, and the lungs. Bottom: Isodose contours overlaid with microCT images.

iv. *Partial spinal irradiation*

Spinal irradiation can be localized to treat a primary spinal cord tumor, or include the entire spinal cord, for palliative treatment. For localized primary spinal cord treatment, fractionated radiation therapy or SBRT

can be utilized. Radiation therapy can either follow surgical resection or stand as the primary treatment. In fractionated treatment, 50-54 Gy is delivered to the tumor in 2 Gy fractions, while in SBRT, 10-20 Gy is delivered in 1 fraction. Because the spinal cord is a serial organ, it is important to limit the maximum dose to a small area of the cord. According to QUANTEC, the maximum dose to 5 cm of the cord is 50 Gy to reduce the risk of myelopathy (Kirkpatrick, Kogel, & Schultheiss, 2010).

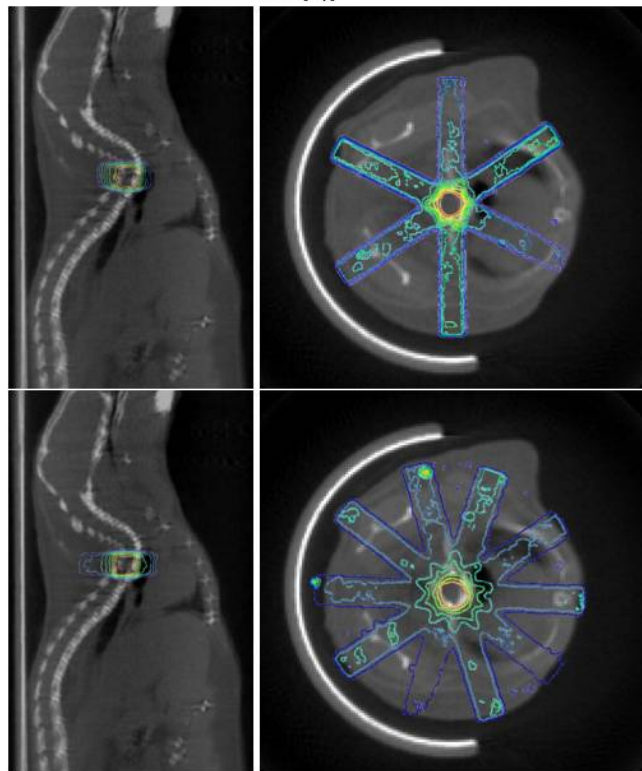
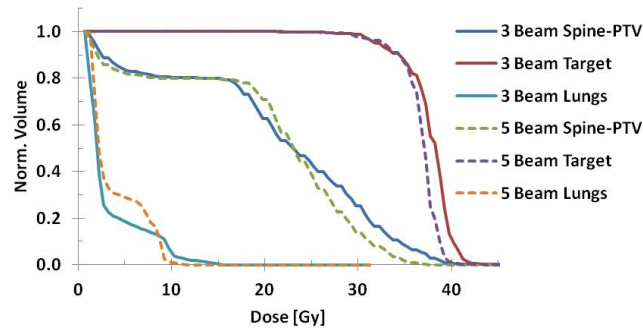


Figure 31. Partial spine irradiation of a mouse using three and five beams. Top: DVH for both three beams (solid lines) and five beams (dashed lines). Center: Isodose overlay of a three beam treatment using a square aperture with microCT sagittal and transverse images. Bottom: Isodose overlay of a five beam treatment using a square aperture with microCT sagittal and transverse images.

A typical clinical treatment of a spinal tumor is a fractionated dose of 36 Gy to the PTV, which is roughly 35 cm³. An organ at risk for a spine treatment includes the lungs, with a QUANTEC limitation of less than

35% of the volume receiving less than 20 Gy (Kirkpatrick et al., 2010). The clinical metrics are shown in table 9.

For a fractionated preclinical partial spinal cord irradiation, we delivered 2 Gy per day for 38 Gy to the CTV. A circular aperture was used to deliver a three beam treatment and a five beam treatment. The DVH comparison for the target, total spine, and lungs is shown in figure 31 for both three and five beams. Also in figure 31 are shown the isodose contours of a three and five beam treatment overlaid with microCT images in the sagittal and transverse views. The sagittal images were ideal in this treatment for viewing the entire volume of the spine, whereas a coronal view would have shown only a portion of the spine in a single slice and therefore skewed results. The metrics are shown for both preclinical beams and the clinical treatment in table 9. When comparing three and five beams, there is a reduced hotspot for a five beam treatment, but the conformity is almost exactly the same. The maximum and mean doses in the target in a three beam treatment are 42 and 36 Gy, respectively, compared to 40 and 35 Gy, respectively, for a five treatment. Based on the DVH data, the target coverage is actually reduced in a five beam treatment. Based on this analysis, and the time which can be gained by reducing the number of beams, it is found that there is no substantial gain from using five beams versus three beams.

Table 9. Comparison of preclinical and clinical metrics for a spinal tumor treatment

	Clinical		Preclinical 3 Beam		Coefficient of agreement [%]	Preclinical 5 Beam		Coefficient of agreement [%]
CTV	NA	cm ³	1.87	mm ³		1.87	mm ³	
PTV	34.23	cm ³	2.46	mm ³		2.46	mm ³	
^{CTV} V _{100%}	50	%	80	%	60.00	75	%	6.25
CI	50	%	47	%	-6.00	75	%	59.57
DNR	5	%	10	%	-100.00	1	%	90.00

When examining the preclinical DVH, one can see that the healthy spine does not receive more than the maximum dose at any point in the spine. The maximum dose in a three beam treatment, to the healthy spine, is 30 Gy. The maximum dose in a five beam treatment is only 25 Gy. These doses are low enough to satisfy the requirements as set by QUANTEC for a fractionated treatment. The maximum dose in the lungs for three beam and five beam treatments are 25 and 20 Gy, respectively. To reduce the risk of pneumonitis, according to QUANTEC, 35% of the lung volume should receive less than 20 Gy, which has been satisfied

by both preclinical treatment options. When we compare the mean dose in the target to the mean dose in our organ at risk, we find a ratio of 15% and 13% for a three beam and five beam irradiation, respectively.

H. Conclusions and future work

While it can be assumed that a preclinical orthovoltage treatment will not deliver an identical treatment to that in the clinic, based on the presented work, it can be indicated that a well designed small animal treatment can be clinically comparable, based on treatment results. A well designed treatment accounts for the differences in beam energy, subject size, and dose distribution, and the results indicate comparable treatment, not necessarily identical treatment.

According to the metric comparison and DVHs presented above, a three beam preclinical lung tumor irradiation can be performed with lower conformity but similar ratios of doses between the target and the organ at risk. Less conformity could be due to the higher dose around the target in the healthy lung tissue, based on the shallower orthovoltage dose fall off compared to a megavoltage dose fall off. A shallower dose fall off leads to higher doses after the target than seen in the clinic, which provides higher healthy tissue irradiation. However, the preclinical treatment was still able to limit the hotspot to an acceptable value and maintain low dose to the organ at risk, relative to the organ volume. A treatment with more beams would decrease the amount of dose in each beam, however, it would increase the area of healthy tissue receiving dose. Based on the comparison of three and five beams in the spinal irradiation, it can be shown that there is little to be gained from increasing the number of beams. In the lung irradiation case, with a sharp penumbra around each beam, a large volume of the heart can be spared with fewer beams with slightly higher doses, so this is the preferable treatment method.

A three beam preclinical brain irradiation yielded metrics that were quite clinically comparable. The conformity of a circular beam to a 0.5 mm^3 volume target was almost exactly the conformity seen in a clinical eight beam treatment. The preclinical hotspot was similarly low compared to the clinical value and the target coverage was almost as high. Based on the position of the tumor within the brain, the dose to the organ at risk was very low, less than 0.5% of the target dose. Based on these values, it can be concluded that a three beam orthovoltage treatment is sufficient to deliver a clinically comparable treatment, based on the very sharp penumbra of the beam as well as the image guided capabilities of some orthovoltage

irradiators which can provide highly repeatable positioning. It's unlikely that an increased number of beams would improve the treatment; in fact, it could end up providing higher doses to the healthy brain tissue, so it is prudent to utilize a three beam treatment.

The conformity and target coverage of a three beam liver irradiation were clinically comparable, with improved preclinical conformity when compared to a clinical treatment. However, there was a significantly higher hotspot in the liver, as well as a higher mean dose in the liver than seen in a clinical treatment. Because the orthovoltage dose fall off is so shallow, there is higher dose to tissues before and after the target. The liver is a very large organ, with a high volume of healthy tissue surrounding the target, which receives higher entrance and exit dose with respect to the target. In this scenario, with such a large target volume, treatment could be improved with more beams. A large volume of the liver is receiving dose in a three beam treatment. In a five beam treatment, each beam will contribute lower doses, but more volume will be irradiated. In a treatment such as the brain, so little volume is irradiated in a three beam treatment, it does not improve the results by spreading out the dose. However, in the liver irradiation, each beam is wide and already irradiating a large portion of the liver volume. Increasing the number of beams could decrease the overall liver dose by reducing each beam contribution.

A square beam, as typically seen in clinical treatments, was used to irradiate a spinal mouse tumor with both three and five beam treatments. The purpose of using two different treatments was to identify how, if at all, treatment can be improved with an increased number of beams. As shown in the results, there is little to be gained from additional beams. More beams will simply increase the time required to treat each small animal, thus prolonging the experiment. The only benefit of two additional beams was the decreased hot spot. In the case of spine treatment, it is important to reduce the maximum dose delivered to any small volume of the spine. However, the three beam hotspot is still clinically acceptable. The target coverage and conformity are acceptable with both beam options and little dose is delivered to the lungs, the organ at risk. The location of the spine tumor, in this scenario, was at the midline of the lungs and the heart, so the dose to the lungs is theoretically at the maximum value and the dose restrictions have still been met.

The scope of this project is extensive, and it will likely require years of experience and collaborative efforts to develop standardized preclinical small animal trials for radiation therapy testing. It is therefore important to break the process into steps. In this paper, we have presented the comparison of megavoltage and

orthovoltage irradiators and the ability of microirradiators to deliver clinically comparable treatment beams. We have also compared mice and humans in terms of organ volumes in an effort to develop scaling standards for treatment design. Finally, we have presented preliminary small animal treatments of the brain, lung, liver, and spine delivered to mouse phantoms and GafChromic film. The results of these treatments were characterized with clinical metrics, such as homogeneity, dose non uniformity ratio, and conformity index. DVHs were developed to compare the volumetric doses for the target and organs at risk. These results were compared to clinical treatment plans of the same treatment sites. The purpose of the comparison was to determine if the preclinical treatments were designed appropriately according to the initial scaling standard and orthovoltage beam characteristics. According to these preliminary comparisons, the designs are clinically relevant, but perhaps not yet entirely comparable.

There are aspects of preclinical orthovoltage irradiations that have not yet been taken into account, such as the orthovoltage radiobiological effectiveness (RBE) versus a megavoltage RBE. The question of RBE is still considered, even in the clinic, when comparing treatment beams such as photons and protons. We would like to see a study developed comparing the RBE of orthovoltage versus megavoltage, in order to more accurately design a preclinical trial, taking into account beam energy. Another factor which has not been explored in depth yet is the varying radiosensitivity of mice organs and human organs. QUANTEC data has been published outlining the radiosensitivity of human organs with respect to treatment sites. It cannot be assumed that mice organs have the same radiosensitivity, so it would be a worthwhile study to explore the doses of OAR for mice.

I. Acknowledgements

I would like to thank Dr. Yaddanapudi for his clinical input and Dr. Joshua Rubin's lab, at Washington University in St. Louis, for their time and effort in providing us with mice with gliomas.

J. References

- AMA. (2008). Physician characteristics and distribution in the US 2004 *IMV Medical Information Division*.
- Baumann, M., Bentzen, S. M., Doerr, W., Joiner, M. C., Saunders, M., Tannock, I. F., & Thames, H. D. (2001). The translational research chain: Is it delivering the goods? *Int. J. Radiation Oncology Biol. Phys.*, 49(2), 345-351.

- Bortfeld, T. (2006). IMRT: a review and preview. *Phys Med Bio*, 51, R363-R379.
- Cavanaugh, D., Johnson, E., Price, R. E., Kurie, J., Travis, E. L., & Cody, D. D. (2004). In vivo respiratory-gated micro-CT imaging in small animal oncology models. *Molecular Imaging*, 3(1), 55-62.
- Chen, C. P., Huang, K., & Roach, M. (2010). Hepatobiliary Cancer. In E. K. Hansen & M. Roach (Eds.), *Handbook of evidence-based radiation oncology* (Vol. 2). New York: Springer.
- Clarkson, R., Lindsay, P. E., Ansell, S., Wilson, G., Jelveh, S., Hill, R. P., & Jaffray, D. A. (2011). Characterization of image quality and image-guidance performance of a preclinical microirradiator. *Med Phys*, 38(2), 845-856.
- Curt, G. A. (1994). The use of animal models in cancer drug discovery and development. *Stem Cells*, 12, 23-29.
- Deng, H., Kennedy, C. W., Armour, E., Tryggestad, E., Ford, E., McNutt, T., . . . Wong, J. (2007). The small-animal radiation research platform (SARRP): dosimetry of a focused lens system. *Phys Med Bio*, 52, 2729-2740.
- DesRosiers, C., Mendonca, M. S., Tyree, C., Moskvina, V., Bank, M., Massaro, L., . . . Timmerman, R. (2003). Use of the Leksell Gamma Knife for localized small field lens irradiation in rodents. *Technology in Cancer Research and Treatment*, 2(5), 449-454.
- Duchting, W., Ulmer, W., & Ginsberg, T. (1998). *Cancer: A challenge for control theory and computer modeling*. Boca Raton, FL: CRC Press LLC.
- El-Deiry, W. S., Sigman, C. C., & Kelloff, G. J. (2006). Imaging and oncologic drug development. *Journal of Clinical Oncology*, 24(20), 3261-3273.
- Elekta. (2012). Leksell Coordinate Frame G Retrieved November 28, 2012
- Gafchromic. (2010). Gafchromic EBT2: Self developing film for radiotherapy dosimetry. Wayne, NJ: International Specialty Products.
- Gagliardi, G., Constine, L. S., Moiseenko, V., Correa, C., Pierce, L. J., Allen, A. M., & Marks, L. B. (2010). Radiation dose-volume effects in the heart. *Int. J. Radiation Oncology Biol. Phys.*, 76(3), S77-S85.
- Green, E. L. (1966). *Biology of the laboratory mouse* (Vol. 2). New York: Dover Publications.
- Herman, M. G., Balter, J. M., Jaffray, D. A., McGee, K. P., Munro, P., Shalev, S., . . . Wong, J. W. (2001). Clinical use of electronic portal imaging: Report of the AAPM radiation therapy committee task group 58. *Med Phys*, 28(5), 712-737.
- Izaguirre, E. W., Price, S. G., Su, I.-T., Birch, J., & Low, D. (2012). Implementation of a micro resolution dual gantry preclinical image guided microirradiator. *submitted to phys med bio*.
- Jabbari, S., Hansen, E. K., & Haas-Kogan, D. A. (2010). Non-small cell lung cancer. In E. K. Hansen & M. Roach (Eds.), *Handbook of evidence-based radiation oncology* (Vol. 2). New York: Springer.
- Jong, M. d., & Maina, T. (2010). Of mice and humans: Are they the same? - Implications in cancer translational research. *J Nucl Med*, 51(501-504).

- Kirkpatrick, J. P., Kogel, A. J. V. D., & Schultheiss, T. E. (2010). Radiation dose-volume effects in the spinal cord. *Int. J. Radiation Oncology Biol. Phys.*, 76(3), S42-S29.
- Lawrence, Y. R., Li, X. A., Naqa, I. E., Hahn, C. A., Marks, L. B., Merchant, T. E., & Dicker, A. P. (2010). Radiation dose-volume effects in the brain. *Int. J. Radiation Oncology Biol. Phys.*, 76(3), S20-S27.
- Ma, C.-M., Coffey, C. W., DeWerd, L. A., Liu, C., Nath, R., Seltzer, S. M., & Seuntjens, J. P. (2001). AAPM protocol for 4-300 kV x-ray beam dosimetry in radiotherapy and radiobiology. *Med Phys*, 28(6), 868-893.
- Maitz, A. H., Wu, A., Lunsford, L. D., Flickinger, J. C., Kondziolka, D., & Bloomer, W. D. (1995). Quality assurance for Gamme Knife stereotactic radiosurgery. *Int. J. Radiation Oncology Biol. Phys.*, 32(1465-1471).
- Marks, L. B., Bentzen, S. M., Deasy, J. O., Kong, F.-M. S., Bradley, J. D., Vogelius, I. S., . . . Jackson, A. (2010). Radiation dose-volume effects in the lung. *Int. J. Radiation Oncology Biol. Phys.*, 76(3), S70-S76.
- Moore, K. L. (2010). Washington University Brain Book: Department of Radiation Oncology, Barnes-Jewish Hospital.
- Mutic, S., Palta, J. R., Butker, E. K., Das, I. J., Huq, M. S., Loo, L.-N. D., . . . Dyk, J. V. (2003). Quality assurance for computed tomography simulators and the computed tomography simulation process: Report of the AAPM radiation therapy committee task group No. 66. *Med Phys*, 30(10), 2762-2792.
- Nath, R., Biggs, P. J., Bova, F. J., Ling, C. C., Purdy, J. A., Geijn, J. v. d., & Weinhaus, M. S. (1994). AAPM code of practice for radiotherapy accelerators: report of AAPM radiation therapy task group 45. *Med Phys*, 21(7), 1093-1121.
- NIH. (2012). ImageJ.
- Paddick, I. (2000). A simple scoring ratio to index the conformity of radiosurgical treatment plans. *J Neurosurg*, 93, 219-222.
- Pn, C. C., Kavanagh, B. D., Dawson, L. A., Li, X. A., Das, S. K., Miften, M., & Haken, R. K. T. (2012). Radiation-associated liver injury. *Int. J. Radiation Oncology Biol. Phys.*, 76(3), S94-S100.
- Pomper, M. G., & Lee, J. S. (2005). Small animal imaging in drug development. *Current Pharmaceutical Design*, 11, 3247-3272.
- Price, S. G., Silvius, A. A., & Izaguirre, E. W. (2012). A micro electronic portal imaging device for image guided conformal microirradiation of murine cancer models. *Submitted to Journal of X-Ray Science and Technology*.
- Regales, L., Balak, M. N., Gong, Y., Politi, K., Sawai, A., Le, C., . . . Pao, W. (2007). Development of new mouse lung tumor models expressing EGFR T790M mutants associated with clinical resistance to kinase inhibitors. *PLoS ONE*, 8(e810), 1-10.
- Saw, C. B., & Suntharalingam, N. (1990). Quantitative assessment of interstitial implants. *Int. J. Radiation Oncology Biol. Phys.*, 20, 135-139.
- Schulz, M. D. (1975). The supervoltage story. *The American Journal of Roentgenology*, 124(4), 541-559.

- Sharpless, N. E., & DePinho, R. A. (2006). The mighty mouse: genetically engineered mouse models in cancer drug development. *Nature Reviews Drug Discovery*, 5, 741-754.
- Sherwood, L. (2006). *Fundamentals of Physiology: A human perspective*. Belmont, CA: Thomson Brooks/Cole.
- Soderstrom, S., & Brahme, A. (1995). Which is the most suitable number of photon beam portals in coplanar radiation therapy. *Int. J. Radiation Oncology Biol. Phys.*, 33(1), 151-159.
- Stein, J., Mohan, R., Wang, X.-H., Bortfeld, T., Wu, Q., Preiser, K., . . . Schlegel, W. (1996). Number and orientations of beams in intensity-modulated radiation treatments. *Med Phys*, 24(2), 149-160.
- Stojadinovic, S., Low, D. A., Hope, A. J., Vicic, M., Deasy, J. O., Cui, J., . . . Grigsby, P. W. (2007). MicroRT - Small animal conformal irradiator. *Med Phys*, 34(12), 4706-4716.
- Taghian, A. G., & Suit, H. D. (1999). Animal systems for translational research in radiation oncology. *Acta Oncologica*, 38(7), 829-838.
- Trilogy. (2012). Millenium MLC Retrieved November 1, 2012, from www.varian.com/us/oncology/radiation_oncology/trilogy/millenium_mlc.html
- Verhaegen, F., Granton, P., & Tryggestad, E. (2011). Small animal radiotherapy research platforms. *Phys Med Bio*, 56, R55-R83.
- Withers, H. R. (1985). Biologic basis for altered fractionation schemes. *Cancer*, 55, 2086-2095.
- Wong, J., Armour, E., Kazanzides, P., Iordachita, I., Tryggestad, E., Deng, H., . . . DeWeese, T. L. (2008). High resolution small animal radiation research platform with x-ray tomographic guidance capabilities. *Int. J. Radiation Oncology Biol. Phys.*, 71(5), 1591-1599.
- Xia, P., Geis, P., Xing, L., Ma, C., Findley, D., Forster, K., & Boyer, A. (1999). Physical characteristics of a miniature multileaf collimator. *Med Phys*, 26(1), 65-70.
- Yoo, S., Grimm, D., Zhu, R., Jursinic, P., Lopez, F., Rownd, J., & Gillin, M. (2002). Clinical implementation of AAPM TG61 protocol for kilovoltage x-ray beam dosimetry. *Med Phys*, 29(10), 2269-2273.
- Zwicker, R. D., & Schmidt-Ullrich, R. (1995). Dose uniformity in a planar interstitial implant system. *Int. J. Radiation Oncology Biol. Phys.*, 31(1), 149-155.

4. INSTRUMENTATION AND TECHNIQUES FOR ORTHOVOLTAGE MICRODOSIMETRY USING SCINTILLATING FIBERS

A. Introduction

Beddar et al (1992) described the use of water equivalent plastic scintillation dosimeters for use with megavoltage beams. Results were presented for clinical photon beams between 4 and 18 MV and electron beams between 6 and 18 MeV. His group concluded that the dosimeter has excellent reproducibility and stability at megavoltage energies, are dose rate independent, and respond linearly with dose. His group provided an effective, high resolution option for clinical dosimetry using scintillating fibers. With the expanding use of preclinical small animal trials, it is advantageous to translate this technology for use in orthovoltage irradiators. Small animals are currently utilized in preclinical radiation therapy trials to provide clinically relevant results for testing novel drugs and radiation therapy techniques and devices. The purpose of a preclinical trial is to test radiation therapy devices and techniques which will eventually be used in the clinic. If a small animal trial cannot produce the same level of precision as a clinical treatment, with respect to treatment subject size, then the small animal trial will not produce results which can be translated appropriately. In an instance when the preclinical trial is not clinically relevant, a novel radiotherapy technique could be successful in a preclinical trial, but fail in a clinical trial, thus leading to a loss of time and money for a failed method. However, if the small animal trial is designed appropriately, the small animal results will reflect future clinical results, thus leading to earlier conclusions on the efficacy of a radiotherapy technique.

Hypofractionation is currently used in the clinic for some treatment sites, such as the brain, in combination with stereotactic therapy (Herfarth, 2006). The ability to deliver an effective hypofractionated treatment stems from the improved treatment localization currently seen in the clinic. In a typical fractionated schedule, a low dose is delivered daily to the tumor for several weeks, until the maximum dose is delivered. Because healthy tissue will heal more quickly than a tumor, this fractionated schedule allows the irradiated healthy tissue to repair while still killing the tumor (Withers, 1985). In a hypofractionated stereotactic treatment, a higher dose is delivered each fraction. If a large volume of healthy tissue is irradiated, it could lead to damage too extensive to repair. To reduce this risk, the volume of irradiated healthy tissue should

be minimized as much as possible through improved target localization. This improved localization is due to very high resolution pre-treatment imaging, high precision image guided radiation therapy, and well characterized small fields. High resolution diagnostic imaging provides dosimetrists high quality images on which to delineate the target very precisely. The next step in providing hypofractionated treatment is the use of a highly precise delivery system, with small penumbra relative to the target and precise subject and treatment beam positioning. An image guidance system can provide imaging before and during at treatment to verify the patient and treatment beam have been positioned according to the treatment plan. Each of these factors will culminate in a highly precise and very localized treatment beam which will deliver a high radiation dose to the target while sparing surrounding tissues. Finally, to deliver a highly precise treatment, it is important to know the distribution of dose within a small field size so it can be accurately modeled in the treatment planning system for a predictable and stable treatment.

In order to further develop novel hypofractionated treatments, a small animal model must be developed for preclinical trials. A clinical hypofractionated treatment delivery device is the Gamma Knife, which can offer collimators for 4, 8, and 16 mm diameter treatment beams, which are some of the smallest clinical treatment field sizes (Mack et al., 2002). If we consider the optic nerve in a mouse, it can be assumed to be one of the smallest structures to be targeted in the brain for irradiation, and the typical width of the optic nerve is approximately 300 μm (Mabuchi et al., 2004). This treatment field size is significantly smaller than the treatment beam offered by Gamma Knife, so clinical dosimetry devices may not be capable of providing accurate dosimetry for these small field sizes.

To deliver this treatment, an orthovoltage device must provide a beam with a small penumbra which can be targeted precisely and verified with image guidance systems. The treatment beam must also be well characterized in order to provide accurate treatment planning. A clinical treatment plan is developed using parameters inputted from a specific treatment machine. These parameters include the shape of the beam for varying field sizes and provide appropriate dose distributions. When considering a small animal treatment, the resolution required to characterize the beam distribution will need to be on a submillimeter scale for accurate treatment, based on small animal organ volumes and penumbra widths. To determine these parameters, there should be a system in place that provides dosimetry with high spatial resolution. The

ideal dosimeter would be tissue equivalent so as to not perturb the beam and provide accurate dosimetry at a wide range of energy levels, from 10 kVp to 320 kVp.

One option which provides absolute dosimetry is an ion chamber. Ion chambers come in many sizes, with recommended field sizes as small as $6 \times 8 \text{ mm}^2$ (Exradin Ion Chambers, 2012), and can provide good spatial resolution at a wide range of energies. Ion chambers have the advantage of precision when the requirements, such as charged particle equilibrium, are met. Based on the small fields required for microdosimetry, these requirements may not necessarily be met and the ion chamber will not function as designed. Ion chambers contain an air cavity, which can perturb attenuation and scatter the beam, which contradicts the requirements of the Bragg-Gray cavity theory [Attix, 1986]. According to the theory, the primary radiation field must not be perturbed, so ion chambers will not operate correctly in very small field sizes. In addition, there will be a single charge value collected over the collecting volume, thus limiting the resolution to the collecting volume size.

Another dosimetry option is radiochromic or radiographic film. Radiographic film is not an ideal option for orthovoltage dosimetry due to the high Z silver content. These films tend to over respond at low energies due to photoelectric interactions. Based on the high Z content, radiographic film is not tissue equivalent, so it is not necessarily useful for absorbed dose measurements. Radiochromic film, on the other hand, uses a gel component which responds to photon interactions and darkens when exposed. It has the advantage that it is mostly insensitive to ambient light and does not require developing. It is also nearly tissue equivalent, with a Z_{eff} of 6.98, compared to the Z_{eff} of water of 7.3 (Martiskova, Ackermann, & Jakel, 2008). Radiochromic film is nearly energy independent from 50 keV to the MV range, which makes it useful when comparing orthovoltage and megavoltage irradiations. Radiochromic film can be calibrated using a known dose gradient and a single batch of film when absolute dosimetry is required, but typically film is used for relative measurements. One disadvantage of film is the inability to read out dosimetry data in real time. Even though radiochromic film does not require post exposure processing, it can only be viewed after it has been exposed. This has the possibility for a loss of positioning information and, for absolute measurements, requires approximately 24 hours to reach a stable exposure before it can be read with a scanner. When digitizing the film into a scanner, the directionality of the film is very important, both during exposure and read out. This uncertainty can arise in the use of different film batches, the stability of the scanner, and the

effectiveness of the calibration (Martisikova et al., 2008). Radiochromic film is the gold standard for measuring beam profiles and dose distributions, based on the high resolution it offers. The resolution is typically limited to the maximum resolution of the scanning device, rather than by the film itself. While film is not a good option for real time dosimetry or absolute dosimetry, it is an excellent method for evaluating the effectiveness of other dosimeters.

Diodes can be an excellent dosimeter in small fields, with field size independence from $1 \times 1 \text{ cm}^2$ up to $40 \times 40 \text{ cm}^2$; however, they show an energy dependence and possible directional dependence. Below 1 MeV, the correction factor is no longer close to 1, as it is for energies greater than 1 MeV, so it is difficult to correct for energy. This will limit the energies for which the diode can be used as well as introduce uncertainties if the directionality is not consistent.

Thermoluminescent dosimeters (TLD) are also good for small fields and available in a wide range of forms, such as chips and powders. The advantage of TLDs is not only the range of forms, but also the range of materials from which a dosimeter can be constructed. There are currently TLDs available which are tissue equivalent in the orthovoltage range as well as those that are tissue equivalent in the megavoltage range [Furetta, et al, 2001; Mobit, et al, 1995]. The disadvantage of TLDs is that they suffer from statistical uncertainties, similar to those seen in film.

Based on the disadvantages of current clinic dosimeters when applied to small field orthovoltage dosimetry, we have chosen to perform microdosimetry with the use of scintillating fibers. Table 10 summarizes the commonly used dosimeters, with their parameters compared side by side. Scintillating fibers are water and tissue equivalent. This ensures very little perturbation of the beam, as well as a direct method of dose calculation, as opposed to converting from one medium to another. Organic scintillators have been shown to produce a high number of light photons per x-ray emitted, and tend to respond linearly with energy, down to 100 keV. Below 100 keV, the scintillation efficiency drops, but can be accounted for with proper calibration [Beddar et al, 1992]. Scintillating fibers can provide high resolution dosimetry with real time data acquisition and read out, and they can be as narrow as $200 \mu\text{m}$ (Saint-Gobain, 2005), thus providing dose profile measurement on small animal organ substructure scales. We have built and tested a scintillating fiber dosimeter with two different scintillating elements. The results of the scintillating

dosimeter have been compared with radiochromic film, as the gold standard, and ion chambers, as the clinical option.

Table 10. Comparison of commonly used dosimeters for small fields

	Minimum Active Detector Size [cm ²]	Absolute Dosimetry	Direction Dependent	Energy Dependent	Real Time Readout	Limitations
Ion Chamber	0.5x0.5	yes	no	yes	yes	Field perturbation, limited resolution
Liquid Filled Ion Chamber	0.5x0.5	yes	no	yes	yes	Limited resolution
Diode	1x1	no	yes	yes	yes	Thermal effects and radiation induced damage
TLD	0.3x0.3	no	no	yes	no	Susceptible to fading
MOSFET	0.02x0.02	no	yes	yes	yes	Temperature and dose rate dependence
OSLD	0.02x0.02	no	yes	yes	no	Temperature and dose rate dependence and fading
Radiochromic Film	NA	no	yes	no	no	24 hour wait time for scanning and read out
Organic Scintillator	0.02x0.02	no	no	no	yes	Must account for Cerenkov in the MV range

B. Methods

i. Detector components

Figure 32 indicates the components of the dosimeter, including the scintillating element, optical fiber, photodiode, electronics, and power supply cables. To read the light output of the scintillating element, we chose to use a multi pixel photon counter (MPPC) as opposed to a PMT based on the small electronics and ease of use offered by a photodiode. A PMT offers high gain, which is desirable in this experimental set up, but the same level of gain can be achieved through the use of a photodiode and an amplifier. The MPPC we chose to use is a Hamamatsu SMD type MPPC [Hamamatsu, Hamamatsu City, Japan]. This device has an active area of 1x1 mm² with 50x50 μm² pixel size. Based on the high resolution of the MPPC, it was ideal

for our detector. The MPPC was coupled to the optical fiber with epoxy and coated with black paint. The efficiencies of the MPPC and the fluorescence output of the scintillating fibers are shown in figure 33.

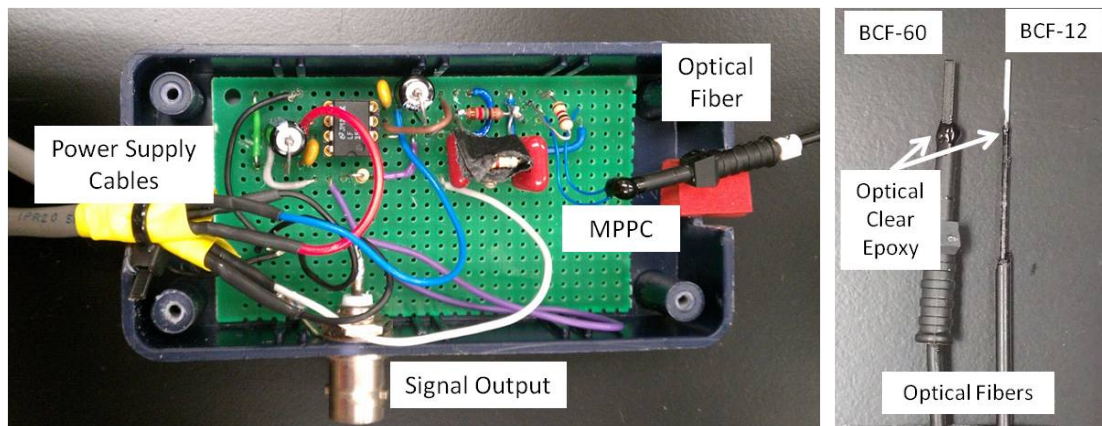


Figure 32. Left: Dosimeter electronics. Optical fiber has been epoxied to the MPPC diode and coated with black paint. Right: Two scintillating fibers, BCF-12 and BCF-60, coupled to clear fibers with optical clear epoxy, painted black.

Because the scintillating element is small, an amplifier with a gain of 10 was used to increase the signal from the few photons produced. The gain of the MPPC itself is 10^5 - 10^6 . An amplifier followed the photodiode, and this amplified signal was read with a Tektronix TDS 2022B oscilloscope (Tektronix, Beaverton, OR) and a Keithley 160 digital micro voltmeter (Keithley, Cleveland, OH). All of the electronics were placed in a light tight box, with small openings for the incoming fiber and outgoing cables for power. The signal was read out through a BNC connector on the light tight box, shown in figure 32.

To determine the optimum scintillating fiber set up, two scintillating fibers were chosen based on their sizes and light output. A 1500 μm thick square BCF-60 fiber was tested based on the larger size and hence larger photon output. The blue light output from the BCF-60 is not necessarily ideal for our photodiode, but the large scintillating element allowed for a greater number of photons to be produced and the emission wavelength was within the photodiode's input range. The second fiber was a 500 μm thick square BCF-12 fiber. The more narrow fiber should provide higher resolution in small fields, but will produce fewer photons. The light output of the BCF-12 is better matched for the MPPC chosen, as shown in figure 33. Both fibers were 1 cm long. The parameters of the fibers are compared in table 11.

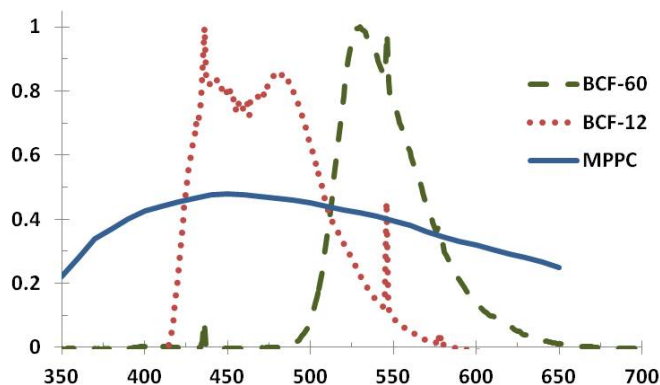


Figure 33. Efficiency curves for BCF-12 (dotted red line), BCF-60 (dashed green line), and the MPPC (solid blue line).

The scintillating fibers have a polystyrene core with acrylic cladding of 0.06 mm. The fibers were coated with black paint to reduce ambient light pollution and were first tested with UV light and orthovoltage irradiation to verify the output wavelength. The output light was read with a B&WTEK CCD array spectrometer (BWTEK, Newark, DE) and compared with the scintillating fiber manufacturer's specifications. The following equations were applied for both scintillating fibers, but only the BCF-60 fiber is demonstrated here.

Table 11. Comparison of fiber parameters

	BCF-12	BCF-60
Sensitivity [mV/V]	364.5	730
Signal to noise ratio	145	80
Polarization [v]	72.5	72.5
Spectral peak [nm]	435	530
Spectral width [nm]	56.5	50.8
Photons per MeV	8000	7100
Attenuation length	2.7	3.5
Photons/second incident on MPPC	$5.252 \cdot 10^4$	$2.606 \cdot 10^6$

A $1.5 \times 1.5 \times 10 \text{ mm}^3$ rectangular box was cut from a fiber and polished with 1, 3, and 5 μm grit size aluminum oxide polishing sheets. (ThorLabs, Newton, NJ). The scintillating element was adhered with optical clear epoxy to a clear optical fiber of the same diameter, measuring 2 m in length. The BCF-60 fiber, as quoted by the manufacturer, produced 7.1 photons per keV of incident beam. For a 300 kVp beam passing through a Thoreau's filter, the average energy is 189 keV (Izaguirre, Price, Su, Birch, & Low, 2012). This treatment beam will then result in 1,512 photons per particle. For a flux of $3.884 \cdot 10^{10}$

/cm²second, as measured with a CC04 ion chamber and a silicon diode, 5.826×10^9 particles/second will be incident on the $1.5 \times 1.5 \times 10$ mm² scintillating element. Therefore, the scintillating element will theoretically produce 7.818×10^{12} fluorescence photons/second. However, not all of the x-rays will be stopped in the fiber, so we can use the attenuation of the material to find the actual number of photons will be absorbed in the fiber. In addition, fluorescence photons will only be produced due to the doping material in the acrylic fiber. The linear attenuation coefficient of the fiber is 0.161 at the average energy of 189 keV, and using equation 3, we can find the ratio of photons stopped in the fiber to the total number of photons.

$$\eta = 1 - e^{-\mu x} \quad 3$$

x is the thickness of the fiber, and we find η to be 0.003. Taking into account that the fiber is 0.1% doping material, we find that the BCF-60 fiber is in fact producing 1.87×10^8 photons/sec. Based on the inherent properties of the scintillating element, there will be a loss in photons based on the refractive indices of the fiber. The scintillating fiber element, with a polystyrene core and acrylic cladding, will have respective refractive indices of $n_f=1.68$ and $n_c=1.49$. According to Snell's law in equation 4, the critical angle can be found with

$$n_f \sin(\theta_c) = n_c. \quad 4$$

The critical emission angle by total reflection is shown in equation 5.

$$\xi_c = \frac{\pi}{2} - \theta_c. \quad 5$$

Therefore, using these equations, we find equation 6.

$$\cos(\xi_c) = \sin(\theta_c) = \frac{n_c}{n_f}. \quad 6$$

To find the fraction of photons exiting the fiber through one uncoated end, the efficiency of the fiber, we use equation 7.

$$\varepsilon_a = \frac{1}{4\pi} \int_{\cos \xi_c}^1 d\Omega. \quad 7$$

After we integrate equation 7, we acquire equation 8.

$$\varepsilon_a = \frac{1}{2} \left(1 - \frac{n_c}{n_f}\right). \quad 8$$

Using the refractive indices for polystyrene and acrylic, we find the scintillating fiber trapping efficiency to be 0.057. In addition to a loss in photons due to inherent efficiency, there will be attenuation of the photons

through the scintillating fiber, though it will not contribute greatly due to the small element size. Equation 9 is used to determine the transmission of photons through a fiber.

$$T \cong e^{-x/L} \quad 9$$

T is the transmission, x is the length of the fiber, and L is the attenuation length. The attenuation lengths for both fibers are shown in table 11. Using this equation, we found the transmission to be 98.6% for the 1 cm long BCF-60 fiber. The optical fiber has an attenuation length in the scale of km, so based on this, it can be assumed there will be negligible attenuation through the 2 m fiber. According to Beddar et al (1992), we can assume the coupling efficiency to be 0.5 for both scintillating element-fiber and fiber-MPPC. The total efficiency of the entire scintillating element and fiber is shown in equation 10.

$$\varepsilon = \varepsilon_a \varepsilon_1 \varepsilon_2 T \quad 10$$

where $\varepsilon_1 = \varepsilon_2 = 0.5$ for the coupling efficiency. Finally, the total efficiency is found to be 0.014. If we apply this to our earlier photon flux, we find the total number of photons reaching the MPPC counter to be 1.09×10^{11} photons/second for our BCF-60 fiber (Rego, Abreu, & Peralta, 2011).

ii. *Experimental set up*

The microIGRT was used to deliver orthovoltage small animal treatments. The scintillating fiber was embedded in acrylic, for consistent back scatter, and placed at the mouse bed level in the microRT. The optical fiber was outside of the acrylic, and was guided through the mouse bed opening in the microRT shielding to the electronics outside. The electronics were attached to a $\pm 12V$ power supply for the amplifier, a high voltage power supply for the photodiode, and an oscilloscope and micro voltmeter for signal readout. The electronics and 12V power supply were located inside the lead lined room, outside of the microRT shielding. The high voltage power supply, the micro voltmeter, and the oscilloscope were located outside of the lead lined room, so they could be adjusted accordingly for appropriate dosimeter operation and read out. A schematic view is shown in figure 34.

The amplified signal can be digitized by a computer for a more precise readout, but for preliminary testing, the oscilloscope and micro voltmeter were sufficient. The micro voltmeter values were inputted into MathCAD for processing.

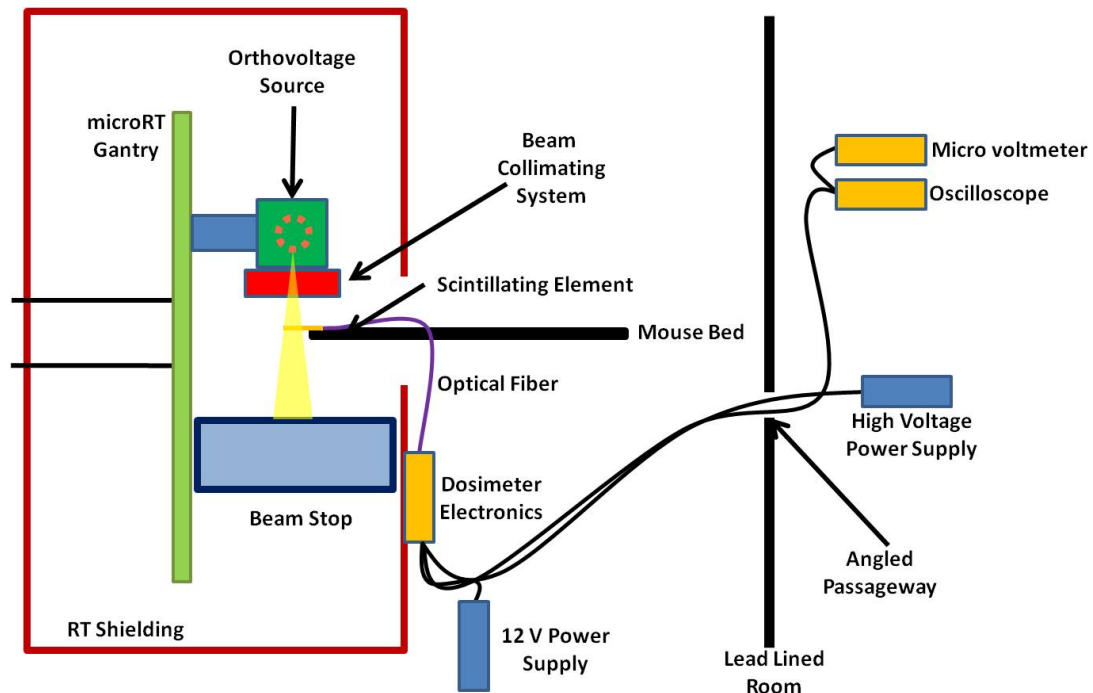


Figure 34. Schematic view of the experimental set up. The bold black line indicates the exterior wall of the lead lined room. An angled hole, a maze, through the wall allows for the passage of cables without the risk of radiation exposure.

iii. *Beam profile testing*

In order to determine the optimal polarization for the MPPC, the diode response was measured versus polarization for both scintillating fibers. Diode response was read with a micro voltmeter in mV and the polarization was measured in increments of 0.1 V from 68 V to 73 V.

The dosimeter response was first tested as a function of depth. Increasing thicknesses of acrylic were positioned over the fiber to test the scintillating output with respect to fiber depth in material. The fiber embedded in 4 mm of acrylic was placed at the isocenter of the microRT, 38 cm from the source, at the level of the mouse bed. A 5 mm circular aperture was in place, with the fiber at the center of circular beam. This percent depth dose (PDD) result was compared to CC01 and CC04 ion chamber responses (Scanditronix & Wellhoffer, 2012) and GafChromic film (GafChromic, 2010). The PDD was evaluated for a filtered beam at 300 kVp, the typical treatment energy. Thoreau's filters consisting of aluminum, copper, and tin were placed in the beam path for the filtered measurements. The ion chamber was placed in a 25 mm diameter phantom at three locations within the phantom, at $\frac{1}{4}$, $\frac{1}{2}$, and $\frac{3}{4}$ of the total depth. The relative measurements of the film and fiber were adjusted to the absolute measurements of the ion chamber. The

ion chamber charge was read by a K602 precision electrometer in nC (CNMC, 2012). For the ion chamber and fiber measurements, the source to dosimeter distance was constant, with additional acrylic added towards the beam. Due to the limited resolution of the ion chamber, radiochromic film was used to evaluate the shape of the PDD and then normalized to the absolute ion chamber values. 10 pieces of GafChromic film were placed between identical thicknesses of acrylic to form a 25 mm thick cylindrical phantom. The phantom was placed in the mouse bed and irradiated for 4 Gy with a 10 mm circular aperture. The film was scanned and analyzed to determine the beam profile. The fiber response profile was then compared to the ion chamber and film profile responses.

The dosimeter response was also tested as a function of beam size. In order to determine the scintillating fibers' improvement over ion chambers typically used in the clinic, we measured the beam profiles with the CC04 and CC01 ion chambers, as well as with the two scintillating fibers. The CC04 ion chamber has an active diameter of 4 mm and the CC01 ion chamber has an active diameter of 1 mm. The scintillating fibers and ion chambers were placed at the center of 1x1, 2x2, 5x5, and 10x10 mm² beams and imaged with the portal camera for positioning verification, as shown in figure 35. The largest beam size, 10x10 mm², was chosen to demonstrate the effectiveness of the CC04 ion chamber at larger field sizes. This ion chamber is considered to be the work horse of the clinic, as it the most commonly used ion chamber. This large field size is not typical in small animal irradiations. Each field size was chosen to accentuate the effectiveness of each dosimeter chosen. For instance, the CC04 ion chamber is too large for the two smaller field sizes, so it was not tested. Special care was taken to ensure that the dosimeter and the edge of the beam were parallel. Based on the pixel size of the portal camera, the precision of the set up angle between the fiber and the field can be considered to be 100 μm.

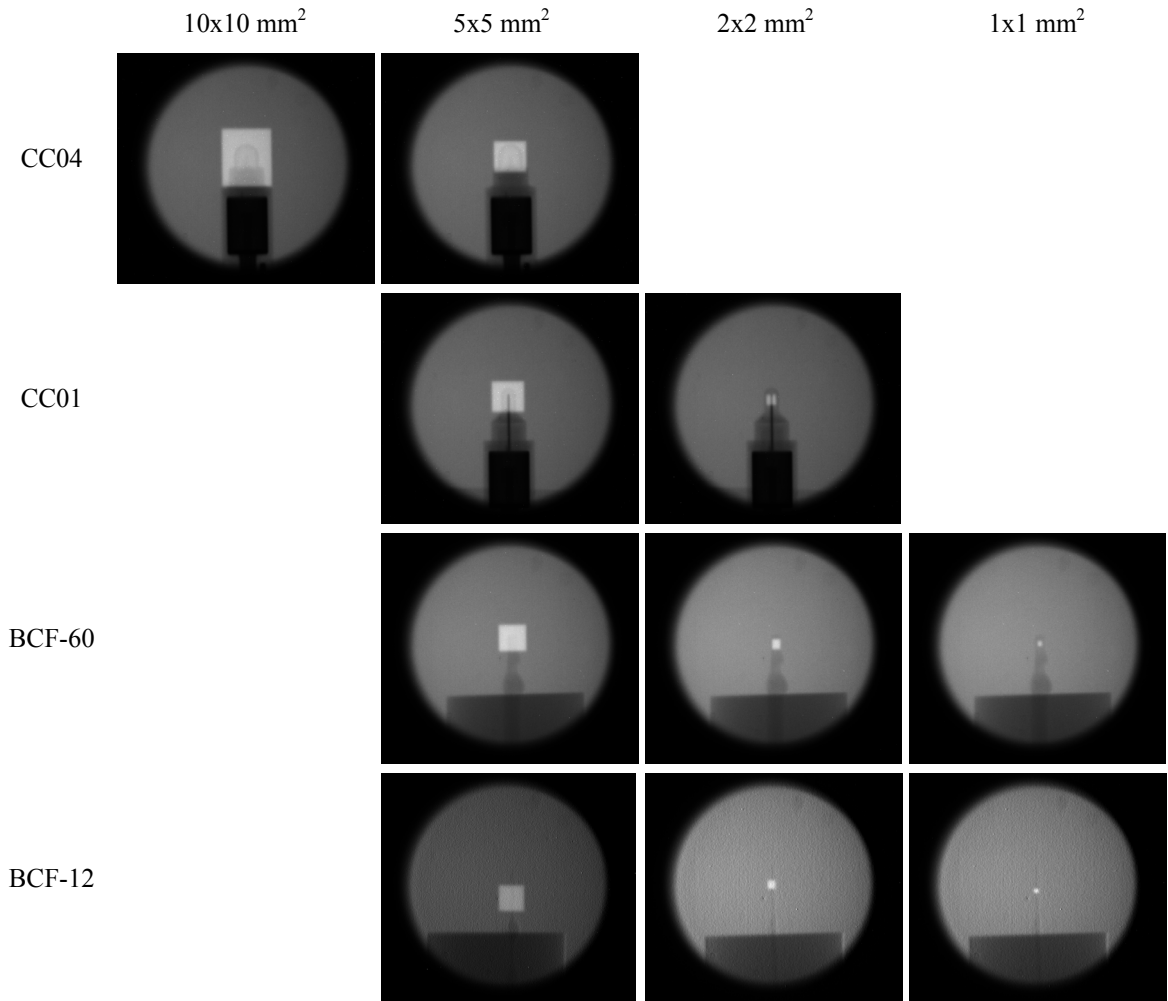


Figure 35. Left: Portal images of dosimeter overlaid with field size images. The fibers and ion chambers are attached to an acrylic half cylinder phantom and placed in the mouse bed, extending past the end to avoid backscatter error. The beam is centered on the dosimeters. A shadow feature has been added to enhance viewing on the BCF-12 500 μm fiber.

To determine the beam profile, the scintillating element was scanned across the beam using the mouse bed. The element was secured to an acrylic board placed on the mouse bed, attached to a half circle of acrylic to fit securely in the mouse bed for rigidity and repeatability. The mouse bed, as reported previously, can be moved in 50 μm increments with 2% error. The scintillating element was placed at the center line of the beam in the transverse direction, with the 10 mm length perpendicular to the direction of travel, and scanned across the entirety of the beam in 50 μm increments, with a 1 mm addition on each side of the beam circle to measure penumbra. The purpose of scanning the scintillating element is to reduce the total size of the dosimetry device required as well as improve the resolution greater than the finite size of the element. For comparison to clinical methods, the CC01 and CC04 ion chambers were positioned at the

same level as the fiber in subsequent irradiations. The ion chamber was then scanned across the beam profile and the output recorded. Finally, GafChromic film was used to measure the beam profile and act as the gold standard of measurement, with the highest resolution available.

The dose rate was measured with the dosimeter by varying the current of the beam. The fiber, embedded in acrylic, was placed at isocenter in a 5 mm circular beam. A constant 300 kVp filtered beam was delivered, with currents ranging from 1-5.7 mA. These beam settings correspond to dose rates between 5 and 50 cGy/min, as measured with a calibrated ion chamber. This experiment was repeated for the 120 kVp beam, used for imaging, with currents ranging from 0.5-5 mA.

To determine the repeatability of the measurements, the embedded fiber was placed at the isocenter for the beam every day and irradiated with the same beam energy, filter, and aperture size. The micro voltmeter values were read out each day and recorded to determine the variance. This was repeated for 20 days, to simulate a fractionated treatment.

C. Results

According to the diode curves acquired for both the 500 μm BCF-12 fiber and the 1500 μm BCF-60 fiber, shown in figure 36, the most effective polarization voltage was found to be 72.5 V. This value was chosen to provide a compromise between maximum gain and minimum noise.

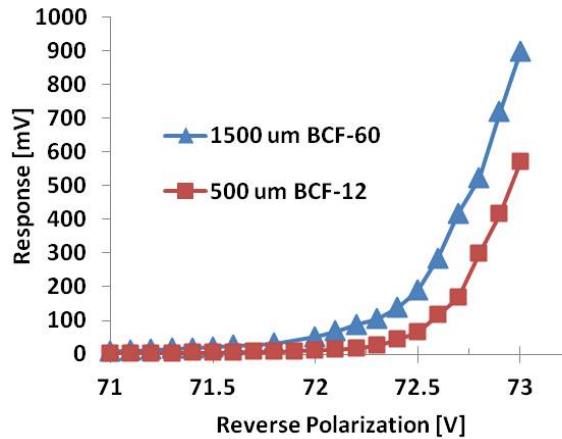


Figure 36. Diode response curves for the 500 μm BCF-12 fiber and the 1500 μm BCF-60 fiber.

The PDD of an orthovoltage beam was evaluated and compared with ion chamber measurements. The results are plotted in figure 37 for a total depth of 25 mm, considering the average diameter of a mouse as

the standard depth. The results indicate that the fiber, film, and ion chamber response are well matched. Based on the limited spatial resolution of the ion chamber, there are only three points of measurement along the PDD in a 25 mm depth. The GafChromic film was measured every 25 mm in a phantom with acrylic between each piece of film. The fiber response was read at 5 points, with 4 mm of acrylic added between each measurement. The deviation between the BCF-60 fiber and film measurements is 0.6% on average, and the deviation between the BCF-12 fiber and film measurements is 3.2%, on average.

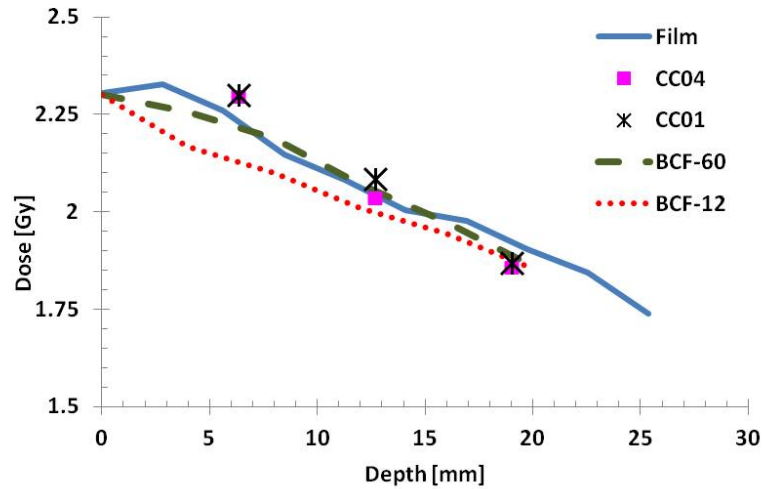


Figure 37. Dose as a function of depth as measured by GafChromic film (solid blue line), the BCF-60 fiber (dashed green line), BCF-12 fiber (dotted red line), a CC04 ion chamber (pink squares), and a CC01 ion chamber (black stars). Both the film and the fiber responses were relative and normalized to the ion chamber responses.

The beam profile results are shown in figure 38 for 1x1, 2x2, 5x5, and 10x10 mm² beams. The penumbra was measured as the distance between the 20% and 80% fall off the beam. The beam profiles are shown for GafChromic film and for the two ion chambers and two scintillating fibers, as explained in the methods. The values for the FWHM and the penumbra for each beam are shown in tables 12-15 for GafChromic film, the two ion chambers, and the scintillating fibers. Table 16 lists the deviations of the FWHM values for each dosimeter from the GafChromic film measurements. The values shown in the table were measured as shown in equation 10.

$$\frac{FWHM_{dosimeter} - FWHM_{film}}{FWHM_{film}} \quad 10$$

Table 17 lists the deviations of the penumbra for each dosimeter and each field size, using equation 10 for the penumbra, rather than the FWHM.

Table 12. Comparison of FWHM and penumbra for a 1x1 mm² beam detected with GafChromic film and the microdosimeter with a BCF-12 and BCF-60 fiber.

	Film	BCF-12	BCF-60
FWHM [mm]	1.23	1.274	1.30
Penumbra [mm]	0.291	0.283	0.689

Table 13. Comparison of FWHM and penumbra for a 2x2 mm² beam detected with GafChromic film, a CC01 ion chamber, and the microdosimeter with a BCF-12 and BCF-60 fiber.

	Film	BCF-12	BCF-60	CC01
FWHM [mm]	1.97	1.9	1.96	1.90
Penumbra [mm]	0.316	0.485	0.853	0.890

Table 14. Comparison of FWHM and penumbra for a 5x5 mm² beam detected with GafChromic film, a CC01 ion chamber, a CC04 ion chamber, and the microdosimeter with a BCF-60 fiber.

	Film	BCF-12	BCF-60	CC01	CC04
FWHM [mm]	5.29	5.09	5.30	5.20	5.35
Penumbra [mm]	0.416	0.279	0.888	1.025	2.43

Table 15. Comparison of FWHM and penumbra for a 10x10 mm² beam detected with GafChromic film and a CC04 ion chamber.

	Film	CC04
FWHM [mm]	11.44	12.39
Penumbra [mm]	0.366	2.636

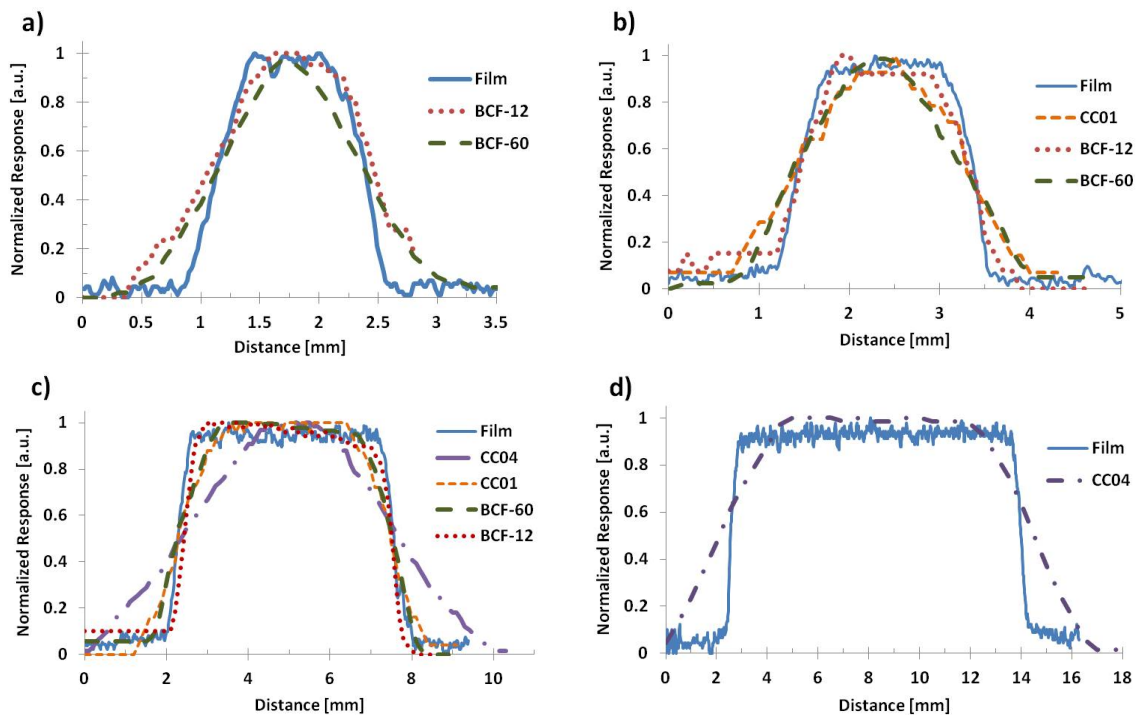


Figure 38. Beam profiles measured with GafChromic film (solid blue), CC04 ion chamber (dot-dash purple), CC01 ion chamber (short dashed orange), BCF-12 (dotted red) and BCF-60 (long dashed green). a) 1x1 mm² beam. b) 2x2 mm² beam. c) 5x5 mm² beam. d) 10x10 mm² beam.

Table 16. Comparison of the FWHM deviation from GafChromic film measurements for four field sizes and four dosimeters. Values are shown in percent.

Field Size [mm ²]	BCF-12	BCF-60	CC01	CC04
1x1	3.50	5.50	N/A	N/A
2x2	3.60	0.38	3.60	N/A
5x5	3.70	0.12	1.68	1.16
10x10	N/A	N/A	N/A	8.00

Table 17. Comparison of the penumbra deviation from GafChromic film measurements for four field sizes and four dosimeters. Values are shown in percents.

Field Size [mm ²]	BCF-12	BCF-60	CC01	CC04
1x1	2.70	136.00	N/A	N/A
2x2	53.00	169.00	181.00	N/A
5x5	32.82	113.70	146.67	484.80
10x10	N/A	N/A	N/A	620.00

The dose rate measurements for 120 kVp and 300 kVp are plotted in figure 39 for both the scintillating fibers to illustrate linear response with dose. The fiber output has been normalized to the maximum value.

The BCF-12 fiber shows a slight non-linear response to dose at the 120 kVp energy, with a deviation from the BCF-60 fiber of 5% at 0.5 mA. This non-linear response is most likely due to very low fluorescence photon production of the small BCF-12 fiber at lower currents.

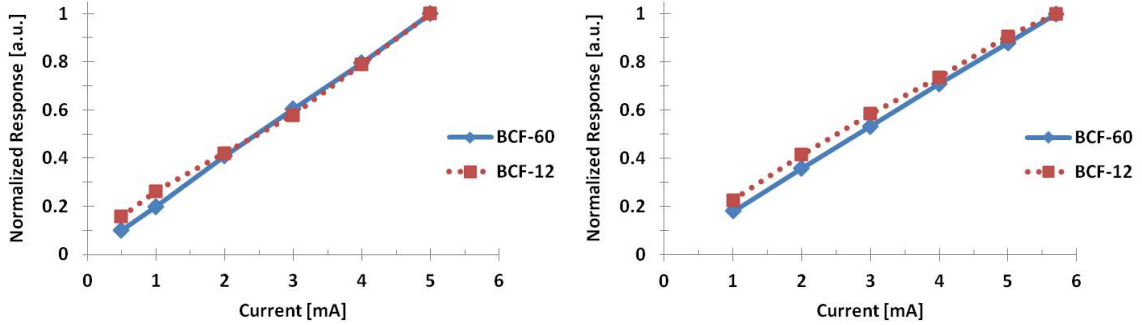


Figure 39. Left: Dose rate response of the BCF-12 (red dotted line) and BCF-60 (solid blue line) scintillating fibers for a 120 kVp beam and currents between 0.5 and 5 mA. Right: Dose rate response of the BCF-12 (red dotted line) and BCF-60 (solid blue line) scintillating fibers for a 300 kVp beam and currents between 1 and 5.7 mA.

Repeatability results assessed over 20 days to simulate a 40 Gy fractionated schedule show an average 6.5% deviation and a maximum 20% deviation. This daily deviation is most likely due to the fluctuation in the temperature of the room, as well as the exact positioning of the polarization dial. At the high gains, as seen in the diode curves, at the polarization voltage we are using, even a very small discrepancy in supply voltage will lead to large differences in response.

D. Conclusions

The clinical applications of scintillating fiber technology have been explored extensively and used with great success in megavoltage beams. Through the application of this technology in orthovoltage beams, we can improve preclinical dosimetry with low cost and hassle. In this work, we compared the response of two scintillating fibers with an MPPC photodiode to ion chambers and GafChromic film. This work has demonstrated high spatial resolution and dose linearity response of the fiber dosimeter, with basic electronics. It is clear that the scintillating fibers are much better suited for small field dosimetry than ion chambers, and can come close to the high resolution results of GafChromic film. Of the two fibers, the BCF-12 response was sufficiently high enough, despite its small size, to conclude that it is the superior option for small field dosimetry, rather than the BCF-60 fiber. Its wavelength response is better matched for the MPPC and its smaller diameter is more conducive to high resolution dosimetry. The fiber dosimeter

can be applied in a wide range of orthovoltage irradiators to be used with the small fields typically seen in small animal irradiations. The water equivalent fiber and acrylic minimize dose perturbation, providing a more accurate representation of the orthovoltage beam. Based on the small scintillating element, this fiber dosimeter is ideal for preclinical small animal applications, which can perform accurate dosimetry in field sizes as small as $1 \times 1 \text{ mm}^2$. By scanning the element in very small finite steps across the beam, we can increase the spatial resolution. The PDD results have shown good linearity across the diameter of a mouse, with less than 1% difference from film response.

Current solutions for orthovoltage beam dosimetry, such as film and ion chambers, have proven to show disadvantages for preclinical applications. With the real time readout of the fiber dosimeter, real time dosimetry can be performed in the midst of a treatment to verify dose rate delivery and beam size. Film measurements cannot provide this real time readout and is therefore not useful for treatment adjustments. Ion chambers, with their larger spatial resolution, are very useful in IMRT treatments with standard field sizes of $10 \times 10 \text{ cm}^2$, but are less useful with field sizes smaller than the active volume. The fiber dosimeter presented here can be used to overcome these difficulties and improve spatial resolution.

E. References

- Attix, Frank Herbert. (1986) Introduction to radiological physics and radiation dosimetry. Strauss GmbH, Mörlenbach: Wiley-VCH.
- Beddar, A. S., Mackie, T. R., & Attix, F. H. (1992). Water-equivalent plastic scintillation detectors for high-energy beam dosimetry: I. Physical characteristics and theoretical considerations. *Phys. Med. Biol.* 37(10), 1883-1900.
- Beddar, A. S., Mackie, T. R., & Attix, F. H. (1992). Water-equivalent plastic scintillation detectors for high-energy beam dosimetry: II Properties and measurements. *Phys. Med. Biol.* 37(10), 1901-1913.
- CNMC. (2012). K602 Precision Electrometer, from <http://www.cnmcco.com/>
- Exradin Ion Chambers. (2012) Retrieved November 28, 2012
- Furetta, C., M. Prokic, R. Salamon, V. Prokic, & G. Kitis. (2001). Dosimetric characteristics of tissue equivalent thermoluminescent solid TL detectors based on lithium borate. *Nuclear Instruments and Methods in Physics Research.* 456, 411-417.
- Gafchromic. (2010). Gafchromic EBT2: Self developing film for radiotherapy dosimetry. Wayne, NJ: International Specialty Products.
- Herfarth, K. K. (2006). *New technologies in radiation oncology.* Berlin: Springer.

- Izaguirre, E. W., Price, S. G., Su, I.-T., Birch, J., & Low, D. (2012). Implementation of a micro resolution dual gantry preclinical image guided microirradiator. submitted to phys med bio.
- Khan, F. M. (2003). The physics of radiation therapy. Philadelphia, PA: Lippincott, Williams, & Wilkins.
- Mack, A., Scheib, S. G., Major, J., Gianolini, S., Pazmandi, G., Feist, H., . . . Kreiner, H.-J. (2002). Precision dosimetry for narrow photon beams used in radiosurgery - Determination of Gamma Knife output factors. *Med Phys*, 29(9), 2080-2089.
- Mabuchi, F., Aihara, M., Mackey, M. R., Lindsey, J. D., Weinreb, R. N. (2004) Regional optical nerve damage in experimental mouse glaucoma. *Invest Ophthalmol Vis Sci.*, 45, 4352-4358.
- Martisikova, M., Ackermann, B., & Jakel, O. (2008). Analysis of uncertainties in Gafchromic EBT film dosimetry of photon beams. *Phys. Med. Biol*, 53, 7013-7027.
- Mobit, P. N., P. Mayles & A. E. Nahum. (1995). The quality dependence of LiF TLD in megavoltage photon beams: Monte Carlo simulation and experiments. *Phys. Med. Biol.*, 41, 387-398.
- Rego, F., Abreu, M. d. C., & Peralta, L. (2011). A scintillating fiber dosimeter for radiology and brachytherapy with photodiode readout. submitted to *Med Phys*.
- Saint-Gobain. (2005). Scintillating optical fibers. Hiram, OH.
- Scanditronix, & Wellhoffer. (2012). CC04 Technical Data, from http://www.rpdinc.com/html/scandatronix_wellhoffer_compac.html
- Sheikh-Bagheri, D., & Rogers, D. W. O. (2002). Monte Carlo calculation of nine megavoltage photon beam spectra using the BEAM code. *Med Phys*, 29(3), 391-402.
- Withers, H. R. (1985). Biologic basis for altered fractionation schemes. *Cancer*, 55, 2086-2095.

Conclusions

The purpose of this work was to develop instrumentation and techniques for preclinical irradiations which will ultimately increase the prevalence and effectiveness of preclinical trials with improved clinical relevance. The first step in the process was the development and characterization of an orthovoltage treatment device. The device, in order to provide clinically relevant treatments, must provide orthovoltage treatments with appropriate beam filtering to effectively treat a small animal without undue harm. The treatment must be performed with submillimeter precision, to account for a small subject scale and target size with respect to a clinical human treatment. The characterization of this device was performed with clinical similarity in mind, using many of the same characterization methods and metrics. As such, this provided a one-to-one comparison with a clinical treatment, drawing more appropriate conclusions for treatments and results.

In order to aid in the submillimeter precision of the microIGRT, a portal imager was developed for image guided microirradiation therapy. This device was designed and developed according to clinical standards and put into use in every day orthovoltage treatments. This device has improved our preclinical treatments through positioning verification of the treatment subject and the treatment beam. The μ EPID was essential in the characterization of the microIGRT, hence its inclusion in every day treatments. The microIGRT and μ EPID were designed and developed together, for seamless operation, and providing the most effective image guided treatments. The microIGRT has now become part of a facility for Washington University in St. Louis, offering imaging and irradiation for cells and small animals. Collaborators from several different departments have utilized the microIGRT capabilities. Dr. Joshua Rubin, of Washington University in St. Louis, is carrying out research exploring combined drug and radiation therapy for pediatric gliomas. The microIGRT has been used to irradiate cells *in vitro*, which led to small animal irradiations. The treatment utilized image guided irradiations every day for a total of 10 or 20 days, delivering 2 Gy per fraction. One small animal from each cohort is imaged with the microCT and a 256 image reconstruction is contoured in the treatment planning system and a back projection of the target brain tumor is produced. Using our

tungsten-epoxy method, a treatment beam mask is developed and used for each of the mice in a cohort. Before every fraction, each small animal is anesthetized and a quick planar microCT image is acquired for daily positioning. After the subject has been transferred to the microRT field of view, a portal image is acquired to verify subject and mask positioning. Daily positioning alterations for each small animal allows us to use a single mask for each beam position while still providing personalized treatment for each small animal. This system takes interfraction motion and set-up errors into account so a targeted treatment can still be delivered. This small animal trial was important for the development of the radiotherapy drug because it gave the researchers an idea of the combined effects of the drug and irradiation. The drug uptake and the efficacy of irradiation could be tested *in vitro* but only an *in vivo* trial would demonstrate the effectiveness of the combined therapies, as well as possible side effects. A clinical trial will be performed based on the results of the preclinical trial. Based on years of experience with preclinical drug trials, it is well understood how the drug dose in a small animal should be correlated to a human dose and how the side effects in a mouse can help draw conclusions for human side effects. What is less well understood, however, is how to translate the results of the irradiation from a small animal to a human.

Because an orthovoltage small animal treatment is inherently different from a clinical human treatment, we have developed a set of metrics to be defined for clinical and preclinical treatments at several treatment sites. The metrics and treatment sites developed in this work should be used as the foundation for additional work in the future. There are a large number of mice breeds that could be considered if their sizes vary significantly. This work could also be extended to include rats when used for irradiation trials. The treatment sites chosen in this work were considered to be the primary locations of interest for preclinical studies; however, there are additional sites, such as GYN, which could be considered in further studies. As the extent of this work grows, hopefully so will the use of preclinical trials. It is standard practice for novel drug developments to be tested on small animals based on the extensive knowledge of drug interactions in both small animals and humans. The paradigm of radiation therapy should follow this example and put preclinical trials into effect for new irradiation developments. This work is the first step in realizing this goal. The necessity of these metrics and guidelines presented in this work is demonstrated in the ever changing field of clinical treatments. Every day there are new protocols and instrumentation developed for radiation therapy and imaging, and it is crucial that the preclinical environment stay as up to date with the

clinic as much as possible. This means that preclinical instrumentation should deliver treatments with the same level of accuracy and effectiveness, as demonstrated in the characterization of the microIGRT. Advanced clinical treatments, such as stereotactic radiosurgery, utilize small field sizes with hypofractionated treatments. This treatment option is not yet used on a wide spread basis in preclinical trials due to the very high precision of imaging and treatment required with very small field sizes. Therefore, in order to use a preclinical trial for developments in this field, preclinical instrumentation must adapt to this new paradigm of treatment. The metrics developed in this work can guide a researcher in the design and development of improved instrumentation based on the requirements laid out by clinical metrics. The characterization of this new instrumentation will also need to adapt to smaller field sizes, as demonstrated in this work with scintillating fiber microdosimetry.

Small field dosimetry in microirradiations is necessary because current dosimeters utilized in the clinic are not necessarily ideal for preclinical orthovoltage irradiations. A scintillating fiber dosimeter was an excellent option for our small field dosimetry based on the wide energy range of scintillating fibers, the small dosimeter size, as well as the linear dose response. In this work, we compared two scintillating fibers coupled with an MPPC for low photon emission counting. The electronics developed are simple to produce and maintain, and the fibers are low cost, which are conducive for preclinical applications especially when budgets are a factor. Of the two fibers chosen for testing, BCF-12 and BCF-60, the BCF-12 fiber was ideal, based on the smaller diameter and better matched wavelength output with the photodiode. We have demonstrated that we can perform high resolution dosimetry, with responses superior to ion chamber results and closely matched with film results. Ion chambers are most commonly used for dosimetric purposes, thus providing a clinical comparison, and GafChromic film is the highest resolution available, the gold standard for comparison. The results of this work are highly useful for preclinical orthovoltage irradiations, because they will improve small animal treatment planning with more accurate dose distribution characterization, similar to the precision seen in the clinic.

With the completion and publication of this work, researchers in preclinical radiation oncology will now have improved tools for developing image guided microirradiators and small animal treatment plans with maximized clinical relevance. The ultimate goal of a novel radiation oncology development is to improve the quality of life of patients in the clinic. My work, although not directly applicable to the clinic, is

essential is helping others accomplish this goal. Through the use of clinically comparable irradiation devices and treatment plans, radiation oncology developments will undergo preclinical small animal testing and produce results that can be directly translated to clinical applications, which will expedite the developments' progress to the clinic and improve patient treatment.

VITA

Samantha Price grew up in Fulton, MO with her parents and two brothers. Her mother is a crafter and her father is a mechanical engineer at the Ameren nuclear power plant in Fulton. She attended Fulton Public Schools through her high school graduation in 2004. She received her Bachelor's in Nuclear Engineering from Missouri University of Science and Technology, formerly University of Missouri-Rolla, in 2008. Following an internship with Ameren in the summer of 2007, Samantha decided nuclear power was not her first choice of careers and began to explore the use of nuclear science in medicine. This led her to medical physics. In December of 2009, she received her Master's in Nuclear Engineering with an emphasis in Medical Physics from the University of Missouri. Her Master's thesis was entitled "*In vitro* and *in vivo* MRI evaluation of an MRI contrast agent targeting prostate cancer" and her adviser was Dr. Lixin Ma. During her doctoral work, Samantha passed the first part of the American Board of Radiology's Medical Physics certification exam. Following her graduation, Samantha will begin a two year physics residency with Washington University in St. Louis to pursue a career in medical physics.